



Eidgenössische Technische Hochschule Zürich  
Swiss Federal Institute of Technology Zurich



Massachusetts  
Institute of  
Technology

## MASTER THESIS

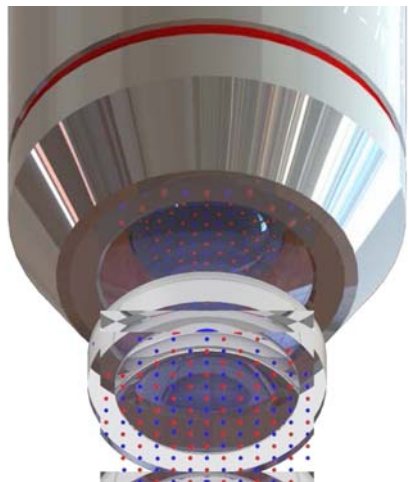
---

# A Quantum Gas Microscope for Fermionic Atoms

---

CHRISTIAN THOMAS JOACHIM GERSDORF

MIT-Harvard Center for Ultracold Atoms



*Advisors:*

Prof. Dr. Martin Zwierlein  
Assistant Professor of Physics  
Department of Physics  
Massachusetts Institute of Technology  
Cambridge, Massachusetts, USA

Prof. Dr. Tilman Esslinger  
Institute for Quantum Electronics  
Department of Physics  
ETH Zürich  
Zurich, Switzerland



## Abstract

This work reports on the concept and on the design as well as the subsequent construction of a fermionic quantum gas microscope for the two fermionic species  $^6\text{Li}$  and  $^{40}\text{K}$  with a bosonic sympathetic coolant  $^{23}\text{Na}$ . It is shown how in-situ imaging of fermionic atoms in a two-dimensional optical lattice could be realized similar to the bosonic quantum gas microscopes that have been built so far as reported in [1] and [2].

A novel setup for the high-resolution imaging system has been embedded into a custom design for a triple species experiment that allows to trap and cool dilute vapors of  $^6\text{Li}$  and  $^{40}\text{K}$  together with the bosonic coolant  $^{23}\text{Na}$  down to the quantum degenerate regime at ultracold temperatures and ultralow pressures.

According to the developed design, the components for the experiment have been built and set up. An ultra-high-vacuum system has been brought to operation and the mechanical setup of the experiment has been completed. The optical setup for laser cooling of  $^{40}\text{K}$  and  $^6\text{Li}$  has been constructed and  $^{40}\text{K}$  atoms have been trapped in the three-dimensional magneto-optical trap.

In addition, a magnetic trap has been constructed and attached to the experiment, which is suitable for both trapping atoms and creating large homogeneous magnetic fields for Feshbach resonances. The successful operation of the magnetic trap has been shown with  $^{40}\text{K}$  atoms. First components of a high-resolution imaging systems capable of resolving single atoms in an optical lattice have been assembled and prepared for deployment in the experiment.

Simultaneously with the construction of the individual components of the new experiment, the whole infrastructure necessary for an ultracold atom experiment has been established. As a result, the experiment apparatus is now ready to cool and trap ultracold samples of  $^{40}\text{K}$  and the sympathetic coolant  $^{23}\text{Na}$  with the option of adding  $^6\text{Li}$  samples later.

Date of submission: 30<sup>th</sup> September, 2012

Version: 12<sup>th</sup> March, 2013

In this version illustrations and graphics were rendered at 150 dpi.

---

# Contents

---

<b>Contents</b>	<b>ii</b>
<b>1 Introduction</b>	<b>1</b>
1.1 Outline . . . . .	5
<b>2 Quantum-degenerate fermions in optical lattices</b>	<b>7</b>
2.1 Ultracold quantum gases . . . . .	7
2.1.1 The ideal Fermi gas in a harmonic trap . . . . .	9
Semi-classical Thomas-Fermi approximation . . . . .	10
Continuum approximation and density-of-states . . . . .	11
2.1.2 Interactions of fermions . . . . .	12
Fundamental scattering properties in ultracold atoms . . . . .	12
Control of interactions with Feshbach resonances . . . . .	14
2.2 Optical lattice potentials . . . . .	15
2.2.1 Conservative and dissipative light forces . . . . .	16
2.2.2 The oscillator model . . . . .	16
2.2.3 Dipole potential and scattering rate . . . . .	18
2.2.4 Blue and red detuning of dipole traps . . . . .	18
2.2.5 Dressed atom picture . . . . .	19
2.3 Optical dipole traps . . . . .	19
2.4 Creation of optical lattices . . . . .	20
2.4.1 Rectangular geometries . . . . .	20
2.5 Band structure . . . . .	21
<b>3 Emulating condensed matter system with ultracold fermions</b>	<b>23</b>
3.1 The Fermi-Hubbard model . . . . .	23
3.1.1 Mott insulator of fermionic atoms . . . . .	25
3.1.2 Insulating phases . . . . .	26
3.2 Antiferromagnetically ordered phase . . . . .	27
3.3 The quest for high-temperature superconductivity . . . . .	29
3.4 Second generation quantum gas microscopy . . . . .	30
3.5 Synthetic gauge fields and topological phases . . . . .	31
<b>4 The Fermi gas experiment</b>	<b>33</b>
4.1 Atomic species . . . . .	33
4.2 Experimental concept and cooling strategy . . . . .	34
4.3 Mechanical layout . . . . .	37
4.3.1 Imaging system setup . . . . .	37
4.4 Vacuum system . . . . .	38
4.4.1 Main trapping chamber . . . . .	40
4.4.2 Re-entrant viewports for DN200CF flanges . . . . .	40
Re-entrant viewports for DN63CF flanges . . . . .	42
4.4.3 Optical viewports . . . . .	43

4.4.4	$^{40}\text{K}$ source . . . . .	43
4.4.5	Double species $^6\text{Li}$ and $^{23}\text{Na}$ source . . . . .	44
4.4.6	Differential pumping . . . . .	45
4.4.7	Mounting system and double-layer optical table . . . . .	46
4.4.8	Construction and baking . . . . .	47
4.5	Experiment control . . . . .	48
<b>5</b>	<b>Laser cooling</b>	<b>49</b>
5.1	2D-MOT for $^{40}\text{K}$ . . . . .	49
5.2	Zeeman slower for $^6\text{Li}$ and $^{23}\text{Na}$ . . . . .	52
5.3	Laser systems . . . . .	54
5.3.1	Laser system for $^{40}\text{K}$ . . . . .	54
5.3.2	Laser system for $^6\text{Li}$ . . . . .	55
5.3.3	Laser system for $^{23}\text{Na}$ . . . . .	56
5.4	Triples-species 3D-MOT . . . . .	56
5.5	Sub-Doppler cooling of $^{40}\text{K}$ . . . . .	58
5.6	Optical pumping . . . . .	59
<b>6</b>	<b>Cooling to quantum degeneracy</b>	<b>61</b>
6.1	Magnetic trapping . . . . .	62
6.1.1	Design of the magnetic trap . . . . .	63
6.1.2	Fabrication of magnetic coils . . . . .	66
6.1.3	Water cooling . . . . .	67
6.1.4	Electrical connections . . . . .	69
6.1.5	Test of magnetic coils . . . . .	71
6.1.6	Gravitational sag . . . . .	72
6.2	Magnetic transport . . . . .	74
6.2.1	Current ramps . . . . .	74
6.3	Evaporative cooling . . . . .	77
6.3.1	RF antenna . . . . .	77
6.3.2	Evaporation of a two-component fermi gas . . . . .	78
6.3.3	Sympathetic cooling . . . . .	79
<b>7</b>	<b>An imaging system for fermions with single-atom and single site-resolution</b>	<b>81</b>
7.1	A high numerical aperture imaging system . . . . .	81
7.2	Testing the imaging system . . . . .	84
7.2.1	Microscope objective tests . . . . .	84
7.2.2	Interferometric test setup . . . . .	85
7.2.3	Imaging nanospheres . . . . .	86
7.3	Loading the atoms in the optical lattice . . . . .	88
7.4	Parity imaging . . . . .	89
<b>8</b>	<b>Outlook</b>	<b>91</b>
<b>A</b>	<b>Technical Data</b>	<b>95</b>
A.1	IBS coating of the main chamber viewports and hemisphere . . . . .	95
A.2	IBS coating of the super-polished substrate . . . . .	96
A.3	Interferometric measurement of DN200CF re-entrant viewport windows after the MRF-polishing process . . . . .	97
A.4	Hemispheric lens for the imaging system . . . . .	99

<b>B CAD drawings of the main chamber</b>	<b>101</b>
<b>C CAD drawings of other components</b>	<b>113</b>
C.1 DN200CF re-entrant viewports . . . . .	113
C.2 DN63CF re-entrant viewports . . . . .	115
C.3 Optical breadboards . . . . .	117
<b>D Pictures of the experiment construction</b>	<b>121</b>
<b>E Technical reference information</b>	<b>125</b>
E.1 IGBT box . . . . .	125
E.2 MOSFET box . . . . .	126
<b>List of Figures</b>	<b>127</b>
<b>List of Tables</b>	<b>132</b>
<b>Bibliography</b>	<b>133</b>

---

## 1. Introduction

---

The physics of condensed matter is often governed by the collective quantum behavior of many particles due to their strong interactions. A lot of the many-body physics of different condensed matter systems could be accessed with conventional solid state physics, but some phenomena are still not understood.

A very prominent example is high-temperature superconductivity, which is mainly observed in the cuprates, chemical complexes containing copper anions. Since its discovery in 1986 [3], high-temperature superconductivity has defeated all attempts to explain its physical origin. Other examples include colossal magnetoresistance<sup>1</sup> [4], heavy-fermion systems<sup>2</sup> [4] and lower-dimensional systems [5] like the 2-dimensional setting of the fractional quantum hall effect [6]. Similarly, only very little is known about the physics of so-called topological electronic phases. While many of these phases have been predicted, only the topological insulators have been discovered in condensed matter systems so far [7].

Common to all these phenomena is their origin in the interplay of many-particles interacting as dictated by quantum mechanics. It seems to be very hard to develop models for these phenomena that accurately describe the physics without becoming too complicated to be solved theoretically or computationally. Richard P. Feynman noticed already in 1982 that one would need a quantum simulator to solve some of these challenging problems of condensed matter physics [8] because a classical simulator cannot efficiently simulate the full behavior of a quantum system.

A promising approach to quantum simulation of condensed matter systems is the uses of quantum gases. The field of quantum gases approaches many-body physics in a wholly different way from conventional condensed-matter physics. Instead of observing phenomena that trigger theoretical explanations, people try to develop experimental systems that mimic the behavior of many-body systems. Many phenomena have been discovered this way, for instance the early milestone of a Bose-Einstein condensate (BEC) in 1995, [9] and [10], the crossover from a molecular BEC to the BCS regime in a strongly interacting Fermi gas ([11], [12] and [13]) and the superfluid to Mott-insulator transition of a Bose gases loaded into an optical lattice [14].

Moreover, trapped ultracold atoms are some of the purest many-particle systems that have been ever created, because laser cooling is highly selective and several billion atoms of exactly one isotope of one atomic species are trapped. Impurities can be added later in a controlled way by adding other atomic species or even other spin states, which provides another versatile set of experimental tuning parameters.

---

<sup>1</sup>The colossal magnetoresistance is an effect occurring in some materials, by which a magnetic field can cause a dramatic change in electrical resistance. This effect might have interesting applications, for instance for probing magnetically stored information in, e.g., computer hard drives.

<sup>2</sup>Heavy-fermion systems refer to a special class of materials which have a very high density of electronic states (several orders of magnitude higher than in metals) and are especially interesting because they are in the regime where magnetic and electronic quantum fluctuations are strongly coupled.

Another advantage of ultracold atom experiments is that one can observe the dynamics of condensed matter phenomena in slow-motion, so to speak: the intrinsic timescales of the internal electronic dynamics of solids are on the order of femto- to attoseconds, requiring extremely quick measurements, for instance by ultrafast lasers, to resolve (see [15] or [16]). In an ultracold atom experiment, by contrast, the small energy scales and the low temperatures stretch the timescales significantly, such that physical phenomena can occur on the microsecond to millisecond timescale.

Shortly after the observation of a BEC, weakly interacting systems of bosons were in the focus of the field and experiments explored coherence properties [17], excitations predicted by the Bogoliubov mean field theory of the weakly interacting Bose gas ([18] and [19]) and the superfluid behavior by creating vortices in a BEC ([20], [21] and [22]), to name some important examples.

It is the nature of this rapidly developing field that with the experimental realization of a quantum degenerate gas of fermionic atoms in 1999 [23] and the access to Feshbach resonances [24], opening the possibility to tune the interaction of atoms by changing the magnetic field, the focus of research quickly moved to strongly correlated systems of bosons and fermions.

The concept of so-called optical lattices provided an even better connection to condensed matter systems, first proposed in 1998 [25]: The Bose-Hubbard Hamiltonian, a model from condensed matter theory [26], should be simulated by loading bosonic atoms into a potential created by a standing wave laser light beam. Unlike the lattice potential created by the Coulomb potential of ions in a crystal, the optical lattice potential depth can be tuned by changing the light intensity of the laser beam. With this tool, researchers were able to experimentally observe the quantum phase transition from the superfluid to the Mott-insulating phase [14].

After successfully exploring the bosonic Hubbard model, the researcher community then saw the realization of the corresponding model for fermions [27] and Bose-Fermi mixtures ([28] and [29]). The observation of a Mott insulator of fermionic atoms in an optical lattice, [30] and [31], was another landmark result that manifested the connection to condensed matter physics.

In the last few years, another technological development has given a fundamentally different view on the physical phenomena: While so far almost all experiments relied on the indirect observation of physical properties, so-called quantum gas microscopes made it possible to image single bosonic atoms on single lattice site of optical lattices. Although this idea was already implemented in a couple of special condensed matter systems (for instance by using scanning tunneling microscopes, [33] and [34]), it was only a few years ago that high-resolution imaging techniques were applied to ultracold quantum gases [35].

A very nice demonstration of the power of this technique [36] is the single-site resolved observation of the superfluid-to-Mott insulator transition in a two-dimensional optical lattice, [1] and [32], which can be seen in figure 1.1: Whereas in a shallow optical lattice with no interactions the atoms are in a superfluid state with tremendous number fluctuations, they form a Mott insulation state with constant number of atoms per site (second column in the figure) when the lattice and repulsive interactions are turned on.

Due to the external harmonic confining potential provided by the Gaussian shape of the lattice laser beam, the atom number per lattice site varies spatially: In the second column each lattice

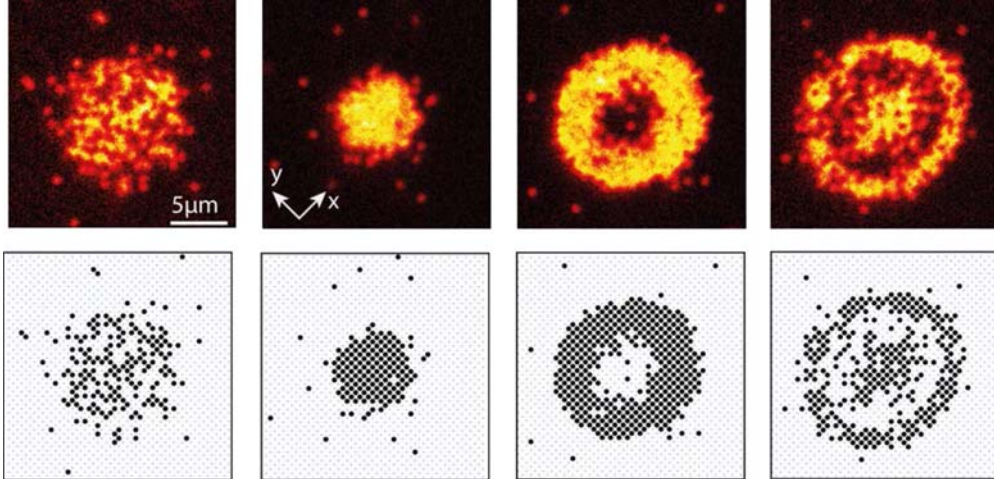


Figure 1.1: High-resolution fluorescence images and reconstructed single-site resolved occupation numbers of a superfluid BEC (left column) and Mott insulators with three different fillings (right three columns) in a two-dimensional optical lattice as observed with a bosonic quantum gas microscope. The experiment is described in [32], from which the figure was adapted.

site in the center of the external potential is filled with exactly one atom because of the repulsive interactions; a Mott insulator has formed and the superfluid behavior has vanished. When adding more atoms, in the a small region in the center of the external confinement the lattice sites are populated with two atoms (third column) and three atoms (fourth column) at even higher atom numbers<sup>3</sup>.

These images show how these many-body phenomena can probed locally and how the physical conditions can be tuned by changing external parameters like the magnetic field and the lattice depth via the light intensity. As it will become clear in chapter 3, with ultracold atomic gases one can, so to speak, engineer a Hamiltonian of many-body system.

Now this concept should be extended to fermionic atoms. This is especially appealing since electrons are fermions and strongly-correlated electron systems play a key role in condensed-matter physics. In the past, people have developed techniques to probe and manipulate fermions with single-atom level resolution [37], but they can look only at up to ten fermionic atoms in an optical micro trap, which basically corresponds to one lattice site. Therefore these few-fermion systems cannot model the lattice physics with many different lattice sites, where tunneling between neighboring lattice sites plays an important role. Our system should be able to look at the interactions of up to few hundreds of fermions distributed over many lattice sites and hence be able to reveal new effects of quantum many-body physics.

This work describes a new experiment implementing a quantum gas microscope for fermionic atoms, a *fermi gas microscope*. A conceptual illustration is given in figure 1.2. Like other

---

<sup>3</sup>As the figure shows, a quantum gas microscope can only detect the parity of atom number on a lattice since light-assisted collisions lead to the loss of atom pairs. See also section 7.4.



Figure 1.2: Concept of quantum gas microscope: Atoms of different spin states are trapped in an optical lattice and placed in front of a high-resolution imaging system.

experiments with ultracold fermions, various techniques are applied to cool and trap fermionic atoms at very low densities in an optical lattice created inside a vacuum chamber by laser light beams. As in the bosonic quantum gas microscope, this sample of fermionic atoms is now imaged with a high-resolution imaging system consisting of a special lens which is optically contacted (optical contact bonding<sup>4</sup>) to the vacuum window, a microscope objective and a CCD camera (not shown in the figure).

With this quantum gas microscope for fermions we hope to ultimately gain access to different phases of the Fermi-Hubbard model, most importantly the antiferromagnetically ordered state and the d-wave superconducting state ([38],[39]).

The antiferromagnetically ordered Mott insulator is one of next goal for experimentalists; so far no experiments have reached below the Néel temperature, above which the thermal energy is sufficient to destroy to antiferromagnetic ordering. In contrast to a bulk measurement a quantum gas microscope should be able to resolve the first antiferromagnetically ordered domains even slightly above the Néel temperature.

In this work a concept for quantum gas microscope for fermionic atoms has been developed and an experiment has been designed and implemented.

---

<sup>4</sup>Optical contact bonding is a method to join two optical elements with conformal surfaces without any glue. The two pieces are just held together by the intermolecular forces like the van-der-Waals force.

## 1.1 Outline

In the next chapter some fundamental concepts important to understand the phenomena of ultracold fermions in optical lattices are explained. Subsequently, chapter 3 covers some of the physical phenomena that can be accessed with a quantum gas microscope for fermions and which essentially provide the motivation for this experiment.

An overview of the setup of the new fermi gas microscope is given in chapter 4. Chapter 5, 6 and 7 focus on three important parts of our experimental setup, namely the laser cooling, the cooling down to quantum degeneracy, and the imaging with our newly developed high resolution imaging system.

As this work describes an experiment which is still being constructed at time of writing, chapter 8 summarizes the current state of the experiment at the time of writing and describes the future perspective.

The concept and design of the new experiment was developed by the author under supervision of Waseem S. Bakr and Martin W. Zwierlein. The construction of the new experiment was carried out in collaboration with Vinay V. Ramasesh [40] and Waseem S. Bakr with help from Sara L. Campbell, David Reens, Jordan Goldstein, Melih Okan and Takuma Inoue.



---

## 2. Quantum-degenerate fermions in optical lattices

---

In this experiment the central idea is to load a quantum-degenerate gas of strongly interacting fermionic atoms into an optical lattice and study its behavior by imaging it with a high-resolution imaging system capable to resolve single atoms. The physics that this experiment tries to explore is governed by the fundamental quantum mechanic properties of fermionic atoms, interactions of atoms and by the concept of optical lattices.

This chapter summarizes important key concepts, but does not provide a full theoretical treatment which would be beyond the scope of this thesis. For good reviews on ultracold Fermi gases see for instance [41] and [42]. Along with recent dissertations in that field (e.g. [43]) and the other references cited in this chapter these review articles provide the theoretical framework for the current ultracold quantum gas experiments.

Although in the experiment described by this work bosonic and fermionic species will be used, ultracold fermionic atoms are in the focal point of interested. Bosonic atoms will be employed in sympathetic cooling techniques, but will not be covered in this chapter. The reader is referred to the available literature (see for instance [44] for Bose-Einstein condensation and [45] for many-body physics with bosonic and fermionic atoms).

### 2.1 Ultracold quantum gases

Identical atoms in a classically behaving gas populate the energy levels according to the Boltzmann distribution [46]. However, the quantum nature of the atoms plays a major role in our experiments with ultracold quantum degenerate gases and the quantum mechanic spin is governing the behavior. A main reason is that in the quantum degenerate regime the energy scales are very small and the populations of the energy levels of the considered systems can be much greater than unity.

For systems of many particles their quantum statistics and spin are closely related. While the squared absolute value of the many-body wave function is invariant with respect to the interchange of two particles due to the fundamental indistinguishability of quantum particles,

$$|\Psi(\dots, \vec{x}_i, \vec{x}_j \dots)|^2 = |\Psi(\dots, \vec{x}_j, \vec{x}_i \dots)|^2, \quad (2.1)$$

the wave function transforms symmetrically or anti-symmetrically:

$$\Psi(\dots, \vec{x}_i, \vec{x}_j \dots) = +\Psi(\dots, \vec{x}_j, \vec{x}_i \dots) \quad (2.2)$$

or

$$\Psi(\dots, \vec{x}_i, \vec{x}_j \dots) = -\Psi(\dots, \vec{x}_j, \vec{x}_i \dots). \quad (2.3)$$

The Pauli principle coined by Wolfgang Pauli [47] states that the wave function of bosonic particles with integer spin transforms according to equation 2.2 and the wave function of fermionic particles with half-integer spin according to equation 2.3.

As a consequence, a quantum state can be occupied by at most one fermionic particle, because otherwise  $\Psi(\dots, \vec{x}_i, \vec{x}_i \dots) = -\Psi(\dots, \vec{x}_i, \vec{x}_i \dots) \stackrel{!}{=} 0$ . This gives rise to the fact that the fermions obey the Fermi-Dirac statistics, whereas bosons obey Bose-Einstein statistics. In quantum field theory this is known under the name of **spin-statistics theorem** [48].

Figure 2.1 provides an illustration of the consequences of the Pauli principle: Whereas many equal bosons (depicted as blue spheres) can be in the ground state of a quantum harmonic oscillator potential (macroscopic population up to a Bose-Einstein condensate is possible), only one fermion of the same quantum state (red sphere) can occupy a single quantum state.

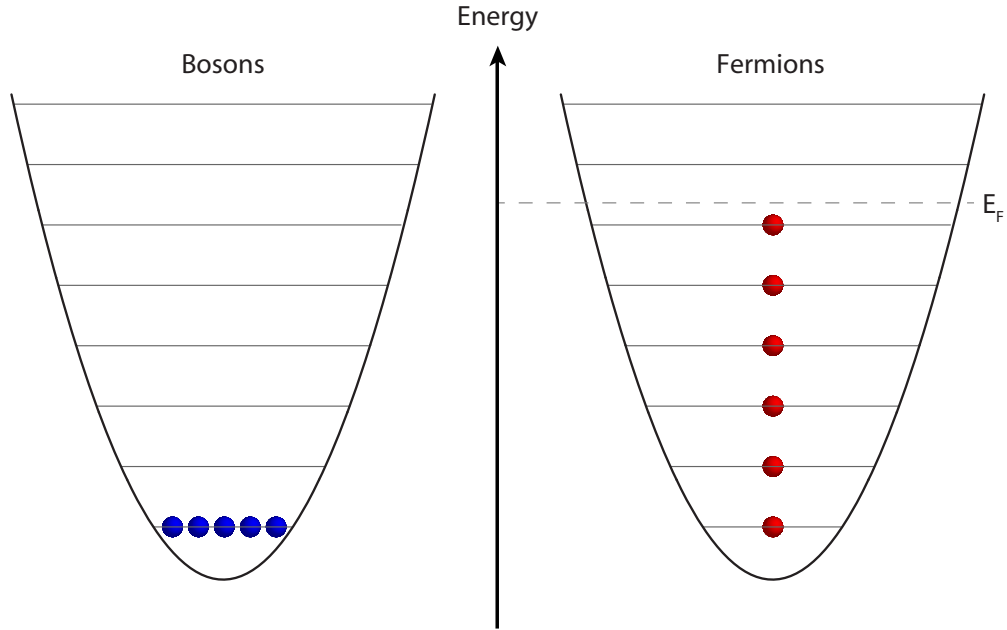


Figure 2.1: Illustration of the Pauli principle with bosonic/fermionic atoms in harmonic potential at  $T \rightarrow 0$ : Whereas for bosons multiple occupation of one quantum state is possible, there is at most one fermionic atom in a single quantum state.

Many interesting quantum mechanical phenomena such as Bose-Einstein condensation occur in the quantum degenerate regime, which is often described as the regimes where the wave functions of different particles *overlap*. For bosons, the phase transition to Bose-Einstein condensation occurs when the de-Broglie wavelengths of the atoms are on the order of the average particle spacing,  $n_B^{\text{cond}} \lambda_{\text{dB}}^3 \approx 1$ . In a Bose-Einstein condensate, all atoms can be described by a single wave function that is macroscopically occupied.

For a homogeneous gas in free space this condition for quantum degeneracy is

$$n_B^{\text{cond}} \lesssim \frac{2.612}{\lambda_{\text{dB}}^3} = 2.612 \left( \frac{2\pi\hbar^2}{mk_{\text{B}}T} \right)^{\frac{3}{2}} \quad (2.4)$$

Dilute ultracold gas samples are ideal to reach this regime because they circumvent the problem that at low temperatures almost every element solidifies. On the other hand the needed temperatures are extremely low and in fact the lowest temperatures humans have been able to create. In quantum gas experiments typical densities are  $n_{\text{typ}} = 10^{12} \frac{1}{\text{cm}^3}$  at temperatures of  $T_{\text{typ}} = 10^{-8} \text{ K}$ .

In ultracold Fermi gases the phase transitions to a Bose-Einstein cannot be observed in atomic samples<sup>1</sup>. This is exactly due to the Pauli principle that prohibits the occurrence of more than one identical fermions in the same quantum state.

Instead, in Fermi gases the quantum states of the system are occupied with not more than one particle up to the Fermi energy  $E_F$ , while excitations can leave intermediate states unoccupied. Figure 2.2 shows how according to Fermi-Dirac distribution the occupation changes function of the temperature. The characteristic temperature associated with the Fermi energy  $E_F$  is the Fermi temperature  $T_F$ . One can see how the Fermi-Dirac distribution changes its shape from an almost classical Boltzmann distribution at temperatures high compared to the Fermi temperature to a quantum distribution at low temperatures reflecting the Pauli principle. In the limit  $T \rightarrow 0$  the Fermi-Dirac distribution approaches a Heaviside step function  $\theta(E_F - E)$ .

It is this quantum degenerate regime of a Fermi gas that this experiment tries to explore microscopically. Quite remarkably electrons in a solid resemble such a quantum degenerate system even far above room temperature due to the light mass of the electron and high electron density.

### 2.1.1 The ideal Fermi gas in a harmonic trap

Magnetic fields and optical dipole traps provide a confinement that traps the atoms in a very small region in center of a vacuum chamber. For working out the thermodynamics of an ideal Fermi gas, the trapping potentials can be considered harmonic in the three spatial dimensions to a good approximation since the ultracold atoms will sit close to the center of the trap. The potential energy of an ideal harmonic trapping potential in three dimensions is given by

$$V(x, y, z) = \frac{1}{2}m(\omega_x^2x^2 + \omega_y^2y^2 + \omega_z^2z^2) \quad (2.5)$$

with the trapping frequencies  $\omega_{x,y,z}$  that characterize the steepness of the trap in the three directions  $x, y, z$ .

The quantum mechanic eigenstates for one particle in this harmonic trap are products of Hermite polynomials [49] with the eigenvalues

$$E_{n_x, n_y, n_z} = \hbar\omega_x \left( \frac{1}{2} + n_x \right) + \hbar\omega_y \left( \frac{1}{2} + n_y \right) + \hbar\omega_z \left( \frac{1}{2} + n_z \right). \quad (2.6)$$

---

<sup>1</sup>However, if two fermions are tightly bound in a molecule, Bose-Einstein condensation can occur [41]. In this case the two fermions act as a composite boson and the quantum statistics can be now described by Bose-Einstein statistics.

To simplify calculations, a geometric mean trapping frequency

$$\bar{\omega} = (\omega_x \omega_y \omega_z)^{\frac{1}{3}} \quad (2.7)$$

is usually introduced that characterizes the mean steepness of the trap.

Now, fermionic atoms are loaded into this trapping potential. The atoms are considered in the limit of no interactions in the grand canonical ensemble [50], which means that the system of atoms is isolated from the environment but in contact with a reservoir enabling the exchange of energy and particles.

In typical ultracold atom experiments one obtains absorption or fluorescence images of the cold atomic cloud with a CCD camera. The obtained image is the density distribution of the atoms integrated along the direction of imaging.

### Semi-classical Thomas-Fermi approximation

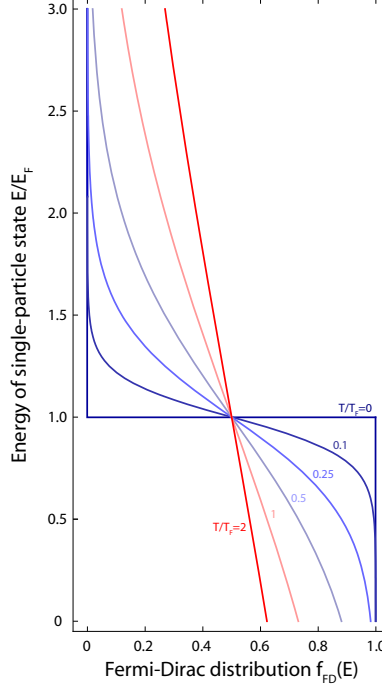


Figure 2.2: Fermi-Dirac distribution as a function of energy (vertical axis) for different temperatures expressed relative to the Fermi temperature  $T_F$ . Below  $T = T_F$  the Fermi-Dirac changes its shape and reaches a step function  $\theta(E_F - E)$  at  $E = E_F = \mu_0$  at zero temperature.

Theoretically, the density distribution and the total number of atoms of an ideal Fermi gas trapped in potential  $V(\mathbf{r})$  can be calculated analytically in a semi-classical approximation often called the **Thomas-Fermi approximation**: While the *quantum* statistical distribution function

for fermionic atoms, the Fermi-Dirac distribution

$$f_{\text{FD}}(E_i, T) = \frac{1}{\exp\left[\frac{E_i - \mu}{k_B T}\right] + 1}, \quad (2.8)$$

is used, a *classical* Hamiltonian  $H(\mathbf{r}, \mathbf{p})$  approximates the energy expression in the denominator:

$$f_{\text{FD}}(\mathbf{r}, \mathbf{p}, T) = \frac{1}{\exp\left[\frac{\frac{p^2}{2m} + V(\mathbf{r}) - \mu}{k_B T}\right] + 1}, \quad (2.9)$$

This semi-classical approximation corresponds to a local density approximation and is applicable in the limit of large particle numbers where the relevant energies are much larger than the harmonic oscillator splitting, i.e.  $\mu_0 \gg \hbar\omega_{x,y,z}$  ([42] and [43]).

By integrating the Fermi-Dirac distribution  $f(E, T)$  over the momentum coordinates the spatial density distribution can be obtained:

$$n_{\text{FD}}(\mathbf{r}) = \int \frac{d^3 p}{(2\pi\hbar)^3} f_{\text{FD}}(\mathbf{r}, \mathbf{p}, T) = -\frac{1}{\lambda_{\text{dB}}^3} \text{Li}_{\frac{3}{2}}\left(-e^{\frac{\mu - V(\mathbf{r})}{k_B T}}\right), \quad (2.10)$$

where  $\text{Li}_s(z) = \sum_{k=1}^{\infty} \frac{z^k}{k^s}$  is the polylogarithm function.

Integrating the density distribution over the spatial coordinates yields the total number of atoms as a function of temperature and chemical potential:

$$N_{\text{tot}} = \int d^3 r n_{\text{FD}}(\mathbf{r}) = \int d^3 r \frac{d^3 p}{(2\pi\hbar)^3} f_{\text{FD}}(\mathbf{r}, \mathbf{p}, T) = -\left(\frac{k_B T}{\hbar\bar{\omega}}\right)^3 \text{Li}_3\left(-e^{\frac{\mu}{k_B T}}\right). \quad (2.11)$$

This relation fixes the chemical potential as function of the total atom number and the temperature.

### Continuum approximation and density-of-states

When the discrete spectrum of the confinement (in our case the harmonic trap) is not resolved<sup>2</sup>, a continuum approximation [43] with the density-of-states can be used.

For a harmonic trap the density of states is given by

$$g(E) = \frac{E^2}{2\hbar^3\bar{\omega}^3}. \quad (2.12)$$

The expression of the total number of atoms can be now expressed as the product of the density of states and the general Fermi-Dirac distribution over all possible energies:

$$N_{\text{tot}} = \int_{E=0}^{\infty} \frac{g(E)}{\exp\left[\frac{E - \mu}{k_B T}\right] + 1} dE = -\left(\frac{k_B T}{\hbar\bar{\omega}}\right)^3 \text{Li}_3\left(-e^{\frac{\mu}{k_B T}}\right) \quad (2.13)$$

---

<sup>2</sup>For the harmonic oscillator this condition corresponds to  $k_B T \gg \hbar\omega_{x,y,z}$ .

In the limit of zero temperature the Fermi-Dirac distribution approaches the step function  $\theta(\mu - E)$  meaning that all states are filled up to the Fermi energy:

$$\lim_{k_B T \rightarrow 0} N = \int_{E=0}^{\infty} g(E) \theta(\mu - E) dE = N. \quad (2.14)$$

One can see from this expression that the Fermi energy is identical to the chemical potential at zero temperature.

Keeping in mind that the density of states for a harmonic oscillator potential given by equation 2.12 one can deduce the Fermi energy as a function of the number of atoms in the harmonic oscillator potential

$$E_F = \mu_{T=0} = \hbar\bar{\omega} (6N)^{\frac{1}{3}} \quad (2.15)$$

and the associated Fermi temperature

$$T_F = \frac{E_F}{k_B}. \quad (2.16)$$

### 2.1.2 Interactions of fermions

In the previous section an ideal, non-interacting gas of fermions was considered. Interactions between atoms give rise to many physical phenomena and are crucial for a complete description of a system of ultracold fermions. Atom-atom interactions are not only necessary for thermalization and several cooling techniques<sup>3</sup> but can be also controlled precisely by Feshbach resonances.

#### Fundamental scattering properties in ultracold atoms

At ultracold temperatures the scattering energies are small and the scattering of atoms can be described by quantum mechanical scattering theory. Typically, the densities of the ultracold atomic samples are very low and the mean interatomic distances very large, therefore the dominant scattering events are two-body interactions [51].

At ultralow temperatures the scattering of two atoms can be described<sup>4</sup> by a spherically symmetric central potential, like the Lennart-Jones potential (the Li<sub>2</sub> singlet/triplet interatomic potential is shown as an example in figure 2.3). This simplifies calculations dramatically but still captures the most important effects of the scattering events.

Two major regimes can be distinguished: At distances on the order of the Bohr radius  $a_0$ , the electron clouds of both atoms repel each other, leading to a strongly repulsive 'hard-core' part of the potential. At distance much larger than the Bohr radius  $a_0$ , the weakly attractive van-der-Waals interaction  $\propto -\frac{C_6}{r^6}$  governs the interaction potential.

The Pauli principle does not only lead to the quantum statistics but is also the reason for the difference between the singlet (spin of the valence electrons point in opposite directions, blue curve) and triplet configuration (spins of the two valence electrons are parallel, i.e. the atoms are in the same electronic quantum state, red curve) in the figure 2.3 as will be explained below.

---

<sup>3</sup>In the absence of atom-atom collisions there is no thermalization and cooling techniques that depend on it (e.g. evaporative cooling) do not work.

<sup>4</sup>In this approximation any magnetic dipole interactions between the two spins is neglected.

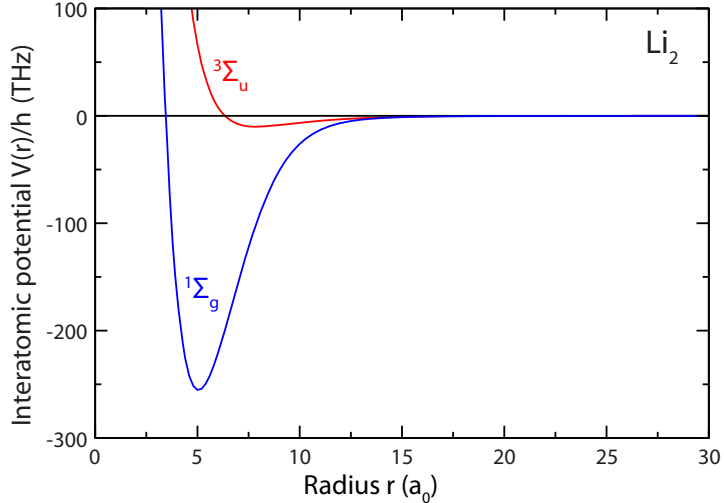


Figure 2.3: Interatomic potentials describing the collision of two fermionic  ${}^6\text{Li}$  atoms in singlet (blue) or triplet (red) configuration. Due the Pauli blocking of two electrons in the same spin configuration the triplet potential is much shallower as explained in the text. Adapted from [52].

In the framework of quantum mechanic scattering theory [49] the Schrödinger equation of a reduced one-particle problem in the center-of-mass frame of the colliding atoms is considered in momentum space:

$$(\nabla^2 + k^2) \Psi_k(\mathbf{r}) = \frac{mV(\mathbf{r})}{\hbar^2} \Psi_k(\mathbf{r}) \quad k^2 = \frac{mE}{\hbar^2} \quad (2.17)$$

The wave function  $\Psi_k(\mathbf{r})$  describes an incoming wave with momentum  $\mathbf{k}$  and a spherical scattered wave in the direction<sup>5</sup>  $\mathbf{k}' = \frac{\mathbf{k}\mathbf{r}}{r}$ :

$$\Psi_k(\mathbf{r}) \approx \underbrace{e^{i\mathbf{k}\mathbf{r}}}_{\text{incoming}} + \underbrace{f(\mathbf{k}, \mathbf{k}') \frac{e^{ikr}}{r}}_{\text{scattered part}}. \quad (2.18)$$

The scattering amplitude  $f(\mathbf{k}, \mathbf{k}')$  is the amplitude of the scattered wave relative to the incoming wave, its absolute square  $\frac{d\sigma}{d\Omega} = |f(\mathbf{k}, \mathbf{k}')|^2$  corresponds to the differential scattering cross section.

Since a central potential is considered in this approximation, the incident and scattered wave can be expanded<sup>6</sup> in partial waves with angular momentum  $l$  [51] as the scattered wave and the scattering amplitude must be both axially symmetric with respect to the incoming wave vector.

The Pauli principle requires any fermionic wave function to be anti-symmetric, such that only odd partial waves with  $l = 1, 3, 5, \dots$  contribute to the total scattering amplitude of a collision

<sup>5</sup>Energy conservation implies that  $|\mathbf{k}| = k = k' = |\mathbf{k}'|$ .

<sup>6</sup>In the following, only the important consequences of the partial wave expansion are outlined since the detailed description and mathematical formulation is well described in various text books like for instance [49] and [51].

of two fermions in the same spin state. Accordingly, for the collision of bosons only even partial wave with  $l = 0, 2, 4, \dots$  contribute. This is the fundamental reason why the interatomic potential of two colliding fermionic atoms in the triplet configuration is much shallower than the singlet configuration like shown in figure 2.3.

At ultracold temperatures the energies and the momenta of the colliding particles are very small. Therefore it is desirable to describe the scattering of ultracold atoms in the low-energy limit, typically characterized as the regime where the incoming momentum  $k$  is much smaller than the inverse range of the potential<sup>7</sup>  $k \ll \frac{1}{r_0}$ .

In this regime  $s$ -wave scattering (partial waves with  $l = 0$ ) is by far the dominant contribution and the scattering amplitude can be described by a single quantity, the **scattering length**:

$$f(k \rightarrow 0) = -a_s := -a \quad (2.19)$$

The scattering length characterizes the low-energy scattering events completely and is independent of the incoming momenta (for detailed derivation and precise definition the reader is again referred to the cited textbooks).

As a result, in ultracold quantum gases  $s$ -wave scattering is dominant and can be characterized by the  $s$ -wave scattering length. For fermionic atoms,  $s$ -wave scattering is blocked by the Pauli principle for atoms in the same quantum state. Consequently, one has to produce mixtures of two different spin states to ensure scattering and hence thermalization in an ultracold Fermi gas.

### Control of interactions with Feshbach resonances

In the previous section the interactions of ultracold atomic gases and especially ultracold fermions have been described. A tool of major importance in the field of quantum gas research are Feshbach resonances [52] that allow to *control* the interactions of an atomic cloud by changing an external parameter like the magnetic field. These magnetic Feshbach resonances will be employed in our experiment and provide a knob to tune the interactions over a very broad range - a unique tool to simulate quantum many-body physics.

Essentially, a magnetic Feshbach resonance allows to tune the scattering length between two atomic species (not necessarily the same) by bringing the quantum mechanical state of the two colliding atoms (incoming, open channel) into resonance with a bound state (the close channel). Since these two states have different magnetic moments, their difference in energy can be tuned.

Off-diagonal coupling between these two states<sup>8</sup> coherently admixes the open channel with a bound state in the close channel, leading to a modification of the scattering length around a scattering resonance.

A detailed description of these Feshbach resonances can be found in various textbooks [53]. As a result the behavior of the scattering length around a Feshbach resonance shown in figure 2.4.

---

<sup>7</sup>Typically on the order of a few Bohr radii  $a_0$ , around  $10a_0$  for the potential shown in figure 2.3.

<sup>8</sup>The hyperfine interaction term of the Hamiltonian is non-diagonal in a basis of the total electronic spin  $\widehat{\mathbf{S}} = \widehat{\mathbf{S}_1} + \widehat{\mathbf{S}_2}$  and total nuclear spin operator  $\widehat{\mathbf{I}} = \widehat{\mathbf{I}_1} + \widehat{\mathbf{I}_2}$ .

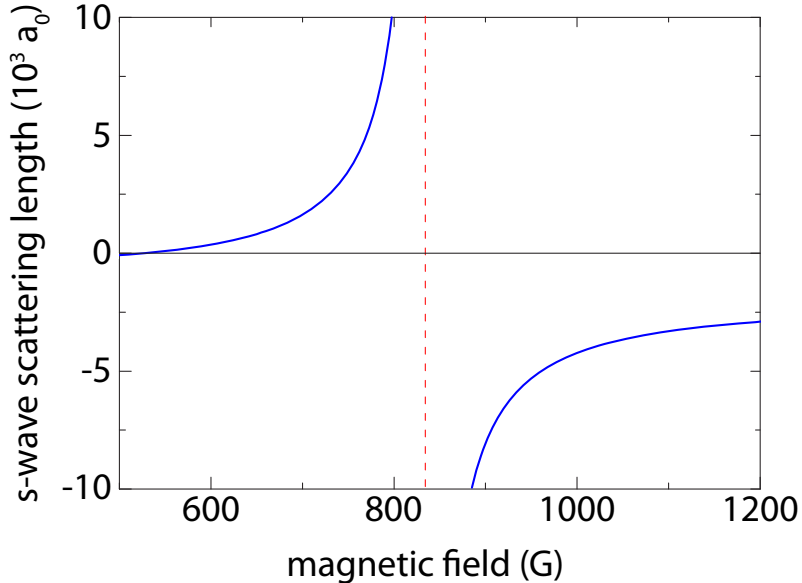


Figure 2.4: Feshbach resonances: The scattering length is plotted as function of the magnetic field around the Feshbach resonance. At the Feshbach resonance (red dashed line) the scattering length diverges.

The scattering length diverges at a Feshbach resonance according to

$$a_s(B) = a_{\text{BG}} \left( 1 - \frac{\Delta}{B - B_0} \right), \quad (2.20)$$

where  $a_{\text{BG}}$  is the background scattering length describing the interactions without an external magnetic field,  $B_0$  the position and  $\Delta$  the width of the Feshbach resonance.

Now, it is possible to investigate spin-mixtures of ultracold fermions in different interaction regimes. A positive scattering length corresponds to repulsive interactions and a negative scattering length to attractive interactions, respectively. Feshbach resonances allow to tune the interactions smoothly, which triggered especially the investigation of the BEC-BCS crossover in ultracold Fermi gases (see details in chapter 3).

## 2.2 Optical lattice potentials

One important milestone that pushed forward the idea of simulating condensed-matter systems with ultracold quantum gases was the concept of confining atoms in optical lattice potentials [25]. These optical lattice potentials - mostly referred as optical lattices - are made up by overlapping laser beams with constant phase difference which leads to constructive interference and a standing wave. Optical lattices can be used to mimic periodic structures like in a solid.

### 2.2.1 Conservative and dissipative light forces

Illuminating atoms with laser light results in dissipative and conservative light forces. The absorption of a photon from the laser beam followed by the spontaneous re-emission of photon in a random direction leads to a dissipative light force because it transfers momentum. Different concepts have been developed on top of dissipative light forces, most important the technique laser cooling [54] and magneto-optical traps [55].

Conservative light forces give rise to an optical dipole potential due to the interaction of the induced dipole moment of the atom with the light, which shifts its potential energy. Optical dipole potentials are known to be a very handy to trap neutral atoms in so-called optical dipole traps ([56], [57] and [58]) and creating optical lattices by generating a standing light wave [25].

### 2.2.2 The oscillator model

Placing a neutral atom into a coherent light field oscillating at a frequency  $\omega$  leads to an induced dipole moment that oscillates at the same frequency  $\omega$  [58]. The laser light field can be described by the complex oscillating electrical field ( $\hat{\vec{e}}$  is the unit polarization vector and  $E_0$  the amplitude):

$$\vec{E}(\vec{r}, t) = \hat{\vec{e}} E_0(r) [\exp(-i\omega t) + \text{c.c.}] . \quad (2.21)$$

The induced dipole moment can be related to the electric field with the complex polarizability  $\alpha$ :

$$\vec{p}(\omega) = \alpha(\omega) \vec{E}(\omega) . \quad (2.22)$$

The interaction potential between the induced dipole moment and the driving electric field is now given by

$$U_{\text{dip}} = -\frac{1}{2} \left\langle \vec{p} \cdot \vec{E} \right\rangle_{\text{av}} \quad (2.23)$$

where  $\langle \dots \rangle_{\text{av}}$  denotes the time average over rapidly oscillating terms.

With the electric field intensity  $I = 2\epsilon_0 c |E_0|^2$  the **conservative** interaction potential can be expressed as

$$U_{\text{dip}} = -\frac{1}{2\epsilon_0 c} \text{Re}(\alpha) I , \quad (2.24)$$

which now depends on the real part of the polarizability (the dispersive part which are the components in-phase with the laser light field) and the light intensity. By taking the negative gradient of the interaction potential the dipole force can be calculated, assuming a spatially varying light field intensity  $I(r)$ :

$$\vec{F}_{\text{dip}}(r) = -\nabla U_{\text{dip}}(r) = \frac{1}{2\epsilon_0 c} \text{Re}(\alpha) \nabla I(r) \quad (2.25)$$

This is a conservative potential proportional to the gradient of the driving electrical field.

On the other hand the imaginary part of the polarizability leads to absorption and subsequent spontaneous re-emission of photons, the **dissipative** part. Since the absorbed power from the light field is

$$P_{\text{abs}} = \left\langle \dot{\vec{p}} \cdot \vec{E} \right\rangle = 2\omega \text{Im}(pE_0^*) = \frac{\omega}{2\epsilon_0 c} \text{Im}(\alpha)I, \quad (2.26)$$

the scattering rate of photons is

$$\Gamma_{\text{sc}} = \frac{P_{\text{abs}}}{\hbar\omega} = \frac{1}{\hbar\epsilon_0 c} \text{Im}(\alpha)I. \quad (2.27)$$

A classical description of the polarizability can be obtained by considering an atom which is elastically bound to electron with an oscillator frequency  $\omega_0$  and driven by the force of the external electric field  $-eE(t)$ . Introducing a damping term due to the dipole radiation of the oscillating electron with

$$\Gamma_\omega = \frac{e^2 \omega^2}{6\pi\epsilon_0 m_e c^3} \quad (2.28)$$

yields the equation of motion

$$\ddot{x} + \Gamma_\omega \dot{x} + \omega_0^2 x = -\frac{eE(t)}{m_e}. \quad (2.29)$$

This is the so-called *Lorentz oscillator model*, the solution for the polarizability is given by ( $\omega_0$  denotes the resonance frequency)

$$\alpha(\omega) = \frac{e^2}{m_e} \frac{1}{\omega_0^2 - \omega^2 - i\omega\Gamma_\omega}, \quad (2.30)$$

which is usually expressed by using the on-resonance damping rate  $\Gamma = \frac{\omega_0^2}{\omega^2} \Gamma_\omega$ ,

$$\alpha(\omega) = 6\pi\epsilon_0 c^3 \frac{\frac{\Gamma}{\omega_0^2}}{\omega_0^2 - \omega^2 - i\frac{\omega^3}{\omega_0^2} \Gamma}. \quad (2.31)$$

By considering the quantum mechanic nature of the atom, simplified in a picture with a ground state  $|g\rangle$  and an excited state  $|e\rangle$ , a semi-classical approach leads to a damping rate which is proportional to the square of the quantum mechanical expectation value of the dipole operator:

$$\Gamma = \frac{\omega_0^3}{3\pi\epsilon_0 \hbar c^3} |\langle e | \mu | g \rangle|^2. \quad (2.32)$$

This semi-classical damping rate corresponds to the spontaneous decay rate of the excited state to the ground state, which sets the line-width of the transition. One important feature of the semi-classical picture (and the fully quantized picture as well) is saturation, i.e. the excited state becomes populated and does not immediately decay to the ground state due to a final lifetime of the upper state.

However, in the limit of low saturation one can ignore the population of excited state and the polarizability is exactly the same in the classical and in the semi-classical picture.

### 2.2.3 Dipole potential and scattering rate

With the expressions for the polarizability 2.31 obtained from the oscillator model one obtains the following explicit expressions for the optical dipole potential and the scattering rate in the limit of large detuning and negligible saturation:

$$U_{\text{dip}}(r) = \frac{3\pi c^2}{2\omega_0^3} \left( \frac{\Gamma}{\omega_0 - \omega} + \frac{\Gamma}{\omega_0 + \omega} \right) I(r) \quad (2.33)$$

$$\Gamma_{\text{sc}}(r) = \frac{3\pi c^2}{2\hbar\omega_0^3} \left( \frac{\omega}{\omega_0} \right)^3 \left( \frac{\Gamma}{\omega_0 - \omega} + \frac{\Gamma}{\omega_0 + \omega} \right)^2 I(r) \quad (2.34)$$

If the laser light detuning  $\Delta = \omega_0 - \omega$  is small compared to the transition frequency ( $|\Delta| \ll \omega_0$ ), one can neglect the terms proportional to  $\frac{1}{\omega+\omega_0}$  in the rotating-wave-approximation [59]:

$$U_{\text{dip}}(r) = \frac{3\pi c^2}{2\omega_0^3} \frac{\Gamma}{\Delta} I(r) \quad (2.35)$$

$$\Gamma_{\text{sc}}(r) = \frac{3\pi c^2}{2\hbar\omega_0^3} \left( \frac{\Gamma}{\Delta} \right)^2 I(r) \quad (2.36)$$

It is important to note that the optical dipole potential is proportional to  $\frac{I(r)}{\Delta}$ , whereas the scattering rate is proportional to  $\frac{I(r)}{\Delta^2}$ . Since inelastic scattering of photons with atoms deposits the photon recoil energy in the sample of atoms, it leads to heating of the atoms. In order to reduce heating one can suppress the (inelastic) scattering very effectively by choosing a larger detuning and a higher intensity of the light field.

### 2.2.4 Blue and red detuning of dipole traps

The optical dipole potential is positive for a positive detuning  $\Delta > 0$  (usually referred as *blue detuning*), which gives rise to a repelling force for the atoms since the potential energy in the center of the laser light beam is higher. Similarly, a negative detuning  $\Delta < 0$  (*red detuning*) leads to a negative potential energy, the atoms are attracted by the light field towards the point of highest light intensity.

Both the red- and blue-detuned dipole traps have been implemented. However, blue-detuned traps require a laser beam which has a local intensity minimum. This is practically more complicated than a laser beam with an intensity maximum (e.g. the zeroth order mode of a Gaussian beam).

The heating rates for red and blue detuned differ by [58]

$$\frac{\dot{T}_{\text{blue}}}{\dot{T}_{\text{red}}} \propto \frac{k_B T}{U_{\text{dip}}} \quad (2.37)$$

Essentially, for very deep trapping potentials a blue detuned optical dipole trap features a lower heating rate<sup>9</sup>.

---

<sup>9</sup>Here, the dependence on the ratio of kinetic to potential energy has been neglected, a detailed treatment can be found in the given reference [58].

### 2.2.5 Dressed atom picture

Another approach is the *dressed atom picture*, in which a two-level atom and a quantized light field is considered ([60] and [61]). Starting with  $n$  photons of the energy  $\hbar\omega$  and an atom in the atomic ground state, the ground state of the combined system has the energy

$$E_g = n\hbar\omega, \quad (2.38)$$

where the atomic ground state energy is zero. When the atom absorbs a photon (transition frequency  $\omega_0$ ), the total energy is

$$E_e = \hbar\omega_0 + (n - 1)\hbar\omega. \quad (2.39)$$

By using perturbation theory one can calculate the effect of the interaction. For two non-degenerate unperturbed states the energy shift due to the dipole interaction  $H_{\text{int}} = -\vec{\mu}\vec{E}$  is

$$\Delta E_{e/g} = \frac{|\langle e | -\vec{\mu}\vec{E} | g \rangle|^2}{\pm(E_e - E_g)}. \quad (2.40)$$

Using the expression for the damping rate 2.32,  $I = 2\epsilon_0 c |E|^2$  and  $E_e - E_g = \hbar\Delta = \hbar(\omega - \omega_0)$  the energy shift reads

$$\Delta E_{e/g} = \frac{|\langle e | \mu | g \rangle|^2 |E|^2}{\pm\hbar\Delta} = \pm \frac{3\pi c^2}{2\omega_0^3} \frac{\Gamma}{\Delta} I. \quad (2.41)$$

This is usually referred as the *AC Stark shift* or the Autler-Townes effect [62]. The AC Stark shift for the ground state is exactly equal to the optical dipole potential obtained in the semi-classical approach with the rotating-wave approximation. This result is not very surprising, since it was obtained in the limit of low saturation, that is that the atom resides most of the time in the ground state and the upper state population can be neglected. Hence, the light-shifted ground state of an atom can be seen as the relevant potential.

## 2.3 Optical dipole traps

As described in the previous sections, the optical dipole potential is proportional to the intensity of the laser light. A Gaussian laser beam has a spatially varying intensity

$$I(r, z) = I_0 \left( \frac{w_0}{w(z)} \right)^2 \exp \left( -\frac{2r^2}{w^2(z)} \right) = \frac{2P}{w^2(z)\pi} \exp \left( -\frac{2r^2}{w^2(z)} \right) \quad (2.42)$$

where

$$w(z) = w_0 \sqrt{1 + \left( \frac{z}{z_R} \right)^2} \quad (2.43)$$

is the beam waist at position  $z$  ( $\frac{1}{e^2}$  radius),  $z_R = \frac{\pi w_0^2}{\lambda}$  the Rayleigh range and  $P$  the total laser power.

As a consequence of equation 2.36 red-detuned Gaussian beam can be used to trap neutral atoms in the intensity maxima. These optical dipole traps for neutral atoms created by Gaussian beams

are one of the workhorses for trapping ultracold quantum gases. A main advantage is that the trapping potential does not depend on the magnetic field, which enables one to use optical dipole trap for trapping atoms and Feshbach resonances [52] to tune the interaction at the same time by varying the magnetic field.

By expanding the exponential function in 2.42 the following approximation can be obtained [43]:

$$V_{dip}(r, z) \approx -V_0 \left[ 1 - 2 \left( \frac{r}{\omega_0} \right)^2 - \left( \frac{z}{z_R} \right)^2 \right]. \quad (2.44)$$

Then, the potential can be expressed in term of following trapping frequencies

$$\omega_r = \sqrt{\frac{4V_0}{m\omega_0^2}} \quad (2.45)$$

$$\omega_z = \sqrt{\frac{2V_0}{mz_R^2}}. \quad (2.46)$$

Since the radial confinement is typically much larger than the axial confinement, one usually applies additional axial confinement. This additional confinement can be provided by an optical dipole trap along another axes (so-called *crossed optical dipole trap*) or by superimposing a magnetic trap (a magneto-optical *hybrid trap*).

## 2.4 Creation of optical lattices

An optical lattice can be created by retro-reflecting a laser beam at a mirror as figure 2.5 shows, resulting in a standing electromagnetic wave. A Gaussian laser beam of wavelength  $\lambda$  creates a periodic potential of the form<sup>10</sup>

$$V_{1D} = V_0 \exp \left[ -\frac{2r^2}{\omega_r^2} \right] \cos^2(kz) \quad (2.47)$$

where  $k = \frac{\lambda}{2\pi}$  is the wave vector of the laser beam and  $V_0$  is the depth of the potential. Hence, an optical lattice potential in one dimension with periodicity  $a = \frac{\lambda}{2}$  is created.

### 2.4.1 Rectangular geometries

It is conceptually easy to create a cubic lattice by crossing three standing-wave laser beams orthogonally. Typically one chooses a laser wavelength that is far detuned with respect to the atomic transitions of the atoms to reduce heating.

To avoid any interference of these beams along three different axes, one can choose orthogonal linear polarizations of these beams. Another trick often applied to avoid interference due to imperfect polarizations of the beams is to shift the frequencies of the beams with respect to each other by some tens of MHz, which leads to rapidly oscillating interference terms that time-average to zero. These frequency differences are much smaller than the detuning from the atomic transition and therefore the atom will experience the same potential depth.

---

<sup>10</sup>Several simplifications have been made here: The overall confining shape of the Gaussian beam is not fully taken into account (the axial dependence of  $\omega_r(z)$  has been dropped) and any imperfections of the optical elements that are used to create the Gaussian beam and retro-reflect it have been omitted (e.g. the reflectivity of mirrors and the transmission of lenses is typically not unity in real experiments).

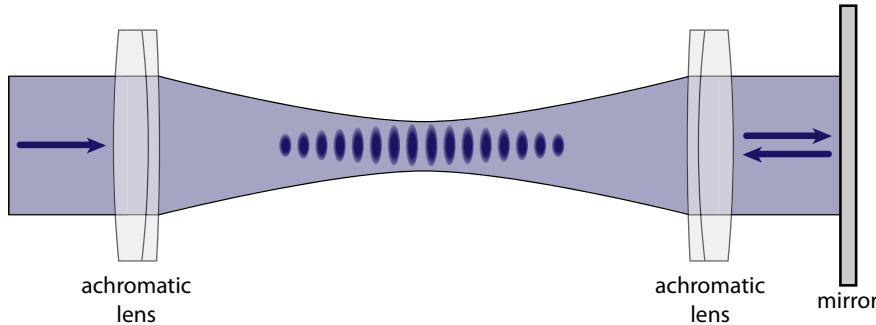


Figure 2.5: Creation of a 1D optical lattice: By reflecting and overlapping a laser beam a standing light wave can be created, which corresponds to a periodic optical potential. The two lenses create a Gaussian beam which enhances the depth of the potential due to the higher light intensity in the focus of the beam.

## 2.5 Band structure

Similar to the band structure of condensed matter materials a band structure emerges from the periodic potential. A very common lattice system is the three-dimensional cubic lattice for which the movement along all three directions can be treated independently.

In a single-particle quantum mechanical treatment a particle subject to a periodic potential  $V(r)$  can be described by the solutions of the Schrödinger equation

$$\hat{H}\phi_q^{(n)}(x) = E_q^{(n)}\phi_q^{(n)}(x) \quad \hat{H} = \frac{\hat{p}^2}{2m} + V(x). \quad (2.48)$$

The Bloch theorem [63] states that the solution for a periodic potential with lattice period  $a$  is the product of plane waves solutions  $e^{\frac{iqx}{\hbar}}$  with the quasi-momenta  $q$  and a function of the same periodicity as the lattice  $u_q^{(n)}(x) = u_q^{(n)}(x + a)$ .

With this ansatz  $\phi_q^{(n)} = e^{\frac{iqx}{\hbar}} u_q^{(n)}(x)$  the Schrödinger equation becomes an eigenvalue problem for  $u_q^{(n)}(x)$  [43]:

$$\hat{H}_q u_q^{(n)}(x) = \left( \frac{1}{2m} (\hat{p} + q)^2 + \hat{V}(x) \right) = E_q^{(n)} u_q^{(n)}(x). \quad (2.49)$$

Due to the same periodicity the periodic potential and the functions  $u_q^{(n)}(x)$  can be expanded in terms of the discrete momenta yielding the discrete Fourier sums

$$V(x) = \sum_{r \in \mathbb{Z}} V_r e^{2ikrx} \quad u_q^{(n)}(x) = \sum_{s \in \mathbb{Z}} c_{s,q}^{(n)} e^{i2ksx}. \quad (2.50)$$

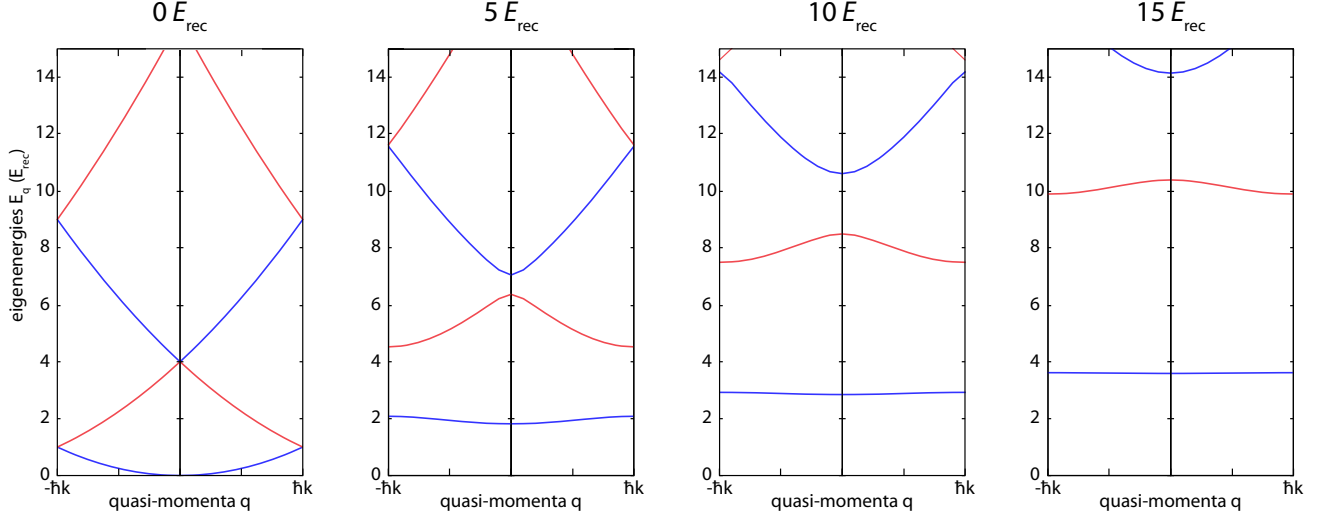


Figure 2.6: Bloch bands for a free particle (left graph) and for a one-dimensional lattice for three different lattice depths given in terms of the lattice recoil energy  $E_R$ . A quadratic dispersion of a free particle is obtained for no lattice, whereas for increasing lattice depth gaps open up in the Bloch bands.

The functions  $\phi_q^{(n)}(x)$  can therefore be expanded in terms of plane waves with wave vectors  $\frac{q}{\hbar} + 2ks$  where  $2ks$  correspond to the reciprocal wave lattice vectors in the Fourier sum in equation 2.50.

Because of the periodicity of the wave vectors the quasi-momenta have a periodicity of  $2\hbar k$  and the Bloch functions are restricted to the interval  $]-\hbar k, +\hbar k]$  called the *first Brillouin zone*.

By inserting the Fourier sums into the Schrödinger equation the Hamiltonian can be diagonalized numerically. The resulting eigenvalues as a function of quasi-momenta  $q$  are called Bloch bands and are shown in figure 2.6: With no lattice present, the quadratic dispersion of a free particle is recovered. When the lattice potential is turned on, gaps in the Bloch bands emerge. For a deeper lattice the band gaps increase.

A characteristic quantity in which the lattice depth (magnitude of the potential  $V(x)$ ) is measured is the recoil energy of the lattice laser light:

$$E_R = \frac{\hbar k_{\text{lat}}^2}{2m} = \frac{\hbar^2}{2m\lambda_{\text{lat}}^2}. \quad (2.51)$$

In lattice experiments with ultracold atoms one typically works in the lowest Bloch band (lowest blue band in figure 2.6) as the energies at ultracold temperatures are very small. Then, the population in the higher bands can be neglected.

---

### 3. Emulating condensed matter system with ultracold fermions

---

In this chapter recent developments in the field of ultracold atoms is briefly reviewed particularly in regard of this experiment. Since this works aims at the construction of a quantum gas microscope for fermionic atoms while still being compatible to work with some bosonic species, the scope of this experiment is wide.

Being in a very early construction stage of a typical ultracold atom experiment, the plans for the future research on this experiments are vague and can change quickly, especially in rapidly moving field of ultracold quantum gases. Because of the complexity these experiments typically exists for many years, often more than a decade. This chapter demonstrates the variety of phenomena that this experiment could explore.

#### 3.1 The Fermi-Hubbard model

When bosonic atoms in optical lattice were examined, the Bose-Hubbard model was developed [25] based on an earlier work by J. Hubbard developed to explain electron correlations in narrow energy bands in condensed matter physics [64]. Essentially, the Fermi-Hubbard model [65] is an extension of the Bose-Hubbard model that describes a two-component gas of fermionic atoms in the lowest band of an optical lattice in a very simple way<sup>1</sup>.

The central part is the Fermi-Hubbard Hamiltonian

$$\mathcal{H}_{\text{FH}} = -t \sum_{\langle i,j \rangle, \sigma \in \{\uparrow, \downarrow\}} (\hat{c}_{i,\sigma}^\dagger \hat{c}_{j,\sigma} + \text{h.c.}) + U \sum_i \hat{n}_{i,\uparrow} \hat{n}_{i,\downarrow} + \sum_i \epsilon_i \hat{n}_i \quad (3.1)$$

which describes three different energy contributions:

The first term describes the kinetic energy which is proportional to a tunneling matrix element  $t$  between two adjacent lattice sites. The operators  $\hat{c}_{i,\sigma}^\dagger$  and  $\hat{c}_{j,\sigma}$  denote in the formalism of field quantization the annihilation of a particle with spin  $\sigma$  on lattice site  $j$  and the creation of a particle on an adjacent lattice site  $i$  and hence the tunneling from site  $j$  to  $i$ .

The second term is proportional to the on-site interaction and describes interactions at a specific lattice site  $i$  between two fermions in different spin states (denote here with  $\uparrow$  and  $\downarrow$ ). The interaction depends on the number of atoms in both states on that specific lattice, denoted by  $\hat{n}_{i,\uparrow}$  and  $\hat{n}_{i,\downarrow}$ .

Since in any typical lattice experiment an overall confinement in addition to the lattice (for instance created by the Gaussian intensity profile of the lattice laser beams or an additional

---

<sup>1</sup>For instance, second-order tunneling effects are neglected.

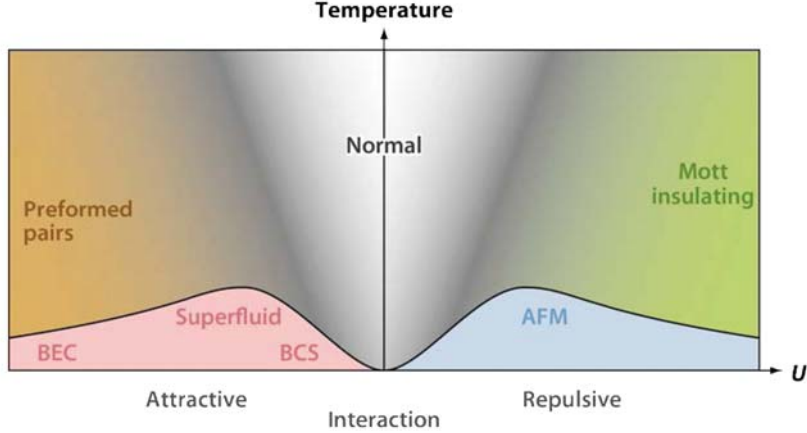


Figure 3.1: Schematic phase diagram for the Fermi-Hubbard model a half-filling for simple cubic lattice in three dimensions, adapted from [66]. AFM denotes the antiferromagnetically ordered phase. On the attractive side of the diagram  $s$ -wave superfluidity with a BEC-BCS crossover is expected.

magnetic trap) is present and confines the atomic cloud, the potential energy of each lattice site in that confinement is given by  $\epsilon_i$  and contributes in the last term of the Fermi-Hubbard Hamiltonian.

The advantage of this simple model is that now there are only two free parameters,  $U$  and  $t$  (the latter one is sometimes also called  $J$ ) which can be tuned easily in an experiment. Tuning the lattice depth varies the tunneling matrix element  $t$  whereas Feshbach resonances can be used to tune the interactions and hence the on-site interaction  $U$ .

It should be noted that the on-site interactions does not only depend on the external magnetic field driving the Feshbach resonance but also on the lattice depth since interactions are enhanced in a tight confinement. This manifests in the fact that the interaction matrix element  $U$  can be approximated as

$$U = \frac{4\pi a_s}{m} \int d^3r |w(\mathbf{r})|^4, \quad (3.2)$$

where  $a_s$  is the  $s$ -wave scattering length for no confinement and  $w(\mathbf{r})$  the Wannier function localized on a specific lattice site. Thus, in deep lattice the interactions are enhanced due to the confinement.

Depending on the different values of  $t$  and  $U$ , several different regimes can be accessed. At the end only the ratio of the tunneling energy and the interaction energy matters for the description of the different regimes. The predicted phase diagram for two fermionic species with an average of one particles per lattice site is shown in figure 3.1.

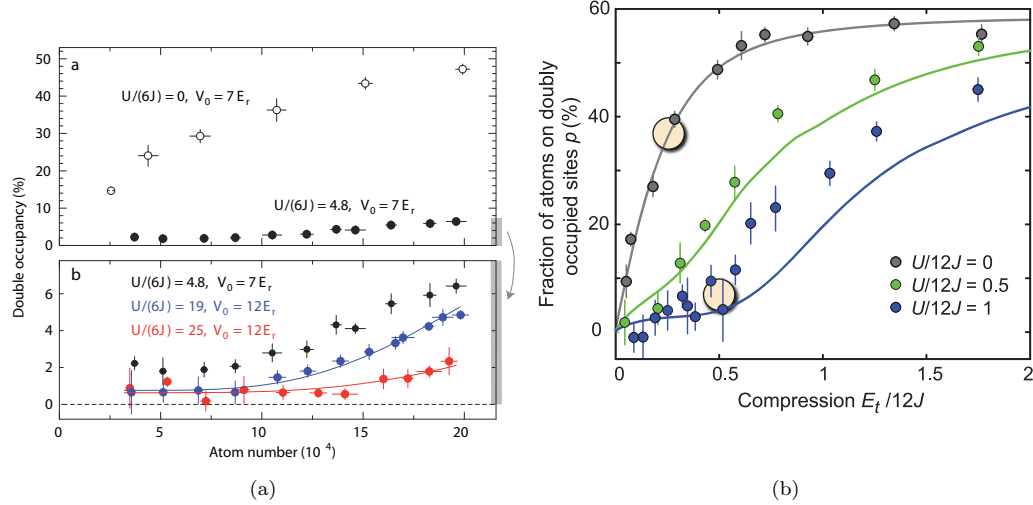


Figure 3.2: Double occupancy as function of atom number from [30] in (a) and compression of the trapping potential from [31] in (b). When repulsive interactions are present, the double occupancy is strongly suppressed.

### 3.1.1 Mott insulator of fermionic atoms

A good example for the new many-body physics emerging from the interplay of interactions and localization is the formation of a Mott insulating phase in fermionic atoms in an optical lattice. In a Mott insulator, interactions are strong and repulsive, such that the double occupancy of a lattice site is very costly. As a consequence, all lattice sites are occupied with exactly one atom - a Mott insulator - until it becomes energetically favorable to occupy the lattice sites with more than one atom.

Mott insulating phases occur not only in optical lattices, but also in condensed matter physics providing a perfect analogy. This Mott insulating phase can be engineered and the transition from the normal phase (often called the metallic phase in analogy to the delocalized electron gas in metal) has been observed.

So far the Mott insulating phase has been observed by measuring the double occupancy [30] and the compressibility [31] across the transition, shown in figure 3.2a and 3.2b, respectively.

In addition, the excitation spectrum of the Mott insulating phase was reported to show a gapped behavior [30], another signature of a Mott insulator<sup>2</sup>.

Although these measurements provide good evidence for the observation of a Mott insulating

<sup>2</sup>A specific amount of energy corresponding to the repulsive interaction energy is needed to excite atoms from the Mott insulator.

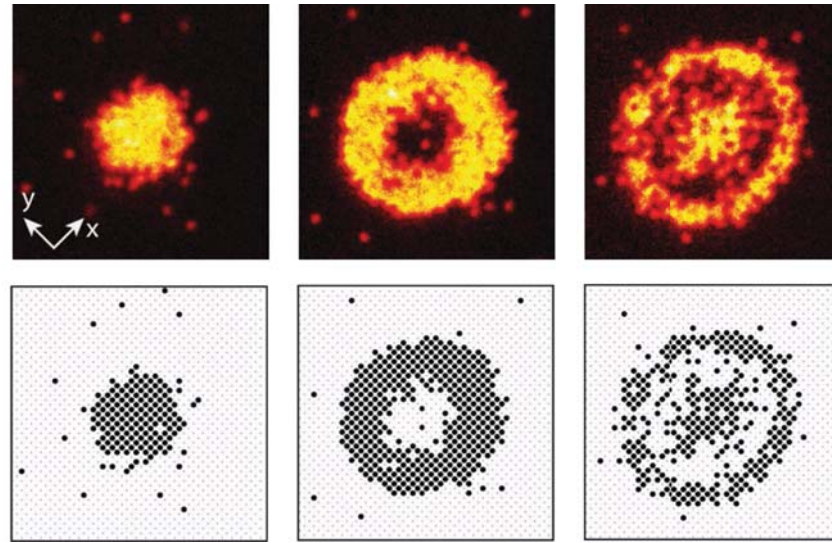


Figure 3.3: In-situ images and reconstructed occupation numbers of **bosonic** Mott insulators with three different fillings (right three columns) in a two-dimensional optical lattice. Figure adapted from [32].

phase, a direct observation of a fermionic Mott insulator seems to be possible. As mentioned in the introduction in chapter 1, two groups already realized in-situ imaging of a bosonic Mott insulator shown in figure 3.3.

Thus, there is no conceptual difficulty in observing a fermionic Mott insulator in quantum gas microscope and it seems to be a perfect proof-of-principle experiment once the fermionic quantum gas microscope has been constructed and is ready to work.

### 3.1.2 Insulating phases

Beside the Mott insulating phase with exactly one atom per lattice there is also the band insulating phase, where exactly two fermions in different spin states occupy a lattice site as depicted in figure 3.4.

Similar to a Mott insulator, the occupation with more than two different fermions is energetically very costly, but this time for a different reason: The Pauli principle forbids more than one fermion of the same spin state in one of the lattice bands. Thus, only the next higher band can be populated.

In quantum gases the behavior of both insulating phases can be studied in a very clean environment. Effects from multiple bands, impurities and long-range effects of the Coulomb interactions are especially relevant close the metal-to-band-insulator transition and the detailed study of the different insulating phases of interacting fermions in lattices is a very insightful topic.

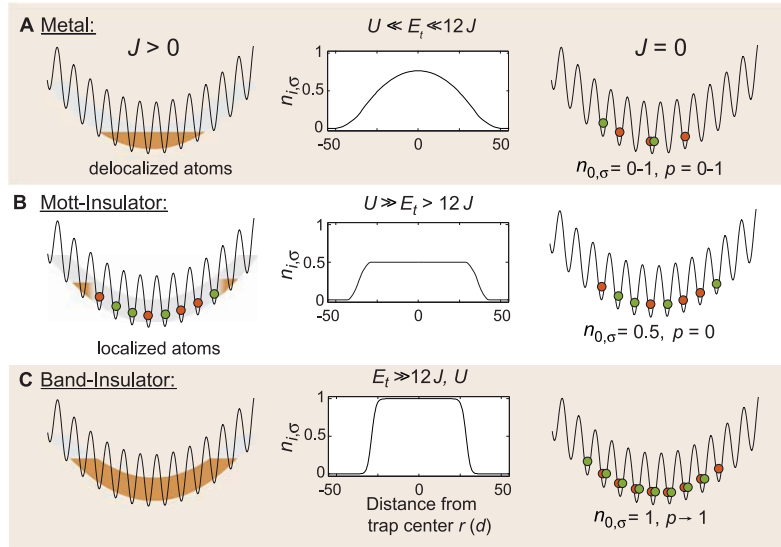


Figure 3.4: The metallic, Mott-insulating and band-insulating phase of a Fermi gas in an optical lattice: The left column illustrates the behavior with allowed tunneling, the center column the corresponding density distribution and the right column the 'freezing' of the different phases in the zero-tunneling limit (very deep lattice). Figure adapted from [31].

### 3.2 Antiferromagnetically ordered phase

Figure 3.1 indicates already that the Mott insulating state is not the ground state of repulsively interacting fermions in an optical lattice as one might think intuitively.

Instead, second order tunneling processes (essentially tunneling from one lattice site to neighboring site and back) are present, sometimes called virtual tunneling processes. Their energy contribution is  $\frac{t^2}{U}$  and give rise to the fact that the ground state of the repulsive Fermi-Hubbard model is the antiferromagnetically ordered phase (AFM).

This AFM phase can be considered as one of milestones on the road towards explaining high-temperature superconductivity which is one of the premier problems that is hoped to be solved with the help of ultracold quantum gases.

The reason for the relevance of the AFM phase is visible in predicted phase diagram of a repulsively interacting Fermi gas in a lattice with filling less than unity, shown in figure 3.5: The AFM phase and the  $d$ -wave superconducting phase are believed to be the ground states for different filling factors in presence of a lattice.

To make the connection to condensed matter physics, a filling factor of less than unity can be also seen as 'hole-doping'. Then, the similarity to the phase diagram of doped high-temperature superconductors in figure 3.7 becomes apparent. A detailed study of the AFM phase with

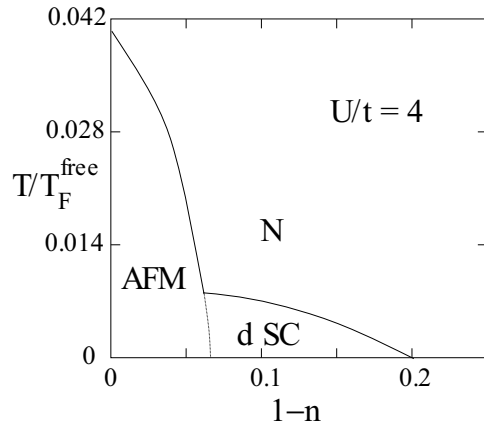


Figure 3.5: Theoretically predicted phase diagram of fermions in an optical lattice showing the temperature/hole-doping concentration plane, from [38].

quantum gases in optical lattices is believed to be an important puzzle piece, as one only needs to vary the number of atoms per lattice to get to the regime of doped superconductors.

Unfortunately, the AFM phase could not be observed so far. The major problem is that the needed temperatures of the initial atomic cloud (before loading it into the optical lattice) are very low in order to ensure a low entropy per particle for forming the AFM phase [67].

Different approaches like for instance interaction-induced adiabatic cooling [68] have been made, but so far no observation of the AFM phase could be made.

A quantum gas microscope might be the ideal tool to detect the AFM phase for two reasons. First, it does not rely on bulk measurements like the detection via Bragg scattering [69] where the measured quantities are mostly obtained by averaging the quantity over the whole atomic cloud. A quantum gas microscope might be able to observe an onset of the AFM phase directly in in-situ images even before any bulk measurement shows a signal.

Second, the advances in quantum gas microscopy might allow not only a single-site single-atom resolved imaging but might also provide more tools to cool to even lower temperatures. A part of this progress is summarized in section 3.4.

Already bosonic quantum gas microscope showed how one can look specially at regions of high or low entropy as figure 3.6 illustrates: The lower graph shows the square atom fluctuations and the small inset the entropy density in the system. The quantum microscope might therefore be the better tool to probe the AFM phases, as it is expected to be more sensitive and the direct measurement can provide evidence free of doubt.

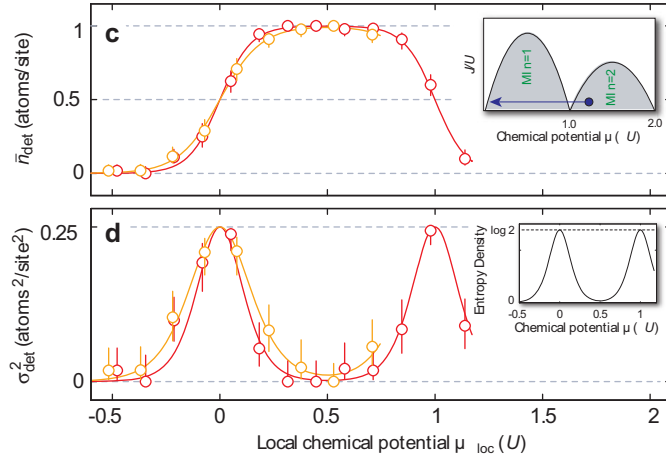


Figure 3.6: Radial atom number occupation and fluctuations as function of local chemical potential observed by the bosonic quantum gas microscope. The lower inset shows the distribution the entropy density in the measured sample. Figure adapted from [31].

### 3.3 The quest for high-temperature superconductivity

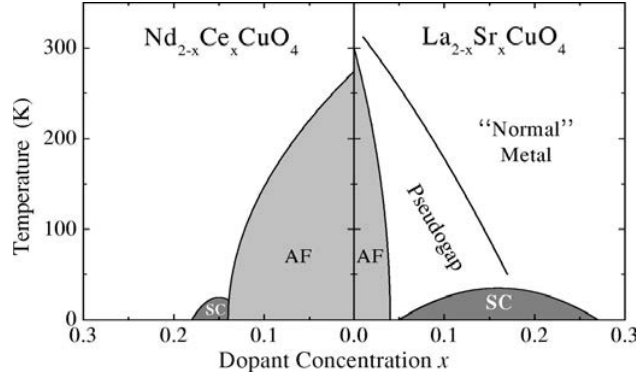


Figure 3.7: Phase diagram of cuprate superconductors for electron- (left side) and hole-doping (right side), adapted from [70].

In the previous section the connection to the high-temperature superconductivity was already mentioned. Particularly,  $d$ -wave super-fluidity is supposed to give rise to the superconductivity in the cuprates [71].

Shortly after the realization of optical lattices it was realized that doping plays a major role in these phenomena [72]. Already since the beginning of the idea of optical lattices for ultracold atoms [25], but especially in the last years after the realization of a fermionic Mott insulator in

optical lattices it is believed that ultracold quantum gases are one of the most promising approaches to explain these phenomena, which has been tried for years and many papers have been written on it<sup>3</sup>.

The experiment described in this work maybe a good tool for further investigation on this topic as it provides not only the single-atom single-site resolution but also features a very robust but versatile optical lattice.

### 3.4 Second generation quantum gas microscopy

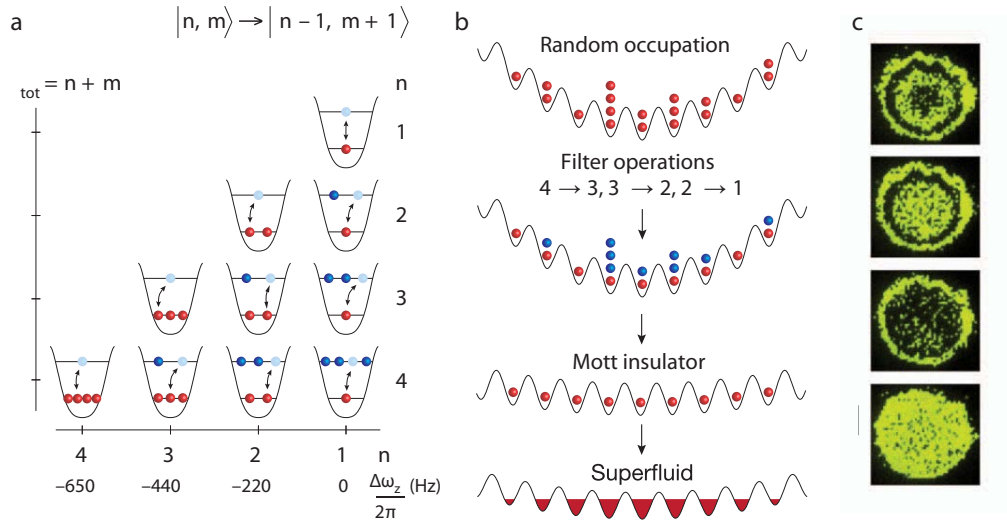


Figure 3.8: Number filtering of Mott insulator shells as reported in [74]: With an occupation-number-selective method lattice sites with  $n = 1, 2, 3, 4, \dots$  atoms are consecutively transferred into lattice sites with exactly one atom.

In the field of quantum gas microscopy the experiments being set up for fermions right now will already represent a major technological improvement over first two bosonic quantum gas microscopes. Experience is not only gained in the quite challenging diffraction-limited imaging techniques, but also new methods have been developed.

For instance, for bosons a technique has been developed that selectively changes the occupation of lattice sites with a specific atom number [74]. As a proof-of-principle experiment, Mott insulator shells with  $n = 1, 2, 3, 4$  atoms per lattice site could be converted to a  $n = 1$  Mott insulator as shown in figure 3.8.

Such manipulation tools might be used in the future to create low-entropy states, which is essentially another step towards a quantum simulator that Feynman proposed in [8].

<sup>3</sup>One of the newest candidates for room-temperature superconductivity is doped graphite [73].

### 3.5 Synthetic gauge fields and topological phases

A very recent development is the creation of synthetic gauge fields that solve a fundamental problem of ultracold atoms: Typically, the neutral atoms employed in the experiments do not exhibit magnetic interactions. Synthetic gauge fields can close this gap and open the possibility to explore magnetic effects like the quantum hall effect with neutral atoms. These techniques were pioneered for bosons [75] and very recently these techniques have been applied to fermions.

So far, a spin-orbit coupling has been realized in fermions ([76] and [77]). Ultimately, one of the targets of these developments are spin-orbit coupled lattices, in which  $p$ -wave pairing, topological superfluidity [78] and Majorona edge states [79] might be observable.



---

## 4. The Fermi gas experiment

---

The goal of this experiment is to explore the physics of fermions in the quantum-degenerate regime of ultracold temperatures and ultralow densities that can be reached by cooling dilute atomic vapors in an ultra-high vacuum (typically at  $10^{-11}$  mbar).

After the successful demonstration of a bosonic quantum gas microscope this work tries to adapt the concept to make it capable of imaging fermions at the single atom level. As explained below the novel design of this experiment enables one to load two different fermionic and one bosonic species into an optical lattice. The primary reason for the bosonic species is sympathetic cooling of the two fermionic species.

A conceptual picture of this experiment was already drawn in figure 1.2 in chapter 1. Now, the details of the quantum gas microscope realized in this work are explained and its fundamental physical layout is described. It is shown how the high-resolution imaging systems will be combined with an ultra-high vacuum (UHV) system and the general layout of the optical beam lines is presented.

Most of the mechanical design has been done using a CAD software<sup>1</sup>. In this chapter the design of the experiment is illustrated based on rendered drawings created with this software. Pictures of the already constructed portion of the experiment can found in appendix D.

### 4.1 Atomic species

For a fermionic quantum gas microscope, one has to select a fermionic atom which is easy to cool and trap. The alkali elements turned out to be a very good choice since their atomic structure allows the use of lasers in the visible part of the electromagnetic spectrum which is easily accessible with present laser technology (diode lasers). Furthermore due to the hyperfine structure of the alkali elements it is possible to choose closed cycling transitions for laser cooling, in which the atom always ends up in the same state after the cooling process.

The experiment in this work was designed for the only two stable fermionic alkali atoms, namely  $^6\text{Li}$  and  $^{40}\text{K}$ . It turns out that  $^{40}\text{K}$  is at the moment a good choice for a fermionic quantum gas microscope because it is possible to cool  $^{40}\text{K}$  atoms in the optical lattice with optical molasses [35]. It turns out that this technique is crucial for imaging single atoms in a lattice.

The standard techniques for probing ultracold quantum gases (see reviews [44] and [41]) are fluorescence and absorption imaging, where a CCD camera collects the fluorescence light or the light of the non-absorbed photons, respectively, with a typical resolution of a couple of micrometers. A quantum gas microscope, by contrast, achieves sub-micron resolution, enough for detecting single atoms in single sites of an optical lattice. The novel approach is to ramp up

---

<sup>1</sup>SolidWorks by Dassault Systèmes SolidWorks Corporation.

Property	$^6\text{Li}$	$^{23}\text{Na}$	$^{40}\text{K}$
Quantum statistics <sup>3</sup>	fermionic	bosonic	fermionic
Natural abundance [82]	7.59(4)%	100%	0.0117(1)%
Nucleons	6	23	40
Electronic structure of the ground state	$1s^2 2s^1$	$1s^2 2s^2 2p^6 3s^1$	$1s^2 2s^2 2p^6 3s^2 3p^6 4s^1$
Nuclear spin [83]	$\frac{3}{2}$	4	$\frac{3}{2}$
Atomic mass [82]	6.015122795(16) u	22.9897692809(29) u	39.96399848(21) u
Lifetime [83]	stable	stable	$1.248 \cdot 10^9$ y
Vapor pressure at 300 K [84]	$9.397 \cdot 10^{-18}$ Pa	$4.239 \cdot 10^{-8}$ Pa	$3.022 \cdot 10^{-6}$ Pa
Melting point SP [85]	180.50 °C	97.794 °C	63.5 °C
Boiling point SP [85]	1342 °C	882.940 °C	759 °C

Table 4.1: General physical properties of the atomic species used in this experiment.

the lattice to a very deep lattice potential<sup>2</sup> and cool the atoms while imaging them with a high-resolution imaging system. By imaging in this way, any tunneling of the atom to neighboring lattice sites is prevented and the atom can be imaged with several photons (typically up to 100 photons) while optical molasses cool the atoms to compensate for the heating due to photon scattering from the optical lattice and imaging light.

We expect  $^{40}\text{K}$  to be easier to cool inside an optical lattice than  $^6\text{Li}$  because cooling with optical molasses is possible. This is different for  $^6\text{Li}$ , since the excited electronic state of its hyperfine structure is not resolved by the laser light sources used in our experiments (see figure 4.1) and therefore sub-Doppler cooling is not effective. Another promising approach for  $^6\text{Li}$  experiments is Raman side-band cooling [80], but this will not be covered by this thesis. Hence, the focus of this work is a quantum gas microscope for fermionic  $^{40}\text{K}$ , although the option for  $^6\text{Li}$  has been included for future experiments.

Besides the two fermionic species, our experiment is also capable of creating ultracold clouds of  $^{23}\text{Na}$ , providing an excellent sympathetic coolant for  $^{40}\text{K}$ . Cooling of  $^{23}\text{Na}$  down to ultralow temperatures has become a standard procedure in the recent years and past experiments have proven the good collisional properties of  $^{23}\text{Na}$  with  $^{40}\text{K}$  [81], which are required for sufficient thermalization during sympathetic cooling.

Table 4.1 summarizes some important properties of these three atomic species. The hyperfine structure and the most important optical transitions used for laser cooling are shown in figure 4.1.

## 4.2 Experimental concept and cooling strategy

One of the challenges in this experiment is to combine the idea of a high-resolution imaging, which usually involves an objective with a small working distance of a couple of millimeters,

<sup>2</sup>Such a potential is typically on the order of a few thousand times the recoil energy  $E_R$ .

<sup>3</sup>The type of quantum statistics that the composite particle consisting of the nucleus and the electron obeys.

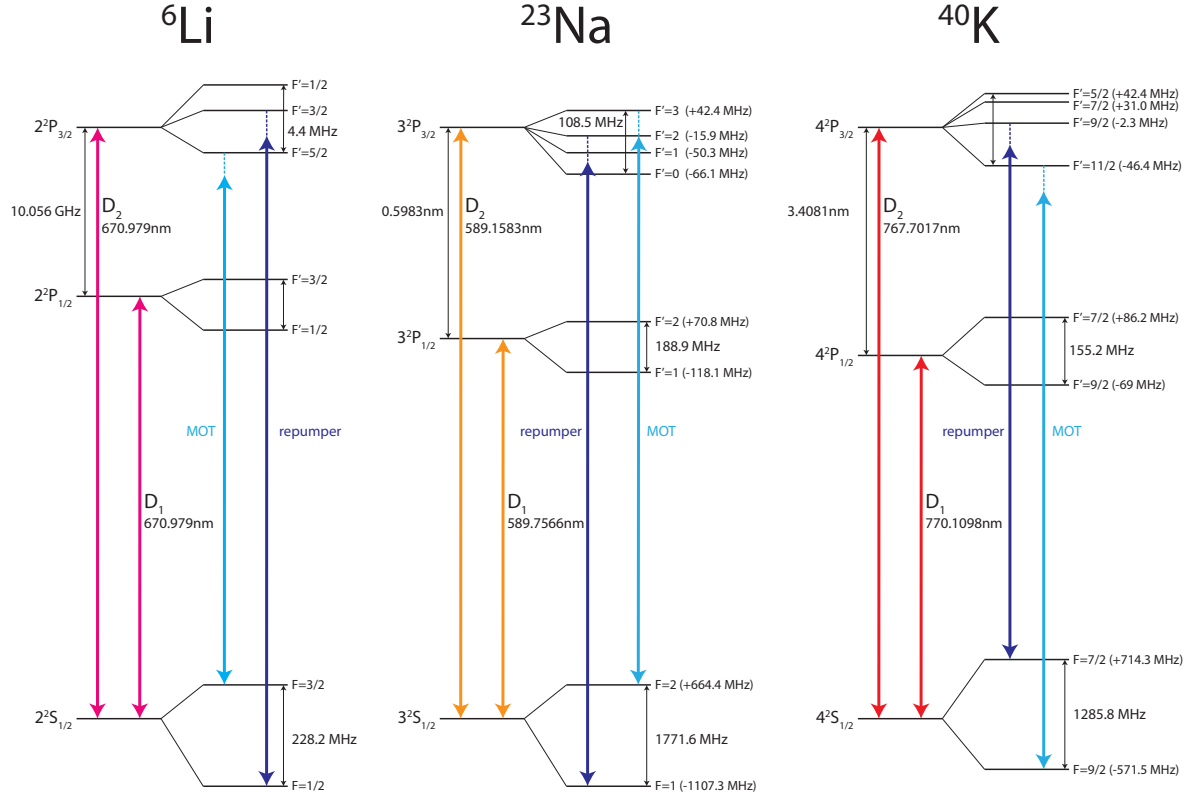


Figure 4.1: Energy level scheme showing the hyperfine structure of  ${}^6\text{Li}$ ,  ${}^{23}\text{Na}$  and  ${}^{40}\text{K}$ . The Fraunhofer  $D_1$  and  $D_2$  lines [86] as well as the transitions used for laser cooling are marked.

with the space-consuming vacuum technology that is needed to create dilute samples in ultra-high vacuum.

Additionally, very high magnetic fields are needed for trapping and tuning the interactions of the atoms by Feshbach resonances [52]. For Feshbach resonances homogeneous magnetic fields of up to 1000 G are needed, for instance for the wide  $s$ -wave Feshbach resonance in  ${}^6\text{Li}$  at around  $B_{\text{res}} = 834$  G [87]. This makes it favorable to put the magnetic coils very close to the atoms to reduce the needed current as much as possible (commercial power supplies providing currents up to  $I = 500$  A are easily available; higher current specifications involve much more technological effort), which is an important design constraint in the layout of this experiment.

Our solution is to use re-entrant viewports, essentially bucket-shaped windows which 're-enter' the vacuum chamber, placing the actual window very close to the atoms. Both the magnetic coils and the microscope objective are located inside the bucket of these re-entrant viewports, as

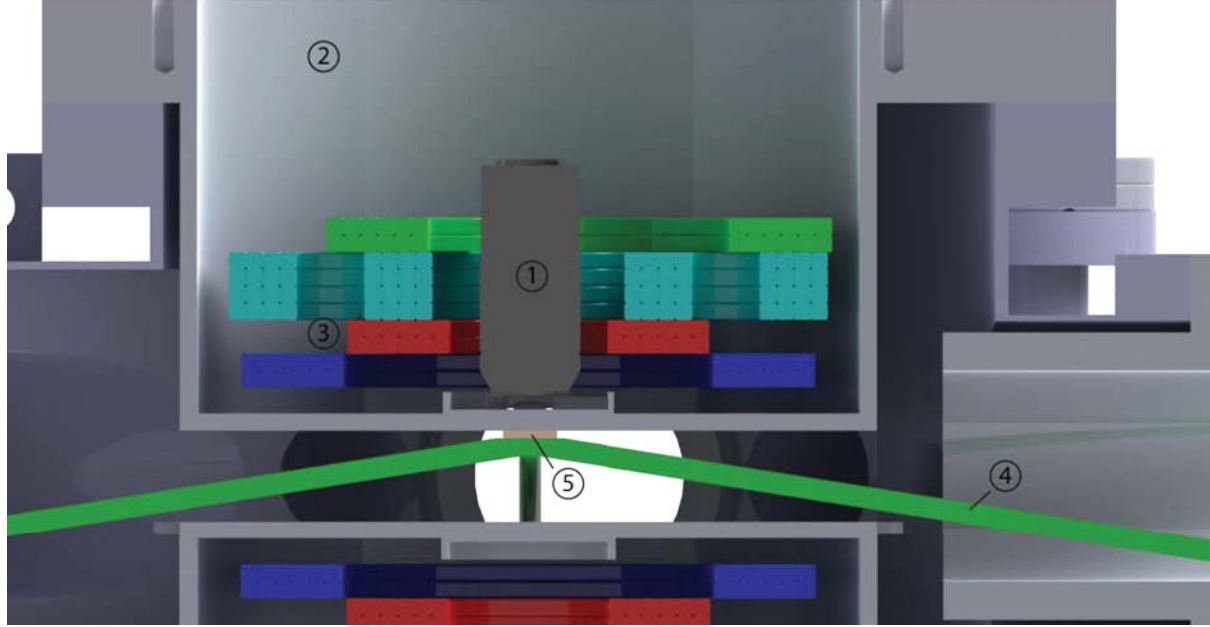


Figure 4.2: CAD illustration showing the setup of the imaging system inside of the re-entrant vacuum viewport (2) consisting of a microscope objective (1), the hemispherical lens below and the super-polished substrate (4) attached to the vacuum window inside the vacuum chamber. Around the objective the magnetic coils have been placed, symbolized by different colors (3). Lattice laser beams (5) can be reflected at the super-polished substrate, which is used for creating an optical lattice along the vertical direction. The recording camera is placed above the objective like shown in figure 4.3.

shown in figure 4.2. A key innovation is that the vacuum window together with a plano-convex lens on top and a so-called super-polished substrate attached below the window makes up a complete hemisphere and is used to enhance the resolution of the imaging system by enhancing its numerical aperture and reduce the scattering of the glass surface which is closest to atoms. More details will be given in chapter 7.

Effusive ovens make up the atomic sources inside the vacuum systems that are heated up to several hundred degrees Celsius depending on the atomic species. Then, the atoms are cooled down to a couple of tens to hundreds of micro-Kelvin with laser cooling and ultimately down to the nano-Kelvin regime using evaporative cooling.

In the laser cooling stage, the atoms are trapped in a triple-species 3D-MOT, which is loaded by a 2D-MOT (supplying  $^{40}\text{K}$ ) and by a Zeeman slower (supplying  $^6\text{Li}$  and  $^{23}\text{Na}$ ). As will be explained in more detail in chapter 5, so-called sub-Doppler cooling is then applied to cool the  $^{40}\text{K}$  even further down before evaporative cooling is applied.

Subsequently all atoms will be loaded into a magnetic trap, which is mainly used to place the atoms in front of the high-resolution imaging systems that are inside one of the re-entrant viewports. A first stage of evaporative cooling can then be applied in the magnetic trap, where the  $^{23}\text{Na}$  is evaporated to cool the  $^{40}\text{K}$  and  $^6\text{Li}$ . After that an optical dipole trap in one direction is switched on in addition to the magnetic field, yielding a so-called hybrid trap, where a second stage of evaporative cooling is carried out (see chapter 6 for details).

Finally, the atoms are loaded into the three-dimensional optical lattice, where a special loading procedure ensures that only one layer in this three-dimensional lattice is occupied (this is described in section 7.3). In this way a two-dimensional system of fermions in a lattice is created just in front of the microscope objective and can be imaged with the high-resolution imaging system.

### 4.3 Mechanical layout

The mechanical design of this experiment is centered around the concept of a high-resolution imaging system and magnetic coils inside re-entrant viewports mounted to a main trapping chamber. This resulted in a rather compact design for a triple-species experiment with good optical access.

An CAD illustration of the overall layout is given in figure 4.3. The experiment consists of three different parts: The main trapping chamber (from now on called the **main chamber**) with the re-entrant viewports constitutes the central part of the experiment. To this main chamber, the  $^6\text{Li}$  /  $^{23}\text{Na}$  atom sources are connected with a **Zeeman slower setup** on the right. In the lower left part, a **2D-MOT setup** with the  $^{40}\text{K}$  source is attached to the main chamber.

The central main chamber provides individual optical access for the 3D-MOT beams (red in the CAD illustration) and the optical dipole trap/lattice beams (green), such that these beams do not need to be combined using optical or mechanical elements.

Moreover, a two-layer optical table setup consisting a standard optical table and a second layer made of three custom-made breadboards provides space to place the optical elements that are needed to form the cooling and trapping beams (see details in section 4.4.7).

#### 4.3.1 Imaging system setup

Figure 4.2 shows how the imaging system is set up inside the re-entrant viewports: The atoms are located in a lattice in front of a three-component high-numerical-aperture optical element consisting of the super-polished substrate, the vacuum window itself and a plano-convex lens. The plano-convex lens is optically contacted to the vacuum window on the outside and the super-polished substrate on the inside. In this configuration the vacuum window and the two optical elements act as a perfect hemisphere and enhance the numerical aperture.

The microscope objective is designed in a way such that the optical rays enter the plano-convex lens perpendicular to the surface and therefore one does not need to correct for the glass-air-interface. Figure 7.1 in chapter 7 depicts how the optical rays propagate in this setup. A camera and a lens are located behind the objective at a large distance (shown symbolically in 4.3).

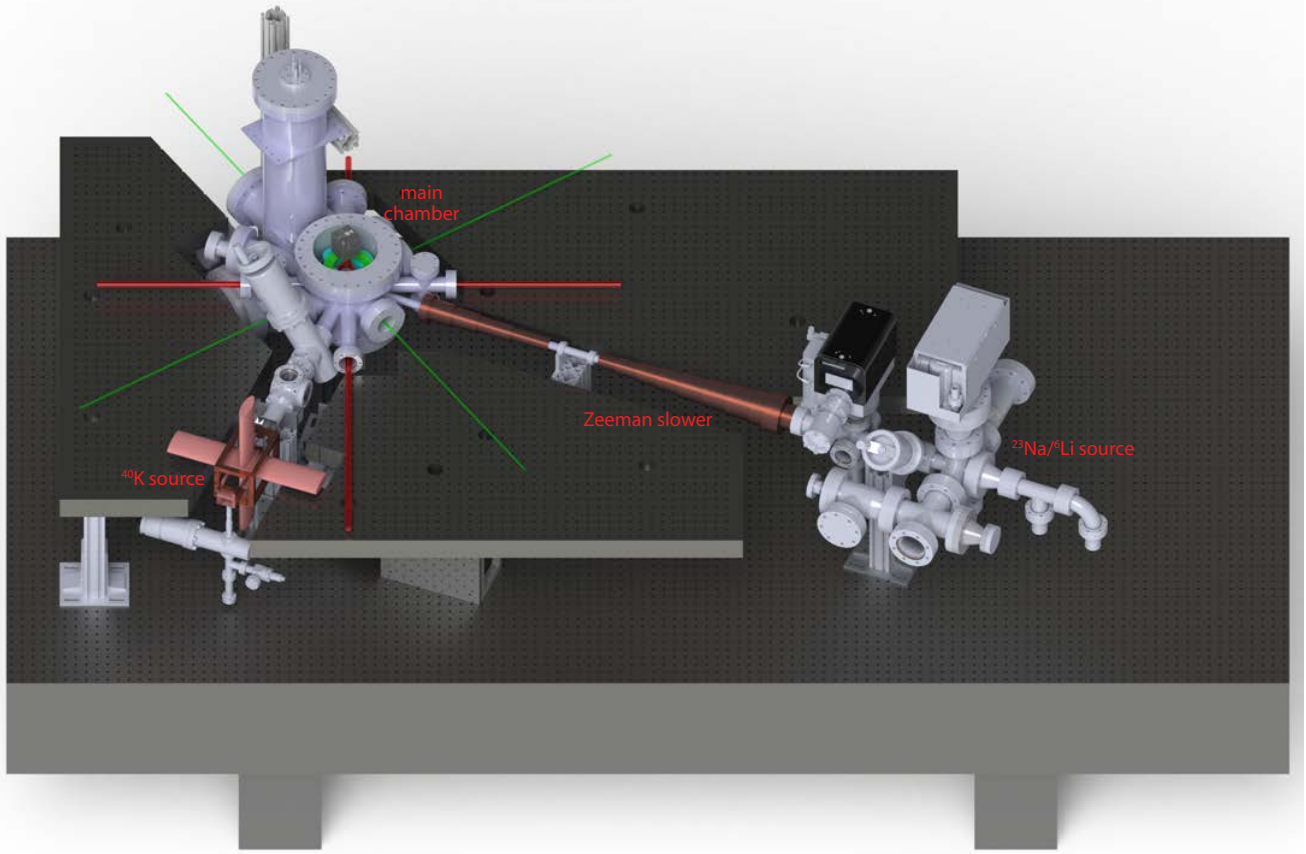


Figure 4.3: The fermi gas microscope from the bird's eye perspective: CAD illustration of the mechanical setup and some of the cooling (red: 3D-MOT) and trapping beams (green: 2D lattice).

#### 4.4 Vacuum system

Ultimately, the desired pressure in the main chamber is less than  $10^{-11}$  mbar in order to ensure a lifetime of the trapped atoms on the order of  $\tau = 100$  s. To achieve such low pressures the whole vacuum system is designed as an ultra-high vacuum system, which means that all major components are made of stainless steel and the connections between different parts is made by a copper gasket connection [88] providing an all-metal connection that does not include any material like polymers or elastomers<sup>4</sup>.

Demanding a very special design, the main chamber was custom-made for this experiment based on a CAD design (drawings can be found in appendix B). Similarly, many other parts were custom-made (e.g. the Zeeman slower vacuum tube, some special six-way crosses in the double

---

<sup>4</sup>The vapor pressure of these materials is very high compared to metals, which causes a lot of 'outgassing' leading to pressure increase.

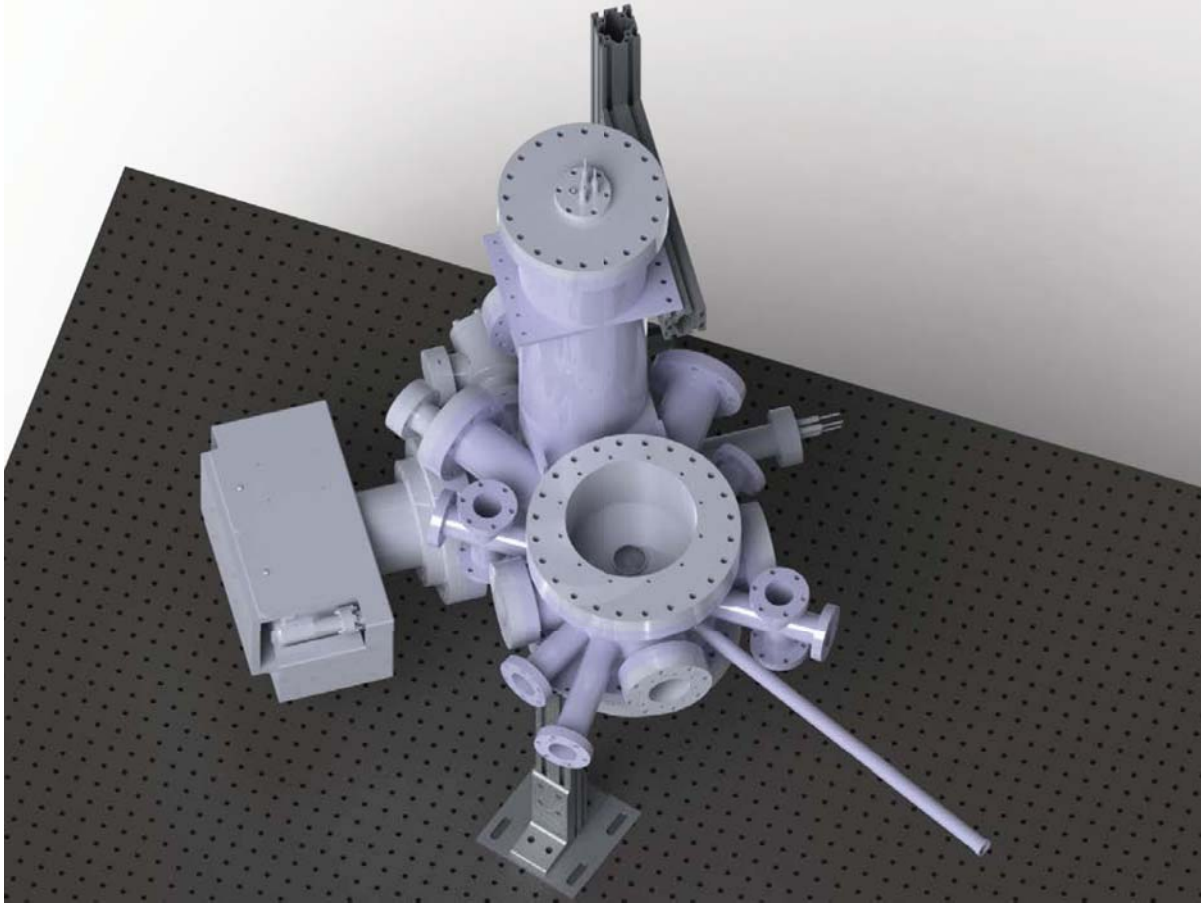


Figure 4.4: CAD illustration of the custom-made main chamber mounted at its final position on top of the optical table.

species oven part, several atomic beam forming elements). The next sections cover the most important details of the design of the vacuum system.

Different types of stainless steel were chosen as the material for the vacuum components: because of the proximity to the atoms, the re-entrant viewports are made out of stainless steel grades compatible to 1.4406<sup>5</sup> (corresponding to the 316LN stainless steel grade of the SAE<sup>6</sup>), which is less magnetic [89] than the standard 1.4301 stainless steel grade. Most of the other components are made out of this most common and hence less expensive stainless steel grade 1.4301 (304 stainless steel grade of the SAE).

#### 4.4.1 Main trapping chamber

A custom-made vacuum chamber was designed to serve as the main vacuum chamber. The custom design allowed to make this main chamber suitable for this experiment, which required to accommodate the microscope setup and the atomic sources for three atomic species (not be possible with an off-the-shelf vacuum chamber). The manufacturing of the vacuum chamber was done by *Sharon Vacuum Inc.*

The pumping concept of this chamber is based on a design for a main chamber described in [90]. As one can see in figure 4.4, a vertical tube with an outer diameter of  $d = 203.2$  mm serves as the main trapping chamber, where the atoms are cooled and trapped. Two re-entrant viewports (see next section) are mounted in the two DN200CF flanges on the top and below of this vertical tube. Several other ports at the side of this tube provide optical access and the input for the 2D-MOT and the Zeeman slower setup (detailed CAD drawings can be found in appendix B).

Another vertical tube with diameter  $d = 152.4$  mm, which is much longer (and therefore commonly referred as the 'chimney'), is connected via a horizontal rectangular tube with a cross section of  $D = 152.4$  mm  $\times$  101.6 mm to the main trapping chamber. It provides pumping with an attached ion pump<sup>7</sup> and two titanium-sublimation-pumps<sup>8</sup>. The large diameter of the connecting horizontal tubes and the proximity to main trapping chamber ensures a large flux towards the pumps and the large diameter of the vertical tubes provides a large surface area that increases the pumping efficiency of the titanium-sublimation pump.

In the horizontal plane two systems of orthogonal axes are important: The rectangular geometry of the optical lattice (green in figure 4.3) is rotated by  $\theta_{\text{rot}} = 34^\circ$  with respect to the geometry of the 3D-MOT beams (red) in the horizontal plane, such that all the laser beams have individual viewports. The 3D-MOT beams have been aligned with the rectangular geometry of the optical table and the main chamber has been positioned on the optical table in way that the complete vacuum system can fit on the table, as can be seen in figure 4.3.

#### 4.4.2 Re-entrant viewports for DN200CF flanges

Re-entrant viewports make it possible to place the magnetic coils and the microscope objective very close to the atoms. It has been a key concept to reduce the electrical current needed for the magnetic coils for a long time and was already used in the first experiments at MIT that created Bose-Einstein condensation [91]. Figure 4.6 shows how this is realized in our experiment for the large viewports, where in one of them the high-resolution imaging system is mounted.

One peculiarity is that the bucket of the re-entrant viewport is not concentric with DN200CF flange, its center line is  $d_{\text{offset}} = 12$  mm apart from the center line of the DN200CF flange. This addresses an issue with the position of the 3D-MOT: The 3D-MOT is created by three pairs of counter-propagating laser beams (and a magnetic quadrupole field). One of the beams would need to pass through the microscope objective and the whole imaging system if the 3D-MOT would be created in front of the microscope. This is not feasible since the imaging system is

---

<sup>5</sup>EN stainless steel grades, normed by the European Committee for Standardization.

<sup>6</sup>Society of Automotive Engineers, common steel grades in the United States.

<sup>7</sup>VacIon Plus 75 StarCell by *Agilent*.

<sup>8</sup>Titanium Sublimation Pump Filament Cartridge by *Agilent*.

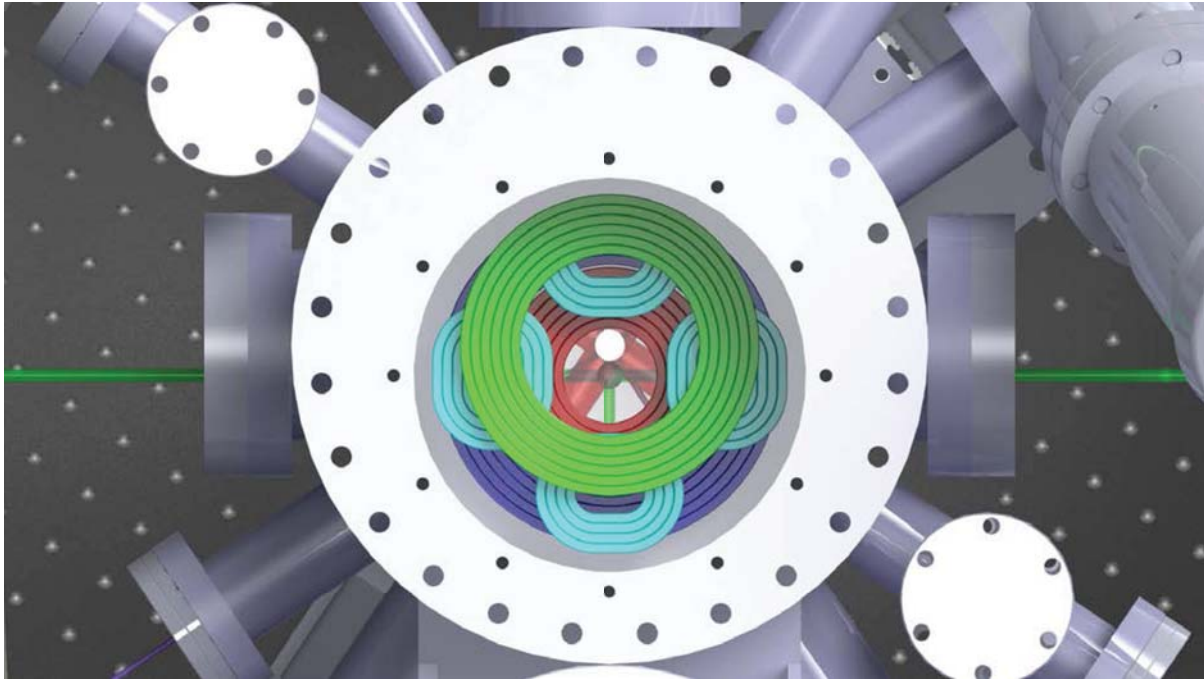


Figure 4.5: View from the top onto the upper re-entrant viewport with the magnetic coils (colored) and the glass window with the hemisphere in it. The 3D-MOT laser beams (red) aim at the center of the main chamber, while the optical dipole trap/lattice beams (green) aim at a position which  $d_{\text{offset}} = 12 \text{ mm}$  apart from the center.

designed to focus at position of the atoms whereas the MOT beams are much larger and are usually almost collimated beams.

A back-reflection of the MOT beam at the vacuum window or at the super-polished substrate is also not possible since the wavelength of the imaging light and the MOT laser light just differ by a few MHz and any high-reflective coating for the 3D-MOT light would block the imaging light completely. As a solution the vertical 3D-MOT beam is back-reflected at a small mirror and a quarter-wave-plate<sup>9</sup> that are placed  $d_{\text{offset}} = 12 \text{ mm}$  apart from the center axis of the imaging system. In figure 4.5 this configuration is shown from the top.

Since the bucket of the re-entrant viewports has been shifted, the 3D-MOT can be created at the center of the trapping chamber (coincident with the center axis of the DN200CF flanges). The atoms then need to be transported to the center of the imaging system, which is done with a magnetic transport (see section 6.2). Based on that concept a sophisticated transport mechanism has been developed to transport the atoms from the original 3D-MOT position in front of the microscope. That is reflected in the fact that as depicted in figure 4.6 the MOT coil (green color

---

<sup>9</sup>The polarization of the MOT light has to be same both beams on the vertical axis. Since reflecting a circular polarization of a mirror would flip the rotation of the electromagnetic field, the circular polarized light is first converted into linear polarized light, then reflected off the mirror and then converted back to circular polarized light by the quarter wave plate.

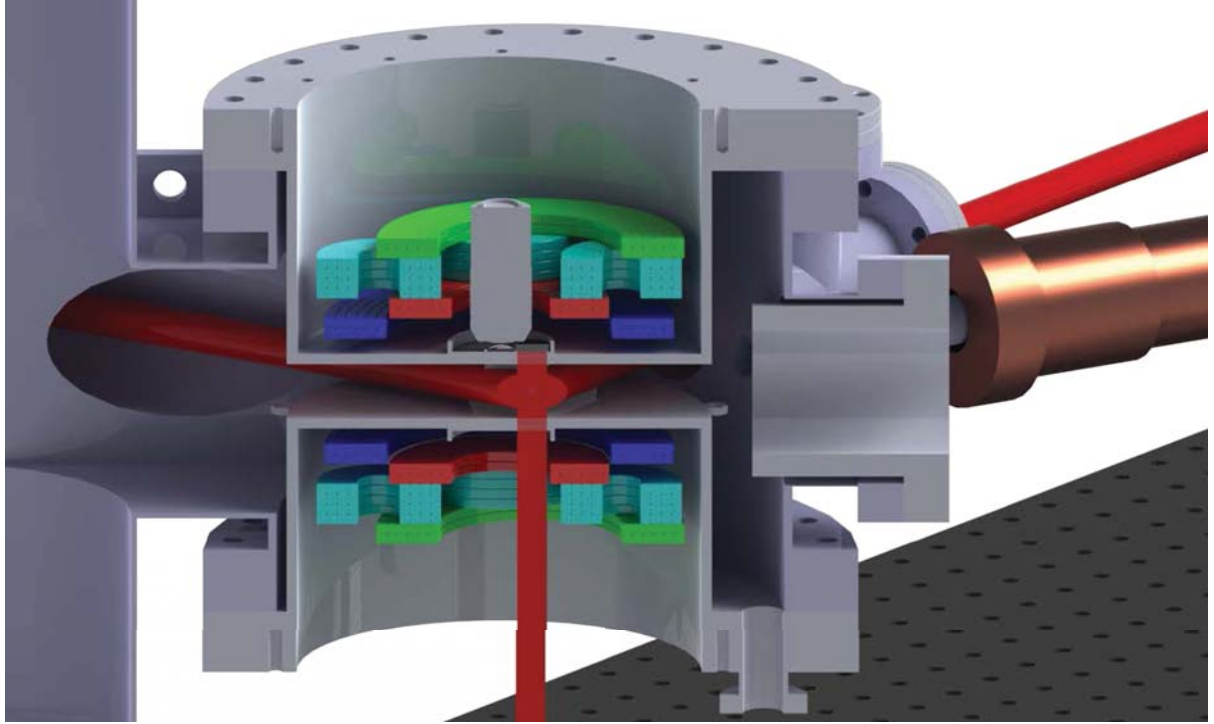


Figure 4.6: CAD illustration showing a cut through the re-entrant viewports mounted to the main chamber. The offset of the centerline of the DN200CF re-entrant viewport with respect to the main chamber vacuum port is visible.

in the figure) is centered around the 3D-MOT position. Chapter 6 describes the setup of the magnetic coils and the transport procedure at length.

The lower viewport is similar to the upper viewport, except that it also contains a little DN16CF port with an electrical feed-through, which connects an RF antenna inside the vacuum (see figure 4.6). Both viewports were manufactured by the *UKAEA Special Techniques Group* at the *Culham Centre for Fusion Energy*, where the windows were bound into the metal mount using laser diffusion bonding [92].

#### Re-entrant viewports for DN63CF flanges

Similar to the larger DN200CF coils, three more re-entrant viewports are manufactured for the DN63CF flanges on the side of the main chamber. Their main purpose is to place lenses and other optical elements very close to the atoms, which can be then used to create the optical dipole trap/lattice beams and also provide the possibility to create an imaging setup close to the trapped atoms in the center of the main chamber, where the distance of the last lens to the atomic cloud is crucial.

#### 4.4.3 Optical viewports

All optical viewports, including the smaller DN63CF re-entrant viewports and the lower DN200CF re-entrant viewport are coated on both sides using ion-beam sputtering<sup>10</sup> to reduce the reflectivity for the wavelengths of the cooling and trapping laser beams.

The coatings were optimized for the wavelengths  $\lambda_1 = 1064$  nm,  $\lambda_2 = 767$  nm,  $\lambda_3 = 671$  nm,  $\lambda_4 = 589$  nm at normal incidence (corresponding to the wavelength of the optical lattice beams and the  $D_2$  transitions frequencies of  $^{40}\text{K}$ ,  $^6\text{Li}$  and  $^{23}\text{Na}$ ).

#### 4.4.4 $^{40}\text{K}$ source

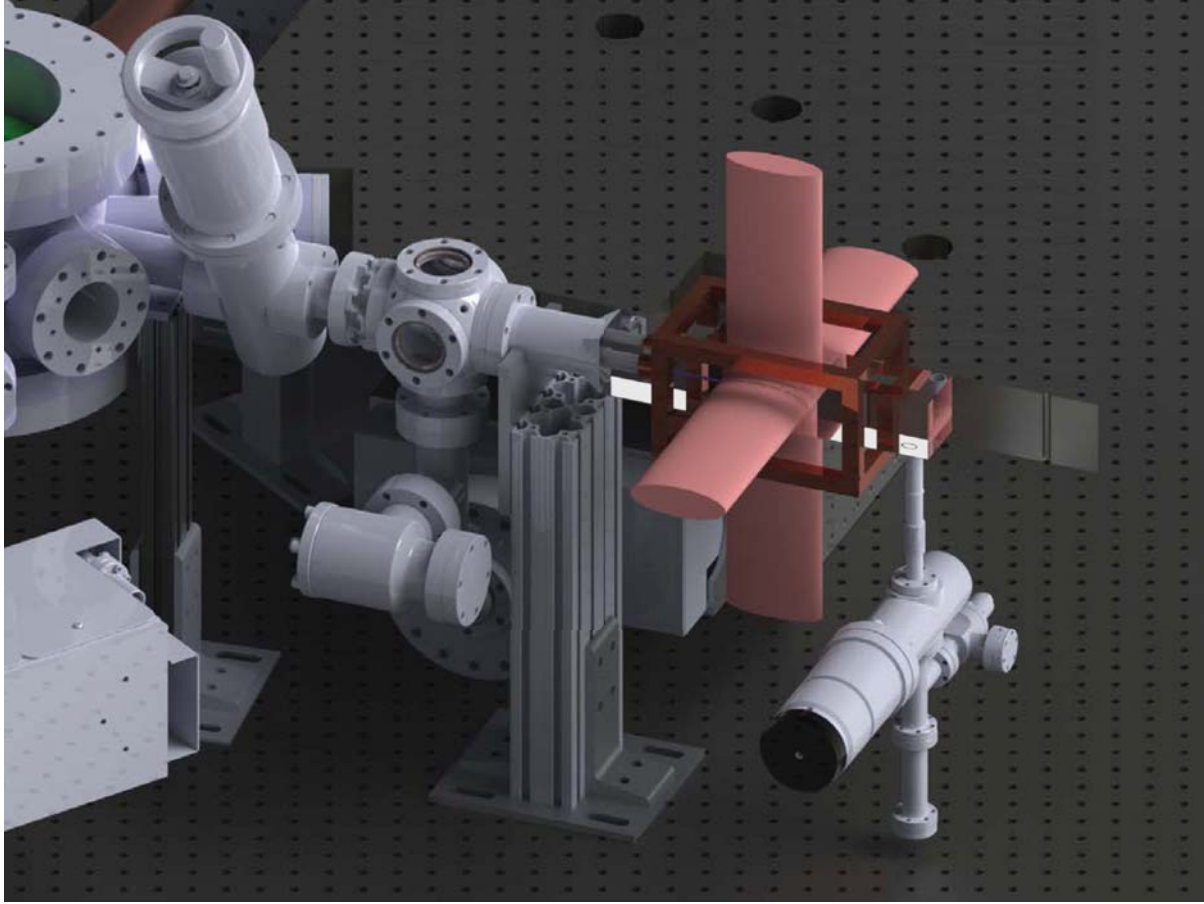


Figure 4.7: CAD illustration showing the 2D-MOT and the atomic source (vacuum nipple below the gate valve on the right side) for  $^{40}\text{K}$ .

Because the natural abundance of  $^{40}\text{K}$  is very low (see table 4.1), an enriched potassium source is used. A 50 mg sample of potassium, where the  $^{40}\text{K}$  was enriched up 7%, was used. The enriched

---

<sup>10</sup>Custom-designed coatings performed by *EvaporatedCoatings Inc.* for the regular viewports and *Laseroptik GmbH* for the re-entrant viewports.

sample was bought in the chemical form of potassium chloride<sup>11</sup> and then chemically converted to elementary potassium and stored under vacuum in a glass ampule to prevent oxidization<sup>12</sup>.

This potassium ampule is placed in metal bellow attached at the lower end of the 2D-MOT glass cell, as can bee seen in figure 4.7 (in the figure the bellow is symbolized as a vacuum nipple). The whole oven is pumped by an ion pump<sup>13</sup> creating an ultrahigh vacuum, therefore this source configuration can be called an effusive oven<sup>14</sup>. An all-metal gate valve<sup>15</sup> separates the bellow from the 2D-MOT glass cell, which allows the change of the potassium ampule when there is no  $^{40}\text{K}$  left. A venting valve is attached to connect a turbomolecular pump for pumping down this part of the vacuum chamber.

By heating the bellow with the ampule with heating tapes<sup>16</sup> to about  $T_{\text{K}} = 80 - 100 \text{ }^{\circ}\text{C}$  a  $^{40}\text{K}$  vapor is created. The effusive flux of  $^{40}\text{K}$  into the glass cell can be increased by heating all metal parts including the gate valve up to the glass cell to a temperature slightly lower than the oven itself, because otherwise the  $^{40}\text{K}$  atoms will most likely stick to the cold metal instead of propagating into the glass cell.

#### 4.4.5 Double species $^6\text{Li}$ and $^{23}\text{Na}$ source

A combined source for  $^{23}\text{Na}$  and  $^6\text{Li}$  was chosen to reduce the space consumption in the experiment. These two species can be combined using the same Zeeman slower and a double-species effusive oven with two separate element reservoirs (originally described in [93]). Compared to the  $^{40}\text{K}$  source, the vapor pressure at  $T = 300 \text{ K}$  is significantly lower for  $^{23}\text{Na}$  and even lower for  $^6\text{Li}$  (see table 4.1), hence the two elements have to be heated to different temperatures.

Figure 4.8 shows how this is implemented here: Two reservoirs made out of standard DN40CF vacuum components have been filled with  $^{23}\text{Na}$  and  $^6\text{Li}$  and attached at the right end of the vacuum chamber and can be heated to different temperatures by applying an external heating.

Nevertheless special components were necessary since the oven part has to be opened about every eight months and the standard CF flanges with copper gaskets are very hard to release and to reseal when heated to high temperatures around  $T = 400 \text{ }^{\circ}\text{C}$ . Instead, the oven components were manufactured out of 1.4401 stainless steel (corresponding to the 316 stainless steel grade of the SAE, a few percent of molybdenum is added in comparison to the 1.4301 (304 SAE) grade), which offers better stability at high temperatures. In addition, nickel gaskets are used because of their better high temperature performance, which is mainly due to the fact that nickel is harder and less sensitive to corrosion. The latter is important when dealing with alkali elements because of their high chemical reactivity. Altogether these components build a stable and easy-to-renew oven.

Two more components are needed to form an atomic beam that can be slowed in a Zeeman slower and then later be trapped in a 3D-MOT in the main trapping chamber. A nozzle (right

---

<sup>11</sup>TraceSciences International.

<sup>12</sup>Technical Glass Inc., now Precision Glassblowing.

<sup>13</sup>75S-DI by Gamma Vacuum.

<sup>14</sup>Effusion is the process of molecular flow through an aperture without collisions between the molecules (atoms).

<sup>15</sup>All-metal gate valve 48124-CE01-0001 by VAT Vacuumvalves AG.

<sup>16</sup>Ultra-High Temperature Heating Tapes by Omega Engineering, Inc.

end of the purple atomic beam in figure 4.8) between the oven and the next chamber (called the oven chamber) provides an small aperture through which the atoms can pass towards the main chamber. This circular aperture has a diameter of  $d = 3.81$  mm and a special conical form on one site (for details see [94]) that is optimized to create an atomic with a small divergence.

In the second stage this expanding atomic beam is shaped even further by adding a so-called cold cup, which is also shown in figure 4.8. This cold cup has another small aperture in the center axis and a shield out of copper that captures all atoms with a large divergence angle. The cold cup is connected via a feed-through to the air-side of the vacuum chamber and can be cooled (hence the name). Especially for alkali atoms it is more likely to stick to a cold surface than to the hot surface (because of the temperature-dependent desorption, see for instance [95]). Typically, these atoms stick to a chamber wall after two to three bounces at wall (depends again on the temperature of the walls). Hence, the cold cup reduces the load on the pumping system and thereby increases the lifetime of the ion pumps.

The same effect has also been used to shield the ion pumps with a so-called baffle, which is a double-side CF-flange component with gills which cause the atoms to stick to the gill surfaces rather than to ion pump elements.

#### 4.4.6 Differential pumping

Both atomic source chambers, even though heated to different temperatures, are typically at a pressure of  $p_{\text{source}} = 10^{-7} - 10^{-8}$  mbar due to the presence of separating small apertures between the two chambers. As quantum gas experiments at ultralow densities require a very good vacuum with an ambient pressure of at least  $p_{\text{main}} = 10^{-11}$  mbar in the main chamber, a differential pumping concept has been employed to maintain this pressure difference.

In the ultra-high vacuum regime the transport properties of molecules can be very well described by the free molecular flow<sup>17</sup>. Then, a tube of length  $l$  and a diameter  $D$ , with a conductivity of  $C \propto \frac{D^2}{l^2}$  can maintain a pressure difference between two neighboring chambers of when one side is pumped at a pumping speed  $S$ .

$$C(P_1 - P_2) = SP_2 \quad (4.1)$$

$$\Rightarrow \frac{P_1}{P_2} \approx \frac{S}{C} \quad (4.2)$$

In our experiment this principle is exploited by putting differential pumping tubes in-between the atomic source chambers and the main chamber to maintain a pressure ratio of up to  $\frac{p_{\text{low}}}{p_{\text{high}}} = 10^{-4}$ . For the  ${}^6\text{Li} / {}^{23}\text{Na}$  side of the experiment two differential pumping tubes of different size and diameter (labeled DPT in figure 4.8) can maintain a pressure ratio of  $R_1^{\text{Li}} = \frac{p_{\text{low}}}{p_{\text{high}}} = 10^{-2}$  and  $R_2^{\text{Li}} = \frac{p_{\text{low}}}{p_{\text{high}}} = 10^{-3}$  at a typical pumping speed of  $S = 70$  L/s.

On the  ${}^{40}\text{K}$  side of the experiments one differential pumping tube (7) in figure 5.1) maintains a pressure difference of up to  $R_2^{\text{K}} = \frac{p_{\text{low}}}{p_{\text{high}}} = 10^{-2}$  and the small aperture in the copper mirror of the 2D-MOT (see section 5.1) provides another factor of  $R_1^{\text{K}} = \frac{p_{\text{low}}}{p_{\text{high}}} = 10^{-1}$ .

---

<sup>17</sup>The fluid dynamics in regime where the mean free path of the molecules/atoms is larger than the size of the chamber is call the free molecular flow. Typically this the regime of high and ultra-high vacuum.

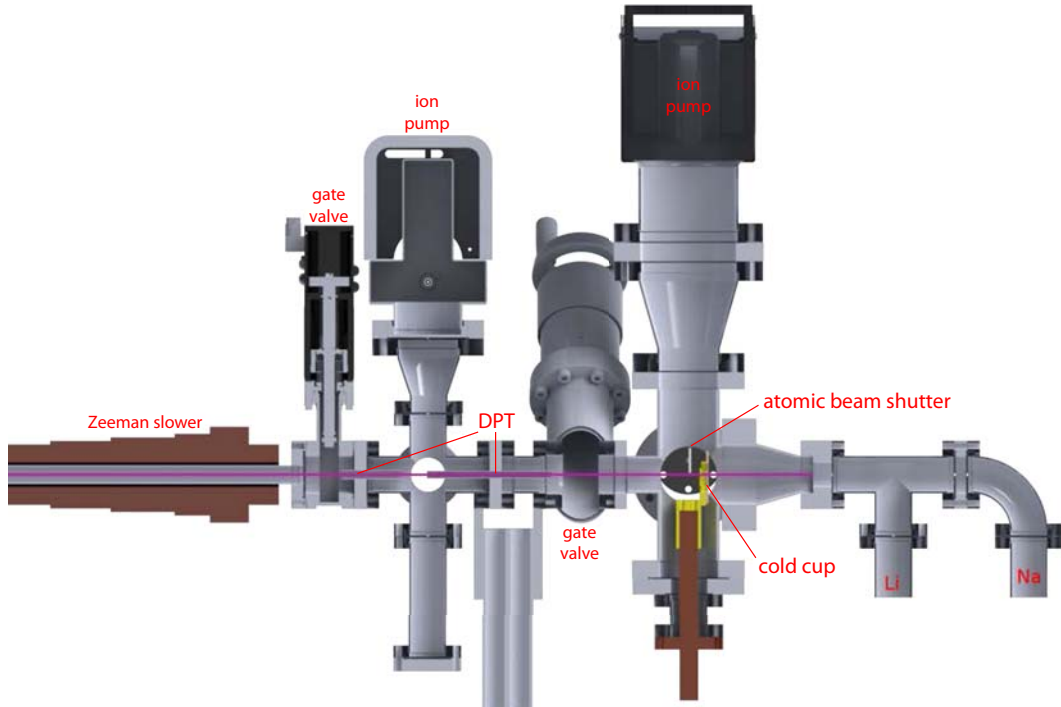


Figure 4.8: CAD illustration showing the double species oven for  ${}^6\text{Li}$  and  ${}^{23}\text{Na}$ : Two reservoirs allow separate temperature control of both atomic sources. An atomic beam (purple) is formed by different beam shaping elements, whereas a cold cup and two ion pumps capture atoms with a velocity vector not in the desired direction of the atomic beam. Two differential pumping tubes (labeled DPT) help maintaining the ultra-high vacuum in the main chamber (attached left of the Zeeman slower), while oven is at higher pressure due to the heating of the atomic sources.

#### 4.4.7 Mounting system and double-layer optical table

After leveling the table the whole vacuum system has been mounted on self-designed mounts made out of t-slotted aluminum extrusion components (often referred as the 80/20 system), where the center of the main chamber and hence the center height of most of the beams is  $h = 14.75$  inches = 374.65 mm above the top of the optical table. The main chamber is fixed with screws in these mounts and custom-made flange support brackets (for instance visible in figure 4.7) are used to support the rest of the vacuum system.

As for a lattice experiment with the goal of a single lattice site resolution a very good mechanical stability for the optical elements is crucial, so to speak second layer optical tabletop is provided by three optical breadboards that have a tapped hole pattern ( $\frac{1}{4}$  inch – 20 screws in a rectangular pattern with a spacing of  $a_x = a_y = 1$  inch = 25.4 mm on both sides). Moreover, their core is made out of a stainless-steel honeycomb structure with thermal expansion coefficients that are very similar to the tabletop.

This second layer is mounted with t-slotted aluminum extrusion mounts<sup>18</sup> such that the upper surface is  $h = 13.05$  inches = 331.47 mm above the optical table. Now, all the optical elements can be mounted using short optical posts. Additionally, the t-slotted aluminum extrusions are filled with lead shot, which reduces the vibrations and improves stability.



(a) Lead-filled mounts for main chamber and breadboards



(b) Double-layer optical table

Figure 4.9: Pictures of the lead-filled mounts for the main chamber (a), which have been made of t-slotted aluminum extrusion, and of the double-layer optical table during the construction of the experiment (b).

#### 4.4.8 Construction and baking

While assembling the vacuum system, the typical guidelines for ultra-high vacuum were followed, described for instance in [96]. Besides the proper handling and cleaning during the assembly, one important step for creating an ultra-high vacuum system is to heat up the entire system to high temperatures (commonly referred as 'baking' the system) while it is being pumped with a turbomolecular pump [97]. At high temperatures (typically up to a couple of hundred degree Celsius) many of the organic and inorganic materials that are present in air (especially water and organic components like methanol) and adsorbed on the chamber walls can be released and pumped off. After cooling down, a lower pressure can be reached.

In this experiment, the three parts of the experiment (main chamber,  ${}^{40}\text{K}$  side with 2D-MOT,  ${}^6\text{Li} / {}^{23}\text{Na}$  side with Zeeman slower) can be disconnected from each other with all-metal<sup>19</sup> gate valves, such that each of the vacuum system parts can be pumped off individually.

---

<sup>18</sup>2040 series aluminum extrusion and a floor base plate by *80/20 Inc.*

<sup>19</sup>All-metal valves have a higher temperature rating since they do not use a polymer or elastomer as a sealant and are therefore better suitable when the system is exposed to high temperatures. Furthermore, outgassing and corrosion is reduced.

The main chamber was heated up in two runs, one run with metal blanks covering all ports up to  $T_{\text{bake}}^1 = 350$  °C and in a second step with the optical viewports up to  $T_{\text{bake}}^2 = 200$  °C since the glass windows of the viewports have a lower temperature rating. The two other parts were only heated up to  $T_{\text{bake}}^1 = 220$  °C since the glass cell in the 2D-MOT chamber and many parts at the  ${}^6\text{Li} / {}^{23}\text{Na}$  side cannot be heated up higher because of their temperature ratings.

## 4.5 Experiment control

Data acquisition and control of the experiment is realized with a computer system consisting of two computers and different computer interface cards. The first computer provides digital (logic, 0 V or 5 V) and analog outputs (continuous, 0 – 15 V tunable with 16 bit precision) by using the National Instruments data acquisition cards. They provide a very fast timing (most of the interface cards up to 20 MHz timing resolution and up to 2 MS/s update rate).

A variable timebase setup based on a FPGA<sup>20</sup> in combination with a software that was written to fit the needs of an ultracold atom experiment [98] allows a very sophisticated computer control system to setup the experimental run sequences.

---

<sup>20</sup>XEM3001v2 by *Opal Kelly*.

---

## 5. Laser cooling

---

Several experimental concepts have been developed based on laser cooling [54], which provide not only mechanisms to cool but also to trap neutral atoms in a magneto-optical trap [55]. Most of the techniques are part of the standard toolkit in an ultracold atom laboratory, therefore the concepts are discussed just briefly and more emphasis is put on the implementation in our specific setup. For a detailed discussion of the underlying physical phenomena the reader is referred to reference [99].

Based on experiences in other previous experiments at MIT it was decided to implement a 2D-MOT for  $^{40}\text{K}$  and a double-species Zeeman slower for  $^6\text{Li}$  and  $^{23}\text{Na}$  in order to capture atoms from an effusive oven sources and cool them down to temperatures suitable for capturing them in a triple-species 3D-MOT. After the atoms have been cooled and captured in the 3D-MOT, the lowest achievable temperature is given by the Doppler limit<sup>1</sup>. For potassium sub-Doppler cooling will be implemented opening up the possibility to cool the atoms in the 3D-MOT below the Doppler temperature, theoretically down to the recoil limit<sup>2</sup>.

In the following sections it is described how these different laser cooling techniques are implemented in this quantum gas experiment.

### 5.1 2D-MOT for $^{40}\text{K}$

Some experiments with cold atoms and especially with  $^{40}\text{K}$  employ a 2D-MOT [101] instead of a Zeeman slower, which is used by the majority of the ultracold atom experiments with alkali atoms.

The main advantage is that the material consumption is much lower compared to a Zeeman slower. Although Zeeman slowers can offer much higher atom fluxes in general, a 2D-MOT yields high fluxes from much smaller atomic samples with a much higher efficiency. This is key for trapping of  $^{40}\text{K}$  since its natural abundance is 0.0117(1)% [82] and the prices for artificially enriched potassium are very high<sup>3</sup>.

Other advantages include the typically less space-consuming design of a 2D-MOT as well as the smaller residual magnetic fields of the 2D-MOT observed at the center of the main trapping

---

<sup>1</sup>The Doppler temperature limit is proportional to the linewidth of the transition used in the laser cooling process,  $k_B T_{\text{Doppler}} = \frac{\hbar\Gamma}{2}$ , and has its origin in the random character of the spontaneous emission process (for details see for instance [100] and [99]).

<sup>2</sup>The recoil temperature limit arises from the fact that any type of laser cooling is limited by the amount of energy that one photon can take away from the atom in an one-photon process. The fundamental limit is hence given by the recoil energy associated with one photon,  $k_B T_{\text{recoil}} = \frac{\hbar^2}{2m\lambda^2}$ .

<sup>3</sup>TraceSciences International quoted 100 mg of 10% enriched  $^{40}\text{K}$  for 12 k\\$ (in the form of potassium chloride, KCl).

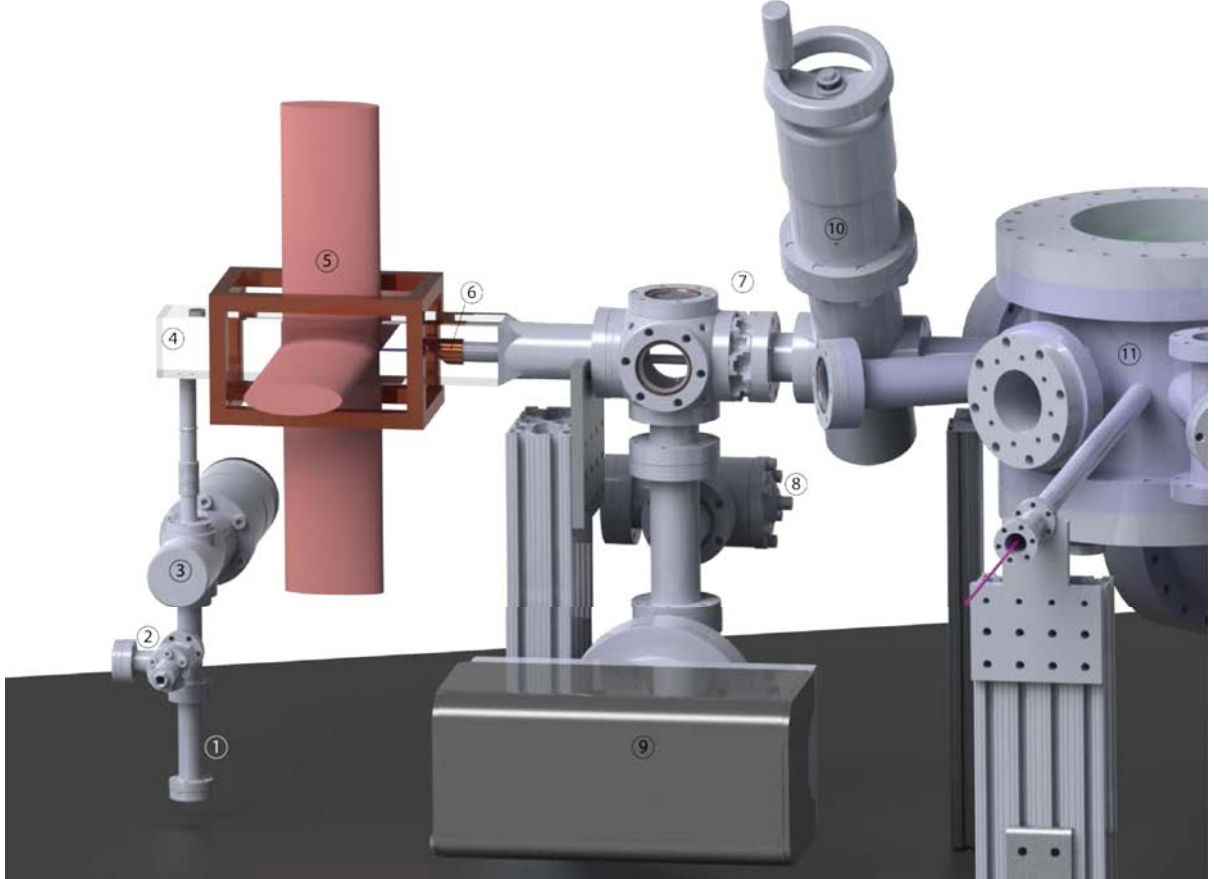


Figure 5.1: CAD illustration of the 2D-MOT part of the experiment, described in the text.

chamber <sup>4</sup>.

In general, a 2D-MOT is a setup of two magneto-optical traps (MOTs) along two orthogonal axes that capture atoms from an atomic vapor and form an atomic beam along the third axes. Usually a 3D-MOT in a neighboring vacuum chamber is directly loaded from this atomic beam (a detailed explanation might be found for instance in [102]).

This concept can be enhanced by applying a pair of optical molasses beams along the direction of the atomic beam, often referred as 2D<sup>+</sup>-MOT. If the intensity of these laser beams is imbalanced such that the intensity of the beam propagating towards the main trapping chamber is higher, the atom flux into the 3D-MOT can be enhanced. This is due to the fact that in average an atom absorbs more photons with a momentum towards the main chamber because of the imbalanced light intensity. These beams are usually named the pushing and the retarding beam.

---

<sup>4</sup>A Zeeman slower typically uses large magnetic fields, whereas a 2D-MOT uses magnetic field gradients, which

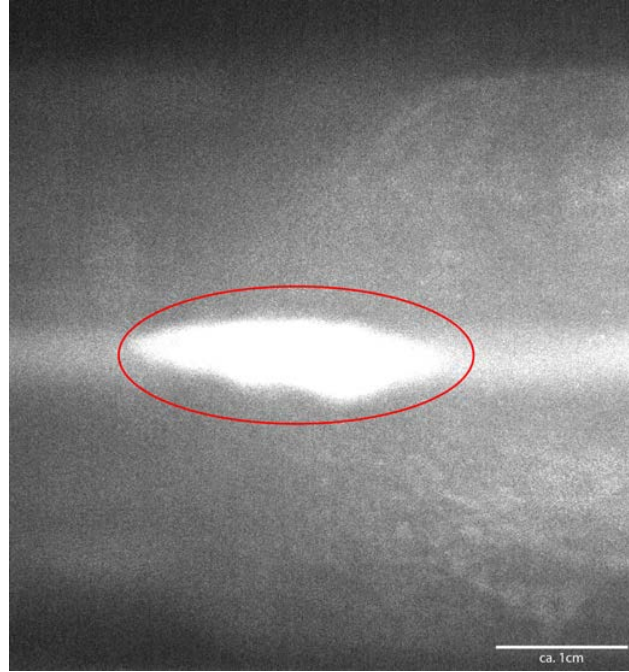


Figure 5.2: Fluorescence image of the 2D-MOT showing a large cloud of laser-cooled  $^{39}\text{K}$  atoms.

A 2D<sup>+</sup>-MOT of  $^{40}\text{K}$  is realized in this experiment, since our main goal is to load fermionic  $^{40}\text{K}$  into an optical lattice. However the same setup could be used to trap the other two naturally occurring isotopes of potassium  $^{39}\text{K}$  and  $^{41}\text{K}$  with the same setup by slightly adjusting the frequencies in the laser system. For initial alignment purposes the laser system is prepared to work with  $^{39}\text{K}$  as well, since it has a much higher natural abundance of 93.2581(44)% [82] (about 19 times more than our enriched samples) and hence simplifies the initial set-up of the 2D-MOT laser beams. Furthermore, the option of a 2D<sup>+</sup>-MOT of  $^{41}\text{K}$  leaves the possibility to sympathetically cool  $^{40}\text{K}$  with  $^{41}\text{K}$ <sup>5</sup> [104].

Figure 5.1 illustrates the 2D-MOT in this experiment (the additional molasses beams of the 2D<sup>+</sup>-MOT are not shown for clarity): A sample of 50 mg of  $^{40}\text{K}$  atoms (enriched to 5% abundance) is heated ①, then the atoms diffuse into a glass cell ④. Here, the 2D-MOT laser beams ⑤ capture the atoms and form an atomic beam that passes through a hole in a copper mirror ⑥. This mirror can be used to create the additional optical molasses beams along the longitudinal direction for the 2D<sup>+</sup>-MOT configuration.

After passing the hole of this copper mirror the atoms propagate into the intermediate chamber

vanish in the center of the trap.

<sup>5</sup>Sympathetic cooling of  $^{40}\text{K}$  with  $^{39}\text{K}$  is not favorable since the interspecies s-wave scattering length is very small,  $a_s^{^{39}\text{K}-^{40}\text{K}} = -2.84(10)a_0$  [103]. For sympathetic cooling of  $^{40}\text{K}$  with  $^{41}\text{K}$  the scattering length of  $a_s^{^{40}\text{K}-^{41}\text{K}} = -54.28(21)a_0$  [103] is sufficient for thermalization of both species.

that is separated from the main chamber by a differential pumping tube<sup>6</sup> (7) and an all-metal gate valve (10)<sup>7</sup>. Since the diameter of the hole in the copper mirror is small ( $d = 2 \text{ mm}$ ), it also acts as a differential pumping tube.

The 2D-MOT has brought into operation for the two major potassium species,  $^{40}\text{K}$  and  $^{39}\text{K}$ . Figure 5.2 shows a fluorescence picture taken with the laser frequencies tuned for  $^{39}\text{K}$ . The 2D-MOT for  $^{40}\text{K}$  can be also seen on the camera, but is much weaker due to the lower abundance.

## 5.2 Zeeman slower for $^6\text{Li}$ and $^{23}\text{Na}$

Zeeman slowers [106] have been the workhorses to cool atoms from the hot temperatures of an effusive oven serving as the atomic source down to temperatures lower than the maximal capture temperature of a MOT.

Our setup of the experiment (see section 4.3) features a double-species Zeeman slower for  $^6\text{Li}$  and  $^{23}\text{Na}$ . Originally developed as an idea to upgrade a cold-atom experiment for  $^{23}\text{Na}$  to a double-species experiment for  $^6\text{Li}$  and  $^{23}\text{Na}$  [94], it turned out to be a very useful concept that reduces the complexity and the space consumption in the experiment significantly.

Like the name suggests, a Zeeman slower exploits the Zeeman effect to slow and cool atoms. A laser beam counter-propagating to the direction of the atoms is tuned to one of transitions from the electronic ground state  $^2\text{S}_{\frac{1}{2}}$  to the excited state  $^2\text{P}_{\frac{3}{2}}$ . A spatially varying magnetic field compensates for the Doppler shift of the atoms: At the beginning the atoms are very hot (typically with a velocity of  $v = 1000 \text{ m/s}$ ) and have a large Doppler shift because of the high velocity in the direction of the laser beam. As the laser beams cool the atoms, the atoms slow down and the Doppler effect is smaller, but is compensated by a smaller Zeeman effect in the Zeeman slower.

Hence, a Zeeman slower is essentially a long coil with spatially varying current density and a laser beam resonant at an atomic transition.

A Zeeman slower for  $^6\text{Li}$  and  $^{23}\text{Na}$  is favorable because the atomic sources have to be run at very high temperatures due to their low vapor pressure and a Zeeman slower reaches higher fluxes for high-temperature effusive ovens. One important point is that one can tune the upper limit of the velocity that is being slowed by the Zeeman slower, which can be then comfortably set to mean velocity of the oven temperature. For a 2D-MOT the maximal capture velocity cannot be tuned.

In our setup a so-called spin-flip Zeeman slower design is used, described for instance in [90]. In this design the magnetic field is not ramped from a high positive value (can be up to  $B_{\text{Zeeman}} = 10^{-2}\text{T}$ ) to zero but instead from a positive value to zero magnetic field in the first section (referred as the decreasing field section) and then to negative value in a second section (decreasing field section). The total difference between the magnetic field at the beginning and at the end of the

---

<sup>6</sup>A differential pumping tube in the UHV regime is a small aperture (typical a few millimeters in diameter) which helps to maintain a pressure difference between two parts of a vacuum chamber [105]. In this case the pressure difference of the oven side and the main chamber can be up to a factor of 100 at each differential pumping tube.

<sup>7</sup>All-metal gate valve 48124-CE01-0001 by VAT VacuumValves AG.

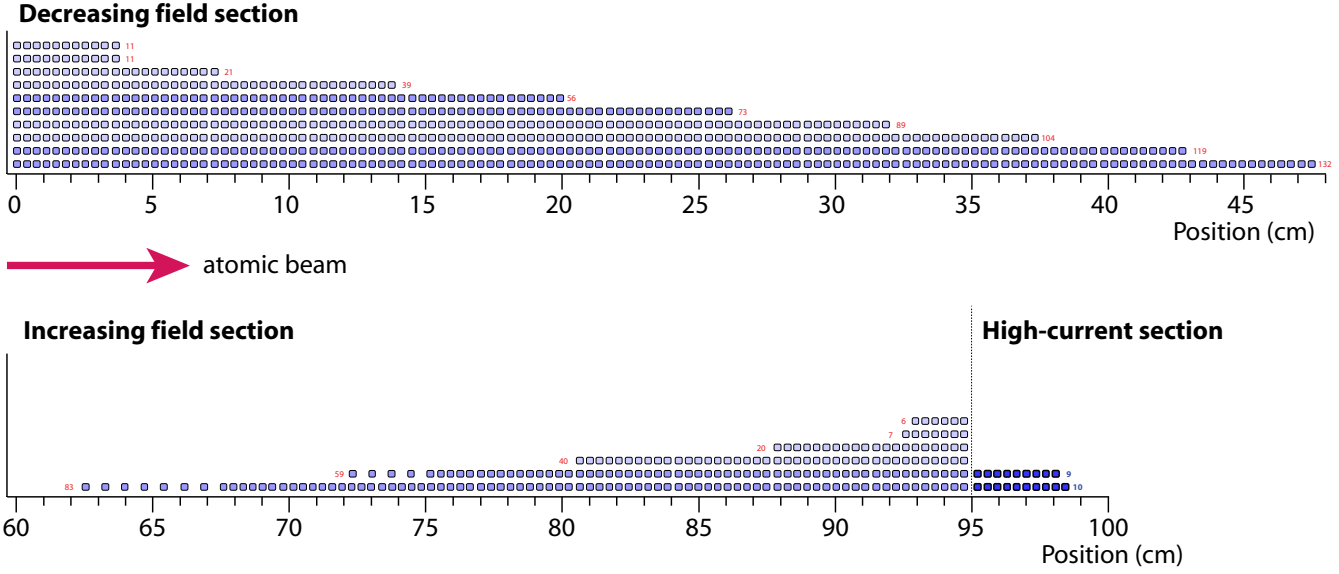


Figure 5.3: Zeeman slower winding profile showing the number of turns in each layer. The increasing field section is attached right of the decreasing field section as the continuing position scale indicates. The different colors symbolize cooling circuits, all turns of a specific color have one common water cooling connection.

slower is the same, but for the second variant the maximal current density is lower and smaller power supplies can be used. Figure 5.3 shows schematically a profile of the spin-flip Zeeman slower developed for this experiment.

Another important detail is that the last part of the increasing field section, which is very close to the 3D-MOT in the main chamber, has been split to separate the electric circuit supplying the last few centimeters: By running a higher current through a smaller number of loops, the resulting magnetic field is the same, but less unwanted stray fields are expected inside the main chamber since the coil has now a smaller diameter. Furthermore, it can be located closer to main vacuum chamber and hence closer to the center of the atoms because of the smaller size.

In total there are three different sections of the Zeeman slower, which are shown in figure 5.3. The first two sections (decreasing and increasing field section) are switched by a MOSFET (see MOSFET box design in appendix E.2) and the last high-current section is switched by an IGBT (see IGBT box design in appendix E.1).

Figure 5.3 shows the exact setup with the number of turns in each layer. The different color shades denote cooling circuits where all turns of one color have a common water connection.

The spatial dependence of the magnetic field has been measured with a magnetic field measurement device<sup>8</sup>, which is shown in figure 5.4 together with a numerical simulation.

<sup>8</sup>Three-Axis Hall effect Gaussmeter by FW Bell Inc.

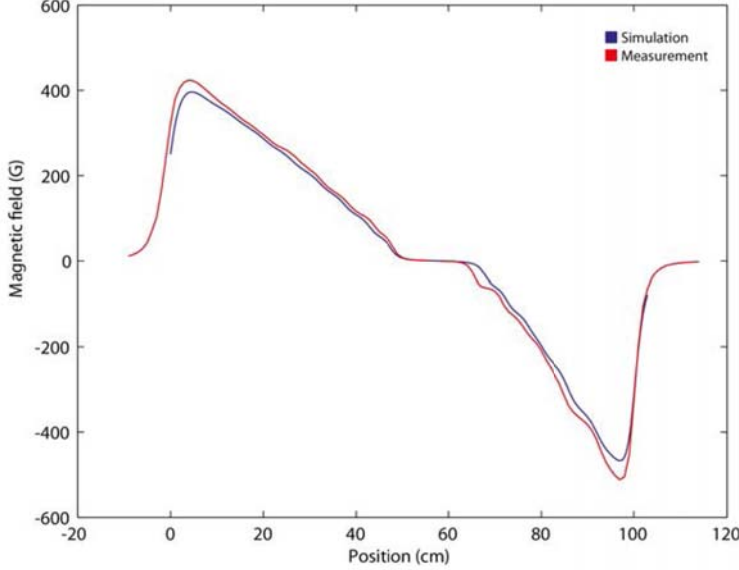


Figure 5.4: Simulated and measured longitudinal magnetic field of the Zeeman slower.

### 5.3 Laser systems

#### 5.3.1 Laser system for $^{40}\text{K}$

Two different laser frequencies are needed to create a MOT, the actual laser *cooling* transition and the so-called *repumper* transition. As can be seen in figure 4.1 in chapter 4, the hyperfine structure of potassium is inverted and the upper  $^2\text{P}_{\frac{3}{2}}$  state splits up into four different hyperfine levels which are spaced by only a few MHz. Therefore it can happen that an atom escapes from the cycling cooling transition and ends up in the lower  $F = \frac{7}{2}$  state, where it can not be cooled any more. The repumper 'pumps' it back to the upper  $F' = \frac{9}{2}$  state, from where it can decay again to the lower  $F = \frac{9}{2}$  state and can be cooled again. These two laser frequencies are created using diode lasers<sup>9</sup>. Figure 5.5 gives an schematic overview of the setup.

To stabilize the frequency of those lasers, a *master laser* in an external cavity setup with tunable grating (similar to [108]) is locked to the D<sub>2</sub> absorption line of  $^{39}\text{K}$  in a vapor cell. Using acousto-optic modulators the frequency of the light of the master laser is shifted to its desired value (see figure 4.1) and then fed into the diode lasers (injection-lock). Tapered-amplifiers<sup>10</sup> are then used to amplify the laser light.

In order to provide a conceptual picture of the laser system, several details of the laser system are neglected. The reader might refer to the Bachelor thesis of Vinay Ramasesh [40] that describes

<sup>9</sup>Home-made diode laser employing laser diodes EYP-RWE-0790-04000-0750-SOT01-0000 from *eagleyard Photonics*.

<sup>10</sup>A home-made mount design for the 2W tapered amplifier EYP-TPA-0765-02000-4006-CMT04-0000 from *eagleyard Photonics*.

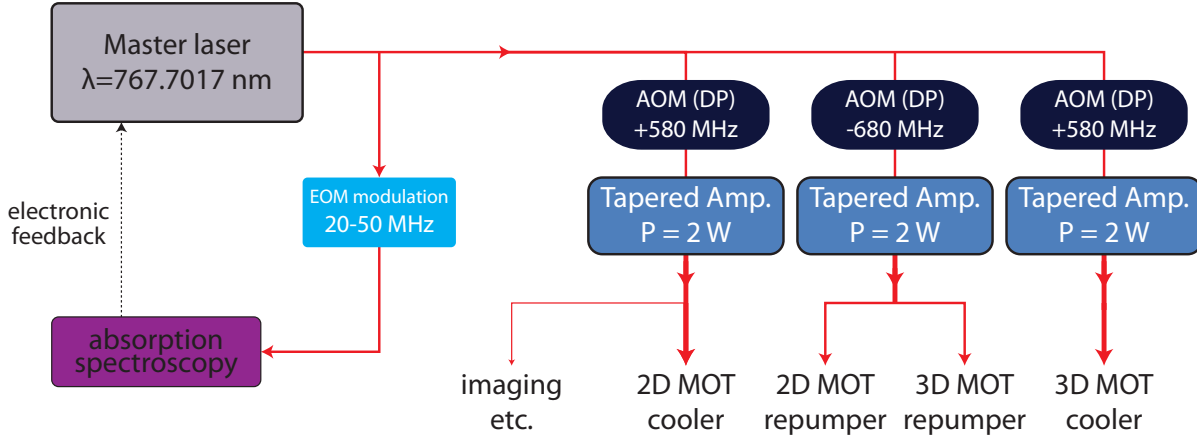


Figure 5.5: Schematic diagram of the laser setup used for the 2D and 3D-MOT for  $^{40}\text{K}$ . AOM (DP) denotes an acousto-optic modulator in a double-pass configuration [107], the given laser frequency shift denotes the shift after the complete passage of the double-pass configuration.

the lasers systems for  $^{40}\text{K}$  and  $^6\text{Li}$  of this experiment at length. Furthermore, references [102] and [109] describe laser systems for magneto-optical traps that are very similar to the  $^{40}\text{K}$  and  $^6\text{Li}$  laser system of this experiment.

### 5.3.2 Laser system for $^6\text{Li}$

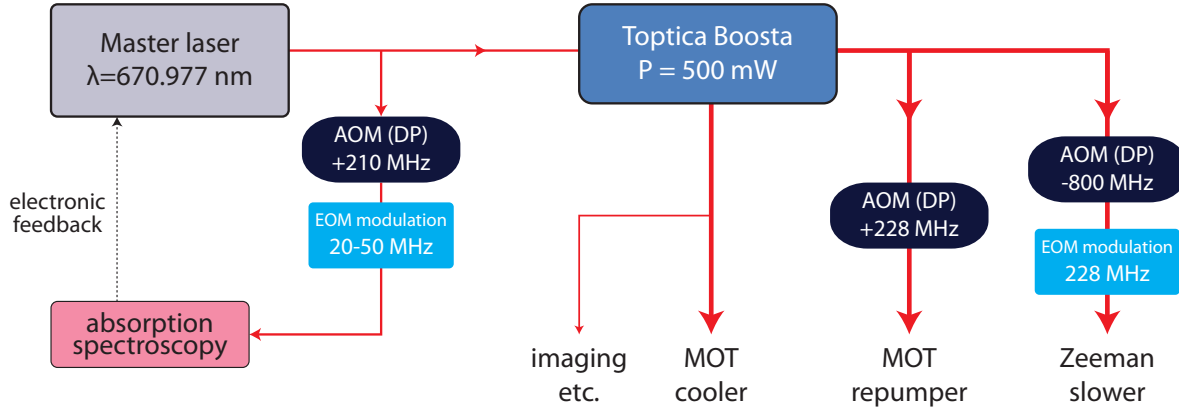


Figure 5.6: Schematic diagram of the laser setup supplying light for the Zeeman slower and 3D-MOT for  $^6\text{Li}$ .

A very similar approach has been pursued for the creation of the needed laser frequency for the laser cooling of  $^6\text{Li}$ . Figure 5.6 shows again a simplified, conceptual picture. In contrast to the

$^{40}\text{K}$  system, only one tapered amplifier has been used to amplify the laser light before it is being shifted with the acousto-optic modulators. Like for  $^{40}\text{K}$ , several details have been omitted and the reader might refer to the same references as given in the previous section.

### 5.3.3 Laser system for $^{23}\text{Na}$

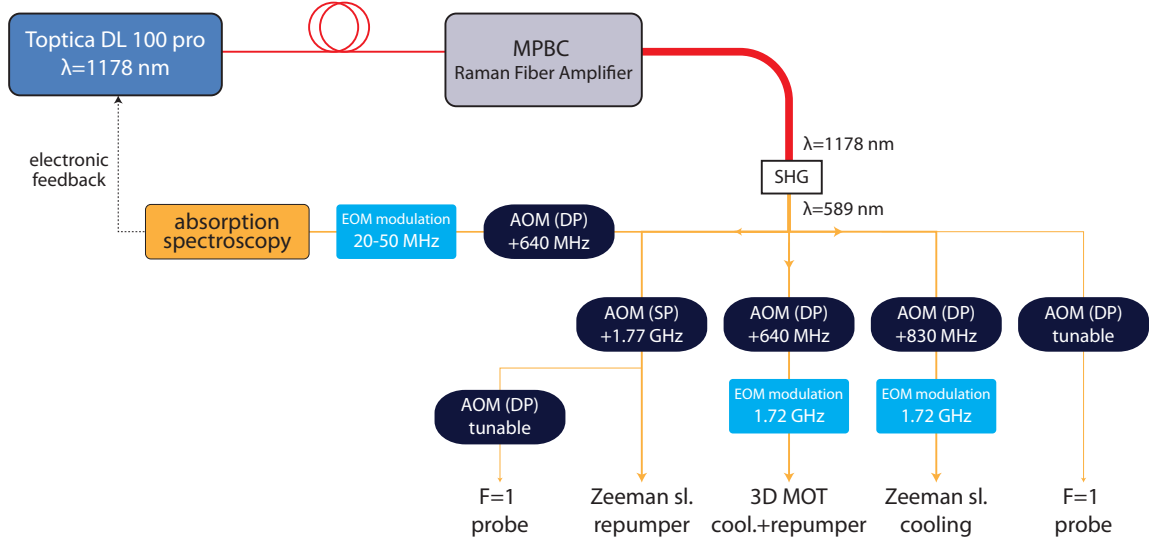


Figure 5.7: Schematic diagram of the planned laser setup for  $^{23}\text{Na}$ .

The laser setup for  $^{23}\text{Na}$  of this experiment is based on a Raman fiber amplifier system which is seeded by a Toptica DL 100 pro design laser system with a center wavelength of  $\lambda_{\text{seed}} = 1178 \text{ nm}$ . In the Raman amplification fiber the seed light is amplified in an optical Raman scattering process by the pump light of three pump laser diodes. After the amplification of the light at the seed-wavelength it passes through a second-harmonic generator crystal that doubles the frequency of the light yielding a wavelength of  $\lambda_{\text{Na}} = 589 \text{ nm}$ . This is schematically shown in figure 5.7 together with the intended configurations of the acousto-optic und electro-optic modulators to provide the needed frequencies and imaging transitions.

## 5.4 Triples-species 3D-MOT

In this triple species experiment all three atomic species need to be cooled and trapped at almost the same position close to the center of the main vacuum chamber. Although the complexity increases with the number of different atomic species, the ingredients of the systems are conventional laser cooling techniques and challenges arise especially in the technical design of the experiment. Since it is known that double species MOTs for  $^6\text{Li}$ - $^{23}\text{Na}$  and  $^{23}\text{Na}$ - $^{40}\text{K}$  mixtures are easily possible [104], a possible triple-species MOT is one important part of the design of this experiment. In particular this work tries to include the option for all three atomic species from the beginning based on the experiences in the other experiments of the given reference. This will

hopefully lead to a more robust and elegant experimental design, which will later be useful in the day-to-day operation of the experiment.

For a multi-species MOT the collisional properties are important since collisions might lead to atom losses. It is known that a triple-species 3D-MOT for  $^{23}\text{Na}$ ,  $^6\text{Li}$  and  $^{40}\text{K}$  is possible. The combination  $^6\text{Li}$  -  $^{23}\text{Na}$  has been used for many years and the  $^{23}\text{Na}$  -  $^{40}\text{K}$  mixtures were created in the last years. For the latter combination not all scattering properties are precisely known, but more and more data is becoming available [81]. The interspecies scattering length for  $^{40}\text{K}$  -  $^{23}\text{Na}$  is negative and likely to be on the order of a couple of hundred Bohr-radii and hence double-species MOTs of  $^{40}\text{K}$  -  $^{23}\text{Na}$  are known to work.

In this setup the 3D-MOT for all three species is created by spatially overlapping all three MOT beams including their respective repumper frequencies. In the end that means that six different light frequencies have to be overlapped. A compatibility option for sympathetic cooling with  $^{41}\text{K}$  is included, so up in principle up to eight different light frequencies need to be joined. This is done stepwise.

First, two fiber-manifolds providing a junction of polarization-maintaining (PM) fibers join the MOT cooling and the repumping light for  $^6\text{Li}$  and  $^{40}\text{K}$  (the latter one has the mentioned option for  $^{41}\text{K}$ ) because for  $^6\text{Li}$  and  $^{40}\text{K}$  a lot of repumper light power is needed (up to equal power of the MOT cooler transition in case of  $^6\text{Li}$ ). These fiber manifolds<sup>11</sup> have 2 inputs and 4 outputs for  $^6\text{Li}$  and 4 inputs and 4 outputs for  $^{40}\text{K}$  /  $^{41}\text{K}$ . From these four outputs three outputs will be used for the three different axes, while the beams are retro-reflected after passing through the main chamber.

In contrast, for  $^{23}\text{Na}$  repumping light from just one direction is enough. By using the principle of a *dark-spot* MOT [110] two issues of a conventional MOT for  $^{23}\text{Na}$  (sometimes called a *bright MOT*) can be circumvented: Trap loss can occur in the high densities of the trap center due to scattering of the excited  $3^2\text{P}_{\frac{3}{2}}$  states with the lower  $3^2\text{S}_{\frac{1}{2}}$  states [111] and because of re-absorption of the spontaneously emitted photons by another atom [112].

In a dark-spot MOT the repumper beam is modified with a dark spot on a piece of glass such that the repumper light does not hit the trap center but just illuminates a cone around the trap center. This way the atoms in the trap center end up the  $F = 1$  state which is dark to the cooling transition and both effects of the bright MOT are prevented. Therefore for sodium no fiber manifold but instead just two conventional fibers are used, which split up the light on the experiment table. In one direction the repumping light is mixed into the cooling light using polarizing beam splitters.

In a second step the light of the lithium and the potassium fiber manifold is combined using polarizing beam splitters<sup>12</sup> and then joined with the sodium light using a dichroic mirror<sup>13</sup> as shown in figure 5.4. The polarization of the resulting beam is tuned by using a zero-order  $\frac{\lambda}{4}$ -waveplate optimized for the wavelengths  $\lambda_1 = 671 \text{ nm}$  and  $\lambda_2 = 767 \text{ nm}$ <sup>14</sup>.

---

<sup>11</sup>Custom-made by *Evanescence Optics Inc.*

<sup>12</sup>Custom-made broadband polarizing beam splitters by *Redoptronics*.

<sup>13</sup>Custom-made dichroic mirror by *CVI Melles Griot*.

<sup>14</sup>Custom-made by *CVI Melles-Griot*.

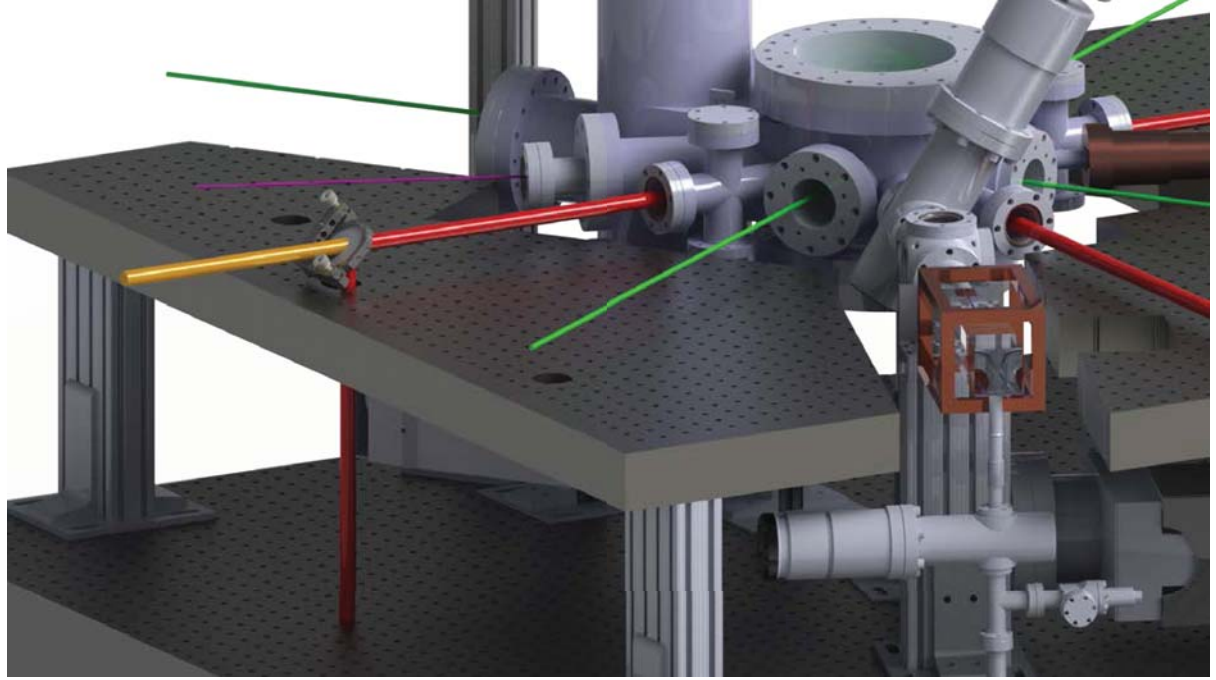


Figure 5.8: CAD illustration of one arrangement of the 3D-MOT beams: The beam tuned to the  $^{23}\text{Na}$  frequency (yellow) is joined at a dichroic mirror with the beam carrying the frequencies for  $^6\text{Li}$  and  $^{40}\text{K}$  (red). The two frequencies for  $^6\text{Li}$  and  $^{40}\text{K}$  are created below the upper layer of the optical table (not shown in detail).

At the time of writing the 3D-MOT has been successfully brought to operation for  $^{39}\text{K}$  and  $^{40}\text{K}$ . Figures 5.9a and 5.9b show the first fluorescence images of the 3D-MOT for  $^{39}\text{K}$  and  $^{40}\text{K}$ , respectively.

## 5.5 Sub-Doppler cooling of $^{40}\text{K}$

For fermionic atoms evaporative cooling is not as easy as for bosonic atoms since the Pauli principle prevents collisions and hence thermalization of equal spin states. Common solutions are to cool two different spin states by simultaneous evaporation or by sympathetically cooling with a bosonic atom that is being evaporated. Both concepts have been applied successfully in other experiments and will be implemented in our machine as well.

Nevertheless it is desirable to make use of laser cooling techniques that cool below the Doppler temperature, because it decreases the evaporation time dramatically while reducing atom losses during evaporation. Furthermore, a laser cooling mechanism is needed to constantly cool the atoms to the lowest energy state on a single lattice site while imaging them with the high-resolution imaging system because typically a couple of hundred photons are needed to image single atoms on single lattice site (described in chapter 7).

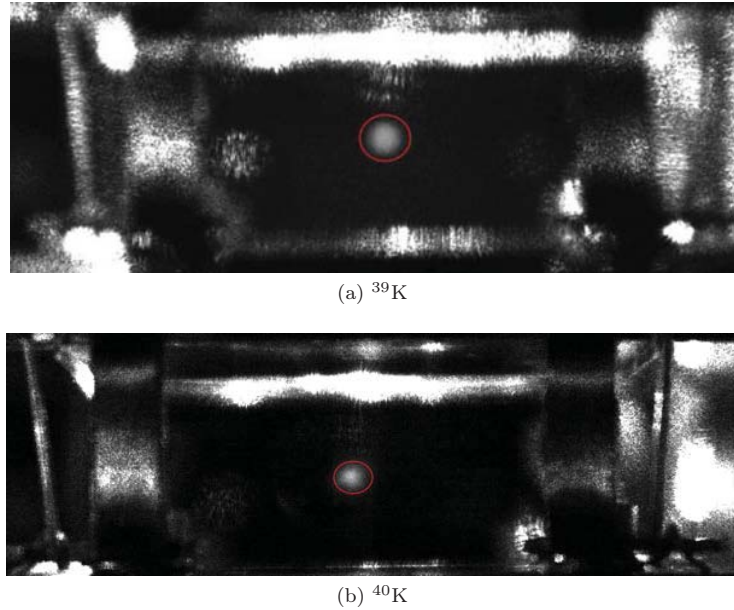


Figure 5.9: Fluorescence images showing the 3D-MOT as a bright spot in the center for  $^{39}\text{K}$  (a) and  $^{40}\text{K}$  (b).

Unlike for  $^6\text{Li}$  the hyperfine splitting for  $^{40}\text{K}$  is rather large and the different states are easily resolved with the typical diode laser line width. Hence it is an ideal atom for applying sub-Doppler cooling, temperatures of  $T_{\text{sub-Doppler}} = 15 \mu\text{K}$  have been reported [113]. Therefore the cooling strategy includes Sub-Doppler cooling for  $^{40}\text{K}$ .

For  $^6\text{Li}$  however Raman side-band cooling [114] might turn out to be good alternative, since it is expected that sub-Doppler cooling cannot not be applied due to the unresolved<sup>15</sup> hyperfine structure splitting of the excited state.

## 5.6 Optical pumping

For the experimental cooling sequence the cloud of cold atoms needs to be prepared in exactly one spin state. Optical pumping can be applied directly after the creation of the 3D-MOT and the application of sub-Doppler cooling for  $^{40}\text{K}$  to put all the atoms in the  $F = \frac{9}{2}$  hyperfine state. This can be done by just driving the transition from the ground state to the excited  $F = \frac{9}{2}$  hyperfine state with laser light resonant at the transition<sup>16</sup>.

---

<sup>15</sup>Using a typical diode laser.

<sup>16</sup>In this case the beam is not detuned as in the case of the magneto-optical trap. This requires changing the laser frequency by a couple of MHz, which is done by changing a AOM frequency in this case.



---

## 6. Cooling to quantum degeneracy

---

In the past chapter it was described how laser cooling can cool the three different atomic species in this experiment down to the lower micro-Kelvin regime. To access the quantum degenerate regime in the low nano-Kelvin regime and to reach the needed phase-space densities, **evaporative cooling** [115] is applied. This technique, since the creation of the first BEC one of the standard cooling techniques in ultracold atom experiments, has been enhanced and adopted for fermionic atoms.

Essentially, a cloud of laser-cooled atoms is trapped, usually in a magnetic or optical dipole trap. Then, heat is taken away from the atoms in the trap by removing the hottest atoms from the trap while thermalization of the trapped atoms takes places. Originally this concept was developed for a magnetic trap, which is shown in figure 6.1: a specific low-field seeking hyperfine spin state (depicted red) is trapped in a magnetic trap in a 'cloverleaf' configuration, which provides an almost harmonic magnetic confinement along one direction and a strong quadrupole-like confinement along the other two directions (more details in the next section 6.1).

Then, a radio-frequency pulse selectively flips the hottest atoms (because of the increasing Zeeman shift for hotter atoms) in the low-field seeking state<sup>1</sup> (red) to an anti-trapped high-field seeking state (blue) and thus the atoms leave the trap. Due to the continuous thermalization of the atoms obeying a Maxwell-Boltzmann velocity distribution [116], the remaining cloud of atoms gets colder and the atom number decreases. As a consequence, one has to sweep the frequency of the RF wave to lower frequency because now the hottest atoms of the colder cloud have a smaller Zeeman shift.

Another possibility is to evaporate in an optical dipole trap, where the magnetic confinement is replaced by an optical dipole trap potential (see section 2.3) that is created by the intensity profile of a Gaussian laser beam. A main difference is that one cannot apply RF pulses to remove the atoms from the trap because there is no Zeeman effect in an optical dipole trap potential that would distinguish between hot atoms and cold atoms. Instead, the laser intensity is decreased and hence the trapping potential lowered such that at some point the hottest atoms can escape because their kinetic energy is larger than the trap potential depth.

In this experiment the atoms are loaded from the 3D-MOT into a harmonic magnetic trap mainly to transport them in front of our microscope. This transport involves moving the atoms along two directions, therefore it is easier to perform a magnetic transport compared to an optical transport<sup>2</sup>. Then, the atoms are loaded from the magnetic trap into an optical dipole trap, where higher trapping depths are reached compared to our magnetic trap, leading to a faster

---

<sup>1</sup>Only low-fields seeking states can be trapped magnetically since it is not possible to create a local maximum of a magnetic field.

<sup>2</sup>Moving a Gaussian beam along two directions is possible but involves challenges in making the transport setup stable and reliable. In one dimension it is easy to translate the focus by translating a lens with an one-dimensional translation stage.

evaporation.

Furthermore,  $^{23}\text{Na}$  can be also evaporated instead of the atomic species  $^6\text{Li}$  and  $^{40}\text{K}$  that are subject to study. This provides sympathetic cooling for the two fermionic species and only the unwanted  $^{23}\text{Na}$  atoms are lost during the evaporation.

The next section describes the implementation of these techniques at length.

### 6.1 Magnetic trapping

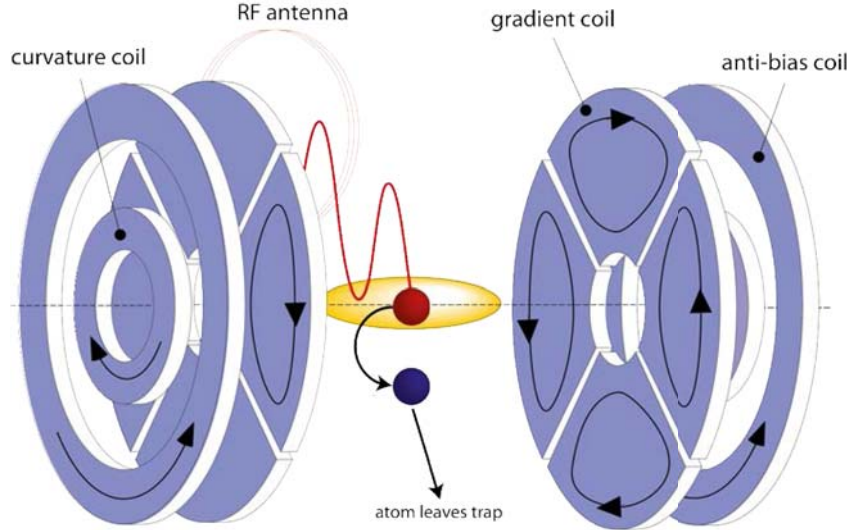


Figure 6.1: Concept of a Cloverleaf magnetic trap and RF evaporation (figure adapted from [41]): a low-field seeking (magnetically trapped) state is flipped to a high-field seeking (magnetically antitrapped) state by a RF pulse and thereby leaves the magnetic trap.

Because static magnetic fields can have local maxima (Wing's theorem, [117]), one can trap neutral atoms only in the low-field seeking hyperfine states. Figure 6.2 shows the shift of the hyperfine structure energy levels with increasing magnetic field, the Zeeman effect. A low-field seeking state is a state whose energy is lower for lower magnetic fields, like for instance the  $|F = \frac{9}{2}, m_F = \frac{9}{2}\rangle$  state for  $^{40}\text{K}$ .

The most simple magnetic field configuration that allows trapping of neutral atoms is the quadrupole configuration, where typically a pair of coils running current in opposite direction provides a spatially varying field that is minimal in the center between the coils and increases linearly for increasing distances from the trap center (hence the magnetic potential is linear).

A more sophisticated configuration of a magnetic trap is the Ioffe-Pritchard trap. This type provides a harmonic confinement with an offset along one direction, which is advantageous for reasons that will become clear in the next section (avoiding losses of atoms in the so-called Majorana hole).

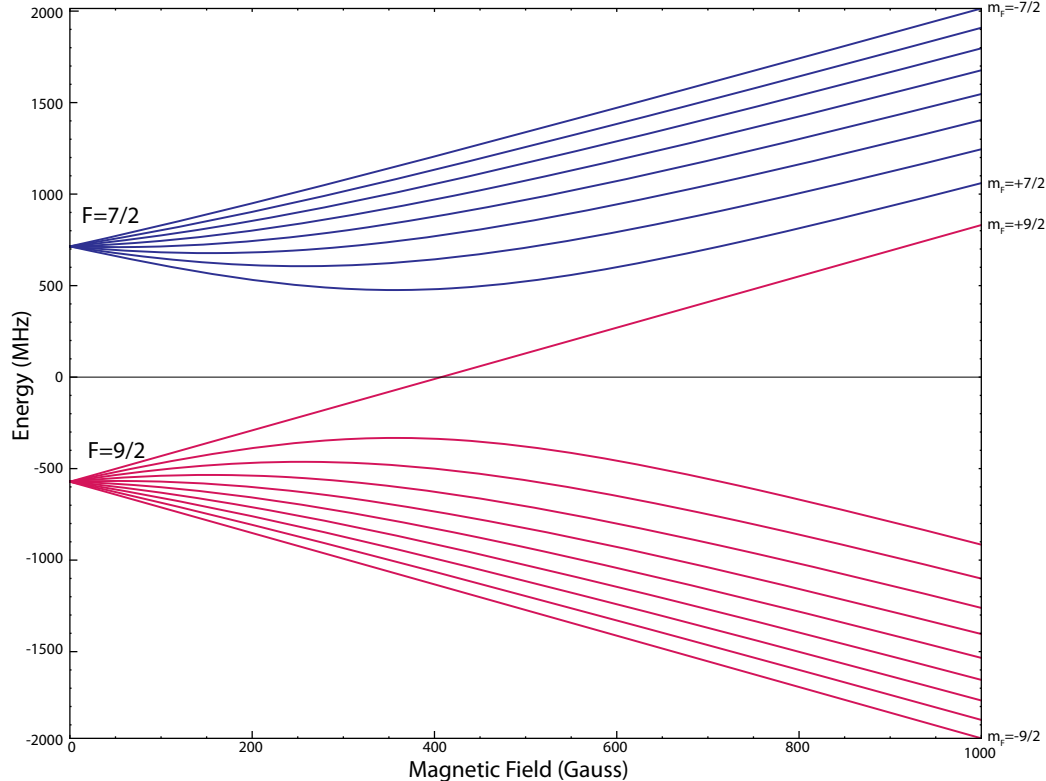


Figure 6.2: Shift of the hyperfine energy levels due to the Zeeman effect for  ${}^{40}\text{K}$ .

In this experiment a combined type of these two conservative magnetic traps has been designed and implemented for this experiment, which is described in this section.

### 6.1.1 Design of the magnetic trap

In this experiment several constraints on the mechanical setup of the magnetic coils providing the trapping and Feshbach fields governed the design process of the magnetic trap. Most importantly, the magnetic trap must be suitable to capture the atoms at the position of the MOT, which is  $d = 12$  mm away from the center of the imaging system (see chapter 4.4.2). In addition a tight magnetic trap with a trapping frequency of  $\omega = 200$  Hz in the strongest direction and Feshbach fields up to  $B_{\text{FB}} = 1000$  G must be achievable.

Furthermore, trap losses due Majorana spin flips [118] need to be avoided. Since the atom loss rate is proportional to  $\frac{1}{\text{temperature}^2}$  [115], this is only important for cold clouds.

As a result, magnetic trapping is provided by two different traps, which can be run independently: A magnetic quadrupole trap [119] which is centered around the MOT position (purple cloud symbolizing the atomic cloud in figure 6.3) and a Ioffe-Pritchard trap in a cloverleaf configuration [120] that is centered coaxially with the center axis of the imaging system, where the atoms are

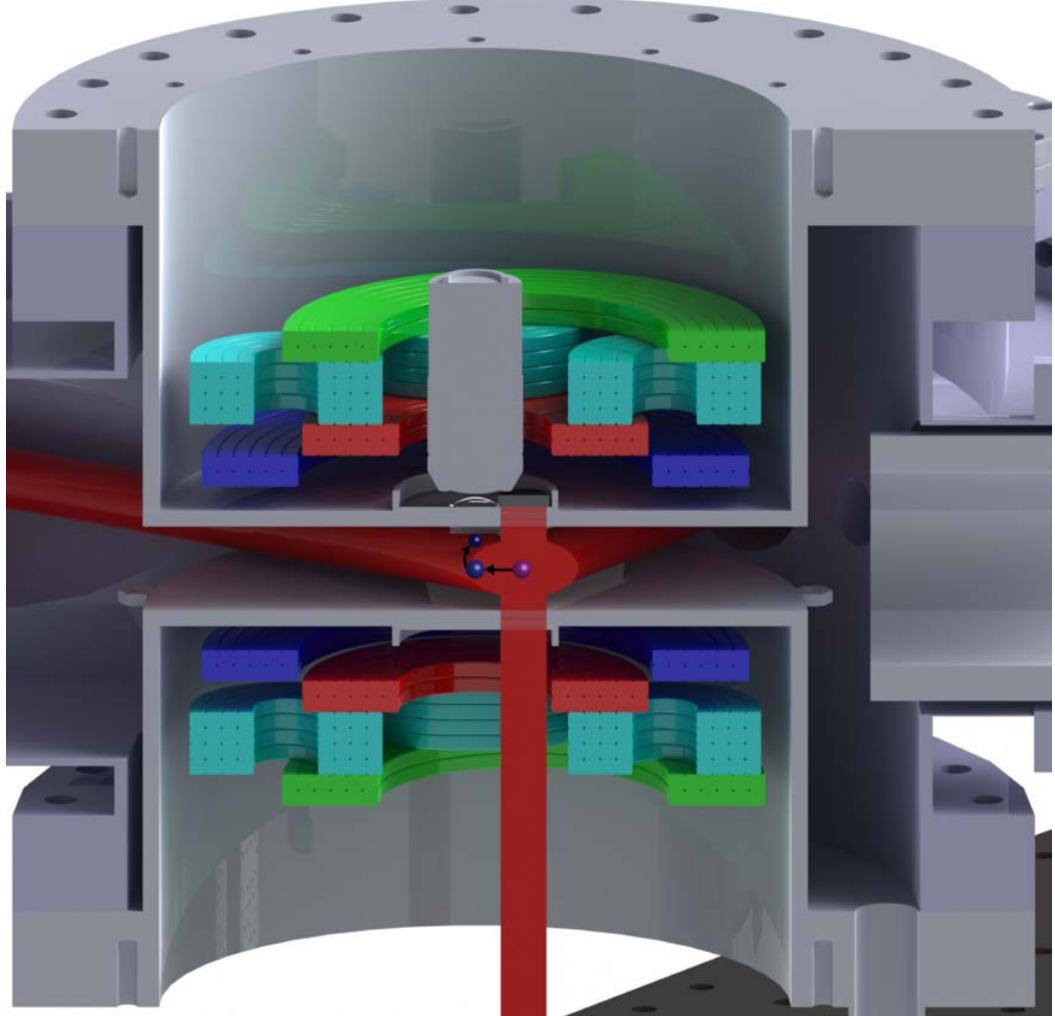


Figure 6.3: Magnetic transport of the atomic cloud at the initial 3D-MOT position (purple sphere) to the center of the chamber (big blue sphere, evaporation is performed here) and towards the objective (small blue sphere).

being evaporated (big blue sphere in the figure). The center of the Ioffe-Pritchard trap [121] can be moved towards the microscope objective by imbalancing the currents in the magnetic coils in order to move the atoms to the focal point of the imaging system.

Based on this concept a design was worked out with a magnetic field simulation program<sup>3</sup> and a CAD program<sup>4</sup> with the following most important constraints:

---

<sup>3</sup>Radia simulation package for Mathematica [122] for simulating magneto-static fields using a boundary integral method [123].

<sup>4</sup>SolidWorks by Dassault Systèmes SolidWorks Corporation.

- dimensions of the bucket<sup>5</sup> of the re-entrant viewport (precise drawing in appendix C.1)
- fitting of a microscope inside a hole ( $d = 38$  mm) in the magnetic coils in the upper bucket, as shown in figure 6.3.
- Ioffe-Pritchard trap as main magnetic trap, center shifted from center of the vacuum chamber ( $\vec{x}_{IP} = (12 \text{ mm}, 0, 0)$ )
- magnetic quadrupole trap to be used for MOT and loading the main magnetic trap, center aligned with center of vacuum the chamber ( $\vec{x}_{MOT} = \vec{x}_0 = (0, 0, 0)$ )
- possibility to create constant magnetic fields up to  $B_{FB} = 1000$  G for using Feshbach resonances
- cooling with chilled water ( $T_{water} = 15$  °C), temperature of cooling water should not rise more than about ten degrees Celsius
- perfect fit with the re-entrant viewport

Figure 6.4 provides a CAD illustration of the computed coil configuration, which is also shown in the CAD cross-section illustrations of the main experiment chamber like figure 6.3.

Besides the additional MOT coil (drawn in green) for the spatially separated MOT/quadrupole trap two main differences to the original cloverleaf design (figure 6.1) have been made:

First, the cloverleaf coils (light blue) are between the curvature (red) and the MOT/quadrupole coils (green). This is mainly because of the emersed edge around the window, which makes it favorable to put the Feshbach closest to the chamber wall<sup>6</sup>. The shape of the cloverleaf coils has been optimized to simplify the manufacturing process and maximize the possible number of turns at the same time.

Second, the curvature (red) and the antibias/Feshbach (blue) coil are not coplanar but shifted with respect to each other. While the curvature coil could not be placed further towards the vacuum wall, the antibias/Feshbach coils have been positioned closer to the vacuum wall (and hence the pair of coils is now closer together) to increase the maximal possible magnetic Feshbach fields.

A detailed description of the cloverleaf configuration of an Ioffe-Pritchard trap is given for instance in [44], therefore only one important point should be emphasized because of the implications for the electrical setup: A main idea of the Ioffe-Pritchard trap is that two pairs of coils (the curvature and the anti-bias coils) are connected such that the homogeneous components of the magnetic field cancel and the curvature components of both coils add up since only the latter one can be used to trap atoms.

---

<sup>5</sup>The diameter of the bucket is limited by the mechanical dimensions of the main vacuum chamber and has been maximized, clearly visible in figure 6.3.

<sup>6</sup>In the CAD design the space consumption for the glue which holds the coils together, additional mechanical features of the vacuum windows and imperfections of the coil manufacturing process have been taken into account. Therefore one can see a gap between the vacuum chamber walls and the coils (curvature (red) and antibias/Feshbach(blue)) in figure 6.3.

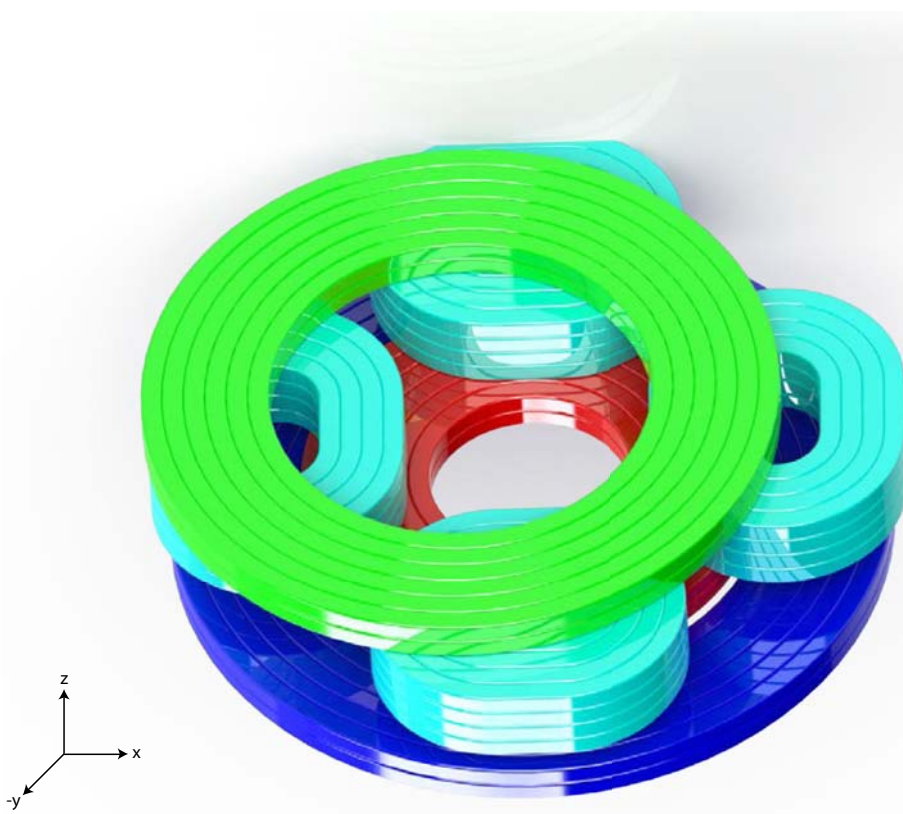


Figure 6.4: CAD rendered picture of one set of magnetic coils. The two different principal centerline axes for the MOT coil (green) and the other coils are visible. Two sets of these coils make up the magnetic trap as shown in figure 6.3.

But, when two large currents of almost equal magnitude are subtracted, this can cause large fluctuations. This problem can be circumvented by running the same current through both the curvature and the antibias coils. In this configuration any fluctuations are canceled if both produce the same magnetic field per unit current. Since the antibias/Feshbach coils in this setup produce a higher field per unit current due to the smaller separation of the coils, some of the current needs to be bypassed<sup>7</sup>. Section 6.1.4 describes how this is realized.

### 6.1.2 Fabrication of magnetic coils

For the fabrication of the magnetic coils a special hollow copper coil wire with a rectangular cross section and fiber glass insulation has been used<sup>8</sup>. This optimizes the packaging of different layers compared to round copper wire and enables one to cool the magnetic coils with water.

---

<sup>7</sup>Basically, a bypass varistor is used in way such that the current in antibias coil is about 80% of the current in the curvature coil.

<sup>8</sup>Outer side length  $\frac{1}{8}$ " = 3.175 mm, inner side length  $\frac{1}{16}$ " = 1.5875 mm.

The design of the magnetic traps requires many different coils of different size, which were manufactured individually and then put together. The following table lists the basis properties of the manufactured coils:

Coil	Layers	Turns	Cooling circuits	Color in figure 6.4	Inner diameter	Inner distance to center
Curvature	2	5	2	red	19 mm	29 mm
Antibias/Feshbach	4	5	1	blue	21 mm	21 mm
Cloverleaf	2	5	2	light blue	8 mm	41 mm
MOT	2	5	2	green	36 mm	53 mm

Table 6.1: Properties of the magnetic coils. The coil referred as 'MOT' is used for creating the 3D-MOT and subsequently used as magnetic quadrupole coil by running a higher current through the same coil.

Based on these parameters the coils were manufactured on a modified lathe<sup>9</sup> shown in figure 6.5a. Precisely cut aluminum molds were used to wind the coils around them and additional guiding pieces made out of aluminum and acrylic help guiding the coil wire. Each layer of the coils was wound separately while continuous application of epoxy<sup>10</sup> fixed the coil wire permanently.

For the cloverleaf coils a fast-curing epoxy<sup>11</sup> had to be used since 4 layers had to be manufactured at once (compared to the layer-wise manufacturing of all other coils). Figure 6.5b shows a readily manufactured cloverleaf coil.

All individually fabricated coils have been put together into two magnetic coil packages: As shown in figure 6.5c the coils have been aligned with the help of machined plastic pieces to resemble the configuration in figure 6.4. Then, the special non-magnetic high-temperature rated epoxy<sup>12</sup> was casted into the bucket made up by the plastic pieces such that all coils were covered. The resulting magnetic coil package is shown in figure 6.6a, where temperature sensors have been added.

### 6.1.3 Water cooling

Running currents of up to  $I = 500 \text{ A}$  through the coil wire demands cooling with chilled water. In average a power of

$$P_{\text{coil}} = 500 \text{ A} \cdot 4 \text{ V} = 2000 \text{ W} \quad (6.1)$$

per coil is dissipated while running the maximal current. Due to the small inner tube cross-section of the coil wire of about  $d = 1 \text{ mm}$  the conductivity of the long coil wire is rather low and standard cooling water with a pressure of about  $p = 80 \text{ psi} \approx 5.5 \text{ bar}$  (low-pressure water) does not provide enough cooling power.

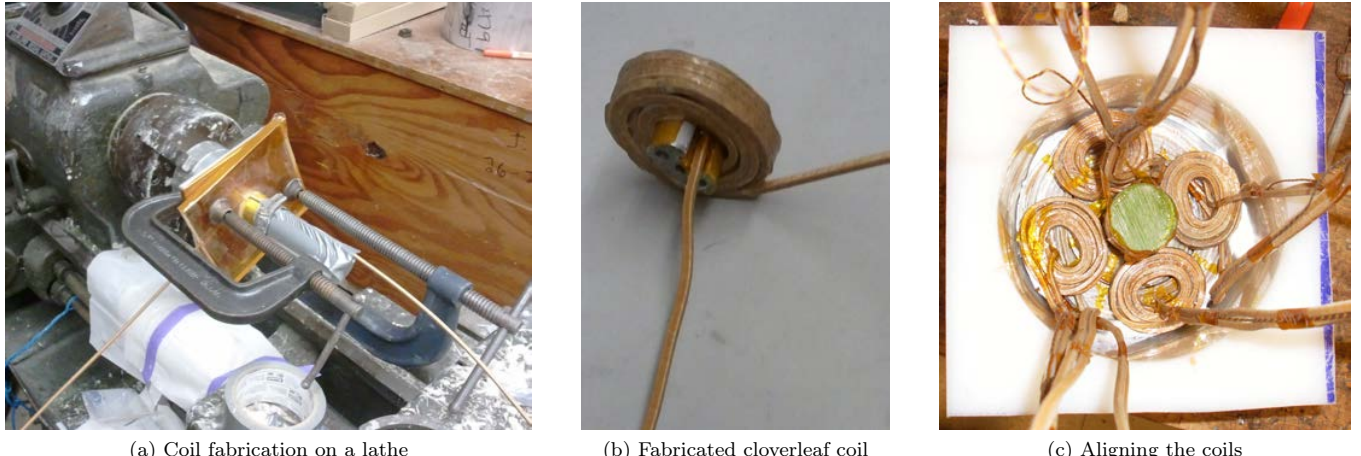
---

<sup>9</sup>The engine of the lathe has been slowed down to about  $\frac{1}{4} \frac{\text{turns}}{\text{s}}$  to make it suitable for winding magnetic coils.

<sup>10</sup>*Cotronics corp.* NM25 non-magnetic epoxy.

<sup>11</sup>3M 5-minute epoxy.

<sup>12</sup>*Cotronics corp.* NM25 non-magnetic epoxy with Cotronics thinner.



(a) Coil fabrication on a lathe      (b) Fabricated cloverleaf coil      (c) Aligning the coils

Figure 6.5: Pictures of the fabrication of the coils on a lathe (a), a readily manufactured cloverleaf coil (b) and the alignment in a special structure to glue them together (c).

Therefore a high-pressure water cooling system has been developed that can provide cooling water with pressures up to  $p = 600 \text{ psi} \approx 41.2 \text{ bar}$  (in this context called high-pressure water). These high pressure cooling water circuits require special tubing<sup>13</sup> and a good flow regulation that controls the flow through the high-pressure pump. This is especially important since all typical high-pressure water pumps for not-tempered or cooling water use the pumped water to cool the engine. If there is not a sufficient flow through the pump itself, the pump will be destroyed due to overheating (observed in other labs which have not implemented a flow control in their water cooling system).

The high-pressure water is not only provided for the coils of the magnetic trap described in this chapter but also for the magnetic coils of the Zeeman slower (see 5.2). An additional low pressure circuit supplies cooling water for electronic devices that need water cooling (IGBTs, laser amplifiers). Figure 6.7 shows schematically the water cooling system for this experiment: The whole system is a closed circuit and a heat exchanger with a reservoir (left side, blue box) is used to exchange the heat to the building cooling water supply<sup>14</sup>. The pump in the heat exchanger (inside the blue frame) maintains a low pressure that is directly fed into the low-pressure circuit.

A high-pressure pump creates high-pressure in the high-pressure circuits with two separate loops with separate temperature and pressure control<sup>15</sup>. Several filters are build into the circuit (not shown in the schematic) in order to prevent the small tube of the coil wiring from clogging. Additionally, using deionized water in this closed circuit reduces sediments.

Temperature and pressure gauges are installed in each circuit before and after the heat load. Furthermore, all magnetic coils have temperature sensors build in, which can be electronically

<sup>13</sup>Tubing was bought from Swagelock®Corporation.

<sup>14</sup>Direct use of the building water supply would clog the small tubes of the coil wire.

<sup>15</sup>In this configuration the water flow is distributed more uniformly over the different coils that need to be cooled.

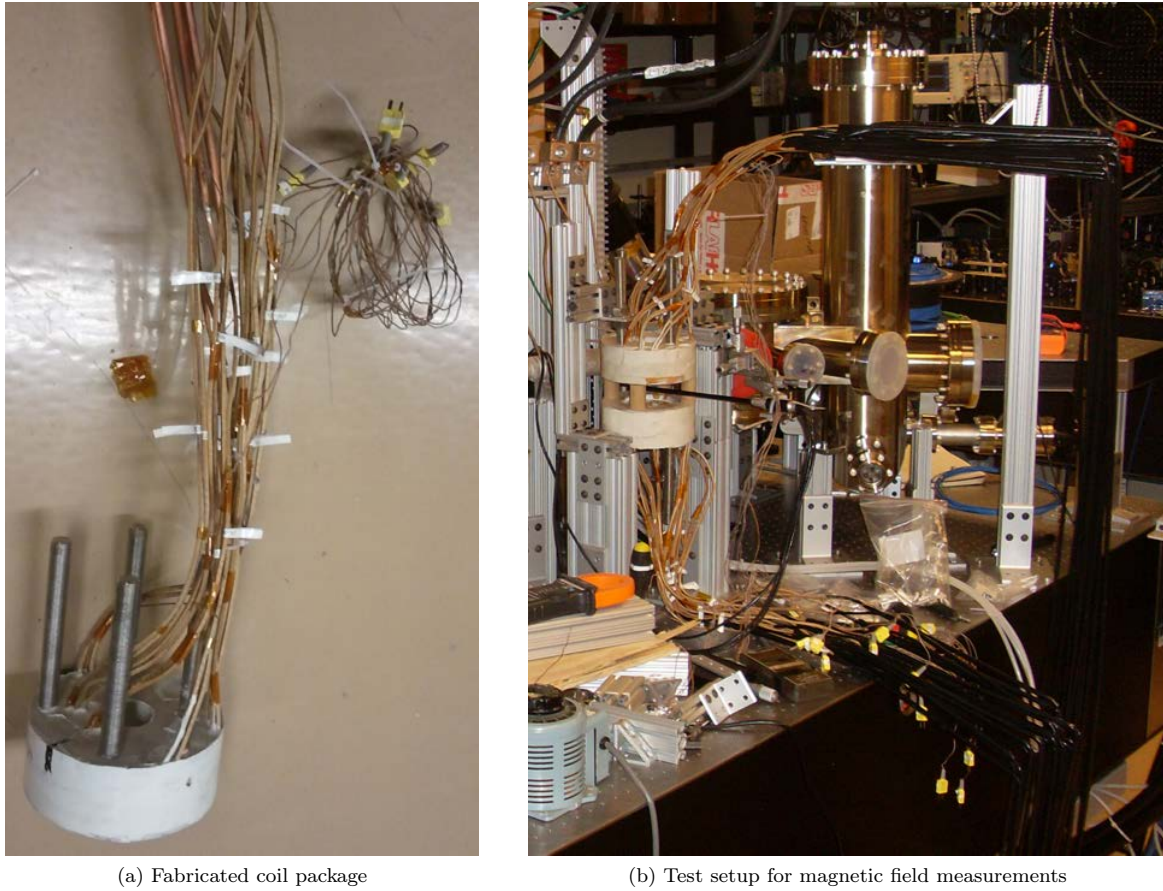


Figure 6.6: Pictures of the readily manufactured coil package (left) and the setup for the magnetic field test (right) with magnetic field probe (long black rod) on a three-axis translation stage, described in detail in the text.

monitored (visible cords with yellow plugs in picture 6.6a). A home-made electronic interlock box monitors the temperature and shuts down all power supplies in case one measured temperature exceeds a maximal temperature set-point.

#### 6.1.4 Electrical connections

Four power supplies (Lambda Corporation ESS Series) power the magnetic coils, which are connected in several circuits. As shown in figure 6.8, one main circuit provides the same current for all the anti-bias and the curvature coils. This is necessary to stabilize the magnetic field: Any fluctuation is canceled out since the same current is running through the curvature and the anti-bias coil in different directions. However, this is only true to a certain extend since the created magnetic fields are slightly different since the anti-bias coil is positioned closer to the center. With two different methods the current in anti-bias coils can be reduced with respect to

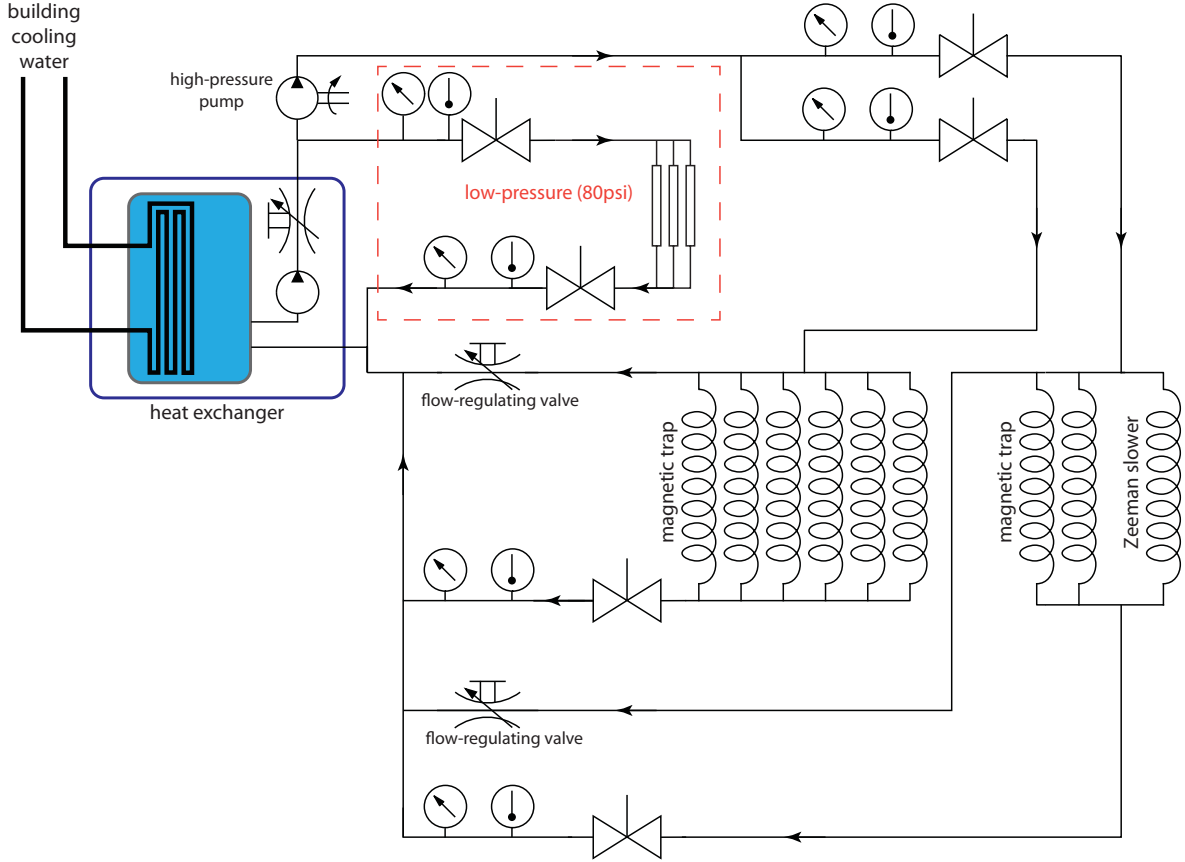


Figure 6.7: Schematic diagram showing the water cooling setup of the experiment (symbols according to DIN/ISO 1219, [124]), explained in detail in the text.

the current in curvature coil. A resistor and variable resistor provide good tunability to reduce the current in the Feshbach coil permanently. A MOSFET (which can take up to  $I = 100$  A) that is connected in parallel can be used to dynamically stabilize the magnetic fields with an electronic feedback system.

All power supplies have been placed in a 19"-rack outside of the main laboratory to reduce electronic and acoustic noise. This configuration also improves the thermal stability of a lab<sup>16</sup>.

The ESS series switching power supplies manufactured by Lambda (now TDK-Lambda) can provide the electric power for the magnetic traps with up to  $I_{ps} = 500$  A at up to  $U_{ps} = 30$  V. Due to the resistance of the coils not all circuits can be run at the maximal current of the power

<sup>16</sup>Power supplies with powers of  $P = 15$  kW produce a quite large heat load (even the switching power supplies). This large flow of hot air cause the air conditioning to put in more cool air causing more air flow and hence reduce the stability of the temperature.

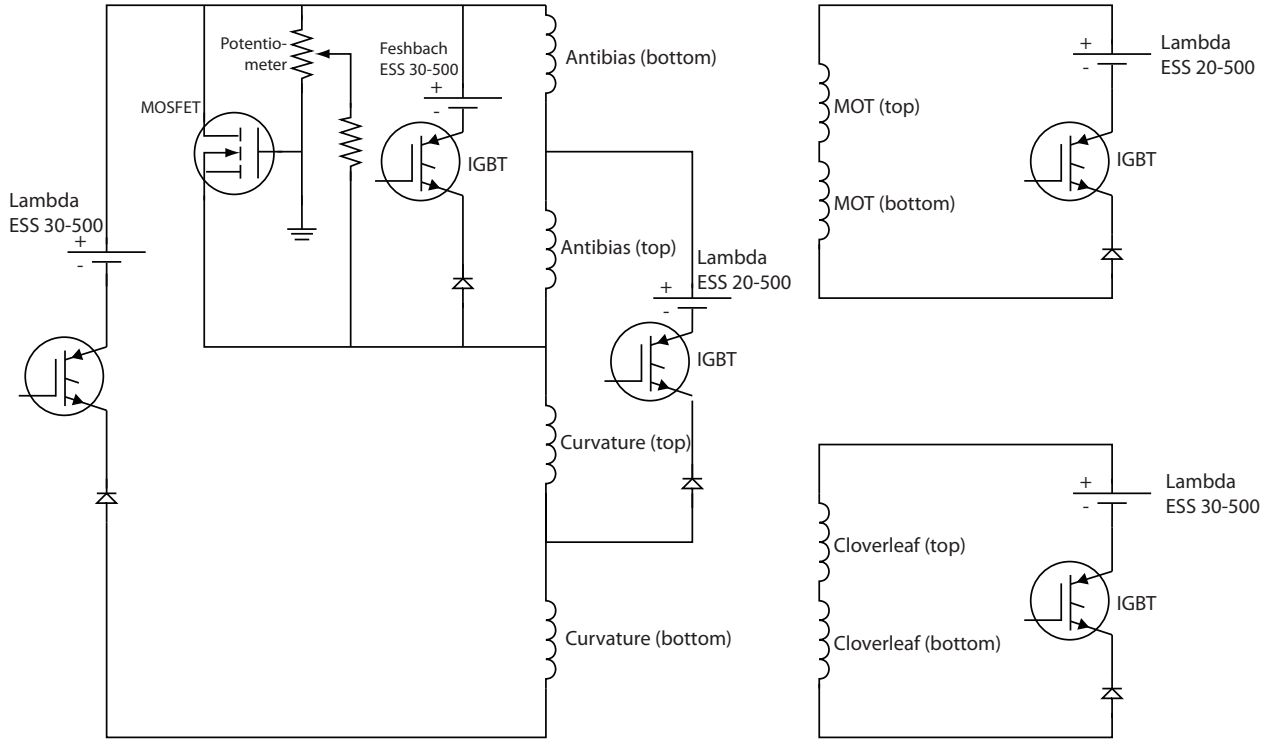


Figure 6.8: Schematic of the electric setup of the power supplies powering the magnetic coils, explained in the text.

supply because of the voltage limitation of the power supplies. Table 6.2 shows the electrical specifications of the coils in the current setup.

In a cold atom experiment it is important to be able to modify the magnetic field very quickly, especially for Feshbach resonances. The ramp time of the power supplies (typically on the order of seconds) is usually too slow and IGBTs are used to switch current very quickly. Industrial grade IGBTs have been used and the driver electronics with a computer control input have been designed and manufactured (details in appendix E.1). All IGBTs and all the power supplies are connected to the computer system and all parameters (current, voltage and IGBT) can be controlled with an analog channel with 16 bit precision.

### 6.1.5 Test of magnetic coils

The readily manufactured and assembled coils have been arranged in a temporary test configuration (see picture in figure 6.6b) to characterize the magnetic fields. This arrangement resembles

Coil	Resistance for whole circuit	Maximal current at 30 V
Curvature and Antibias/Feshbach	$R = 0.1129 \Omega$	265.7 A
Antibias/Feshbach	$R = 0.0675 \Omega$	444.4 A
Cloverleaf	$R = 0.1237 \Omega$	242.6 A
MOT	$R = 0.0646 \Omega$	464.6 A

Table 6.2: Electrical specifications of the manufactured coils: The resistance is given for the whole circuit including the switching IGBT with a diode. The maximal current is given for the configuration where one power supply powers all coil layers of one coil type (compare figure 6.8).

the final setup inside the re-entrant viewports of the main chamber and gives an indication for the maximal achievable magnetic fields.

A magnetic field probe<sup>17</sup> mounted on a three-axis translations stage has been used to record the spatial dependence of the magnetic fields created by the different traps, shown in figure 6.9.

As a result of the measurements Feshbach fields of up to  $B_{FB} = 1190$  G and radial gradients of up to  $B'_{rad} = 165$  G/cm can be created using the theoretical maximum current of the power supply ( $I_{max} = 500$  A).

However, in this setup the same current was used for the curvature and the antibias coil. Because of the different geometries and since no additional balancing of the constant component of the magnetic field was done (details described in 6.1.4), the offset in the axial magnetic field (figure 6.9a) is quite high in these measurements and explains the need for the balancing described in the referred section and in figure 6.8.

### 6.1.6 Gravitational sag

One problem that is immanent in multi-species magnetic traps is the so-called gravitational sag. When using conventional quantum gas experiments permanently set up on the earth, the gravitational force of the earth is acting along one axis (can be circumvented in free falling towers in which a gravity-less BEC has been demonstrated [125]) and causes a spatial separation of atoms with different masses in a harmonic trap (in this case the magnetic trap).

Starting from a harmonic trap potential with trapping frequency  $\omega_z$  along the z-direction (in our setup the axis aligned with gravity)

$$V_{\text{tot}}(z) = V_{\text{mag}} + V_{\text{grav}} = \frac{1}{2}m\omega_z^2 z^2 + mgz, \quad (6.2)$$

one can see easily that its minimum shifts by

$$\Delta z = z_{\text{min}}^{V_{\text{mag}}} - z_{\text{min}}^{V_{\text{mag}}+V_{\text{grav}}} = -\frac{g}{\omega_z^2}. \quad (6.3)$$

It is important to note that in this configuration the weak harmonic trapping axis is aligned along gravity. Hence this effect is quite significant for very cold clouds in which the atoms are

---

<sup>17</sup>Three-Axis Hall effect Gaussmeter by FW Bell Inc.

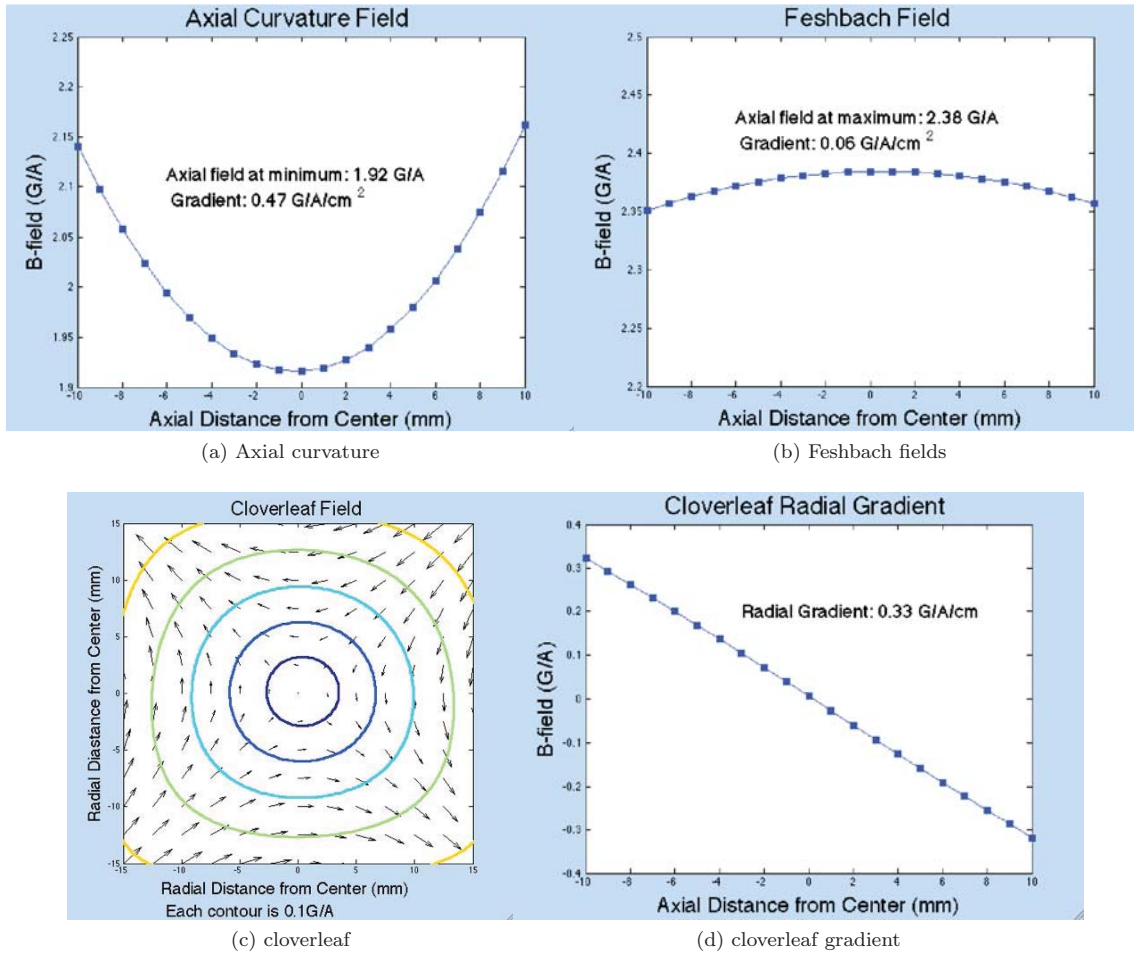


Figure 6.9: Magnetic field measurements of the magnetic trap.

located very close the center of the trap and the cloud size is very small. A consequence is that different hyperfine states of an atom as well as different atomic species are spatially separated since they have different magnetic moments and hence the minimum of the trapping potential changes.

Two solutions to circumvent this problem are very popular: A rotation of the whole experiment can bring gravity along one of the strong axes of the magnetic trap, where the effect is smaller because the trapping frequency is higher and the gravitational sag decreases quadratically with  $\omega$  (for instance done in [90]). This is not possible in our experiment, though, since the microscope imaging setup and the triple-species setup are very hard to construct in this position.

Another way is to use an additional optical dipole trap along one of the axes orthogonal to gravity

in order to provide a strong confinement along the axes of gravity (see details in section 2.3). The optical dipole force of a far-detuned laser beam is the same for the different hyperfine states (therefore optimal for evaporation of two hyperfine states of a fermionic species), but different for species with different electronic structure. This is commonly referred as a hybrid trap [41]. More details are given in section 6.3.3 at the end of this chapter.

## 6.2 Magnetic transport

Setting up the MOT 12 mm away from the center axis of the imaging systems solves the problem of optical access for the six MOT beams (one is retro-reflected with a small mirror inside the re-entrant viewport, see section 4.4.2). However this configuration demands a mechanism to transport the trapped and laser-cooled atoms in front of the imaging setup with the microscope objective. Two main transport mechanisms turned out to be especially suitable for transporting trapped atoms: transport in an optical dipole trap<sup>18</sup> and transport in a magnetic trap by translating the minimum of the magnetic field. The latter one is realized in this experiment.

A magnetic transport can be implemented in many ways that yield the same result: One can move the magnetic field minimum by moving the coils that create the magnetic field with mechanical translation stages (see for instance [126]). Another possibility is to put several individually switchable coil pairs overlapping along the transport path which are switched on and off subsequently [127]. Here, a transport scheme on based on the second variant was developed and implemented.

Since in this experiment the transport distance is very short ( $d_{\text{trans}} = 12 \text{ mm}$ ), the transport can be implemented with all the coil pairs that are part of the Ioffe-Pritchard trap in the cloverleaf configuration and the magnetic quadrupole trap at the MOT position. The principal idea here is very simple: While the magnetic quadrupole trap at the MOT position is ramped down, the Ioffe-Pritchard trap is ramped up at the centered position and with this the minimum of the magnetic field moves towards the center of the Ioffe-Pritchard trap.

### 6.2.1 Current ramps

Ramping up and down both magnetic traps can be done in our experimental setup by modifying the electric current. Since all power supplies and the IGBTs (see section 6.1.4) are connected to computer control software with analog control channels, arbitrary current ramps can be run. Using the Mathematica simulation that has been used for the simulation for both magnetic traps a sophisticated current ramping scheme has been worked out.

Figure 6.10 shows one possible ramping scheme (assuming a maximal current of 500 A): While the currents in the MOT/quadrupole coils are ramped down quadratically ( $T$  denotes the total ramp time, the time duration of the magnetic transport),

$$I_{\text{quadrupole}}(t) = I_{\text{initial}}^{\text{quadr.}} \left( 1 - \frac{t^2}{T^2} \right) \quad (6.4)$$

---

<sup>18</sup>The focus of the Gaussian laser beam making up the optical dipole trap is translated by moving lenses mechanically.

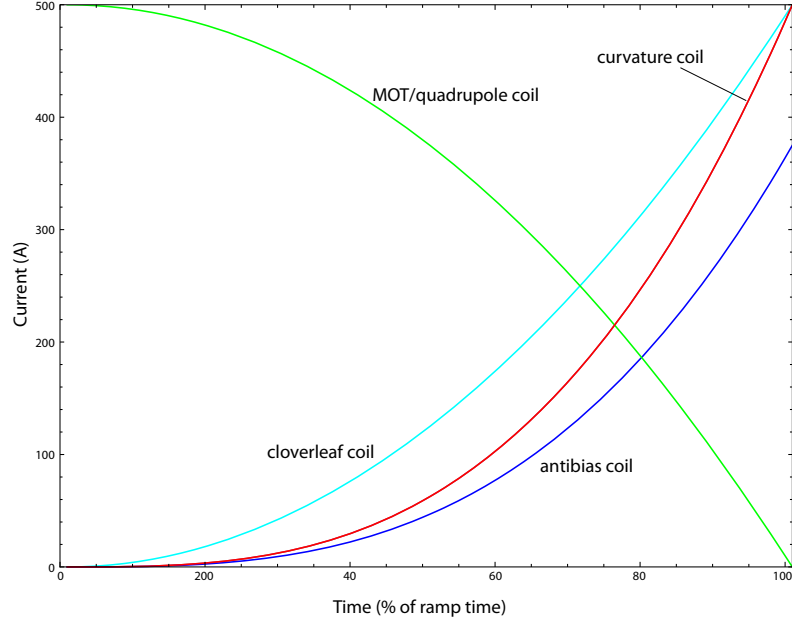


Figure 6.10: Graph showing a possible example of current ramps to move the atoms from the magnetic quadrupole to the Ioffe-Pritchard trap as described in the text.

the curvature and the antibias currents are ramped quadratically

$$I_{\text{curvature}}(t) = I_{\text{final}}^{\text{curvature}} \frac{t^2}{T^2} \quad (6.5)$$

$$I_{\text{antibias}}(t) = I_{\text{final}}^{\text{antibias}} \frac{t^2}{T^2}. \quad (6.6)$$

The cloverleaf currents ramp up cubically in time:

$$I_{\text{clover}}(t) = I_{\text{final}}^{\text{clover}} \frac{t^3}{T^3}. \quad (6.7)$$

As one can see in the figure, the final current of the antibias coils is lower than the final current of the curvature coil, because the spacing of the antibias coil pair is smaller than the ideal configuration as explained in section 6.1.4.

In figure 6.11 the magnitude of the simulated magnetic field of the transport scheme (5 timesteps) is shown as two two-dimensional plots. The first column 6.11a shows the magnetic field magnitude in the horizontal plane ( $x$ - $y$ -plane) and the second row 6.11b along a vertical plane ( $x$ - $z$ -plane). As one can see clearly, the minimum moves along the  $x$ -direction (see coordinate system in figure 6.4) from right to left, the left column shows the view 'from the top' and the right column shows the view 'from the side'.

It is important to note that the magnetic transport is yet to be implemented in practice and can be potentially improved (see for instance the second last graph of the left column in figure 6.11).

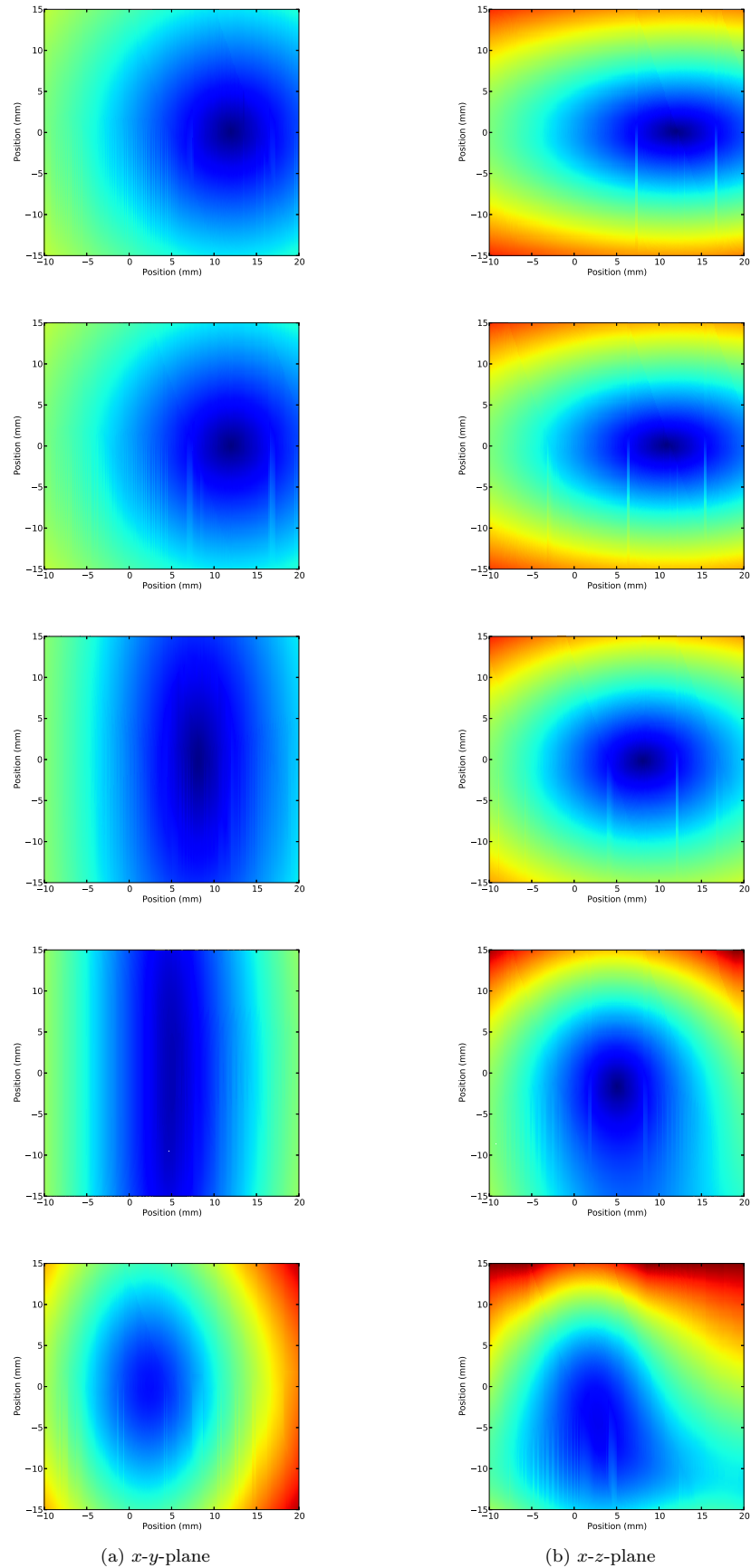


Figure 6.11: Magnitude of the magnetic field during ramping from the quadrupole trap to cloverleaf trap along the  $x$ - $y$ -plane (a) and the  $x$ - $z$ -plane.

Since the numerical computer simulation does not handle any experimental imperfections, the transport current ramps should be optimized after the magnetic trap has been set up. At the time of writing the magnetic coils have been set up at their final place and tested as figure 7.2b in next chapter shows. The magnetic quadrupole trap (MOT trap) is already functional and the first  $^{40}\text{K}$  atoms have been trapped, see figure 8.2 in chapter 8.

### 6.3 Evaporative cooling

Evaporative cooling [115] turned out to be the key technique to cool dilute gas samples down to quantum degeneracy: atoms are trapped in a magnetic or optical trap and during constant thermalization due to collisions the hottest atoms are kicked out such that the remaining cloud cools down. One difficulty with cooling fermions to quantum degeneracy is the Pauli blocking [47]: a spin-polarized fermigas (a fermigas where only one spin state is populated) does not exhibit any collisions and there is no thermalization.

Typically one either evaporates two different spin states at the same time such that thermalization is given by the collisions of different spin states [128] or uses a bosonic species as sympathetic coolant (suggested in [129], this experiment will use  $^{23}\text{Na}$  as a sympathetic coolant like described in [41]). This experiment will be suitable to perform both methods, which will be described in this section.

In the majority of cases the atoms are evaporated in a magnetic trap. This is notably convenient because 'kicking' atoms out of the trap can be very easily realized by using a RF-driven electronic transition to flip atoms to a magnetically anti-trapped state (see figure 6.2 for magnetically trapped and anti-trapped states) that causes the atoms to leave the trap.

Since the first main goal of this experiment is to evaporate  $^{40}\text{K}$ , both the two-spin state evaporation and sympathetic cooling will be described for  $^{40}\text{K}$  in this chapter.

#### 6.3.1 RF antenna

A RF antenna is part of the standard toolkit in a cold atom experiment as it drives not only the RF transitions that are used for evaporative cooling but can be also used to drive other transitions between different spin states whose energy difference is in the RF spectral region. Important examples are the preparation of a fermi gas in a special spin state (spin-polarized fermigas) and RF spectroscopy.

Based on the experiences of the other experiments, an RF antenna has been made that is broad-band and can be put inside the vacuum chamber. Thus it can be placed very close to the atomic sample and less power is needed compared to an antenna outside the vacuum chamber. The broad frequency susceptibility ensures versatility during the long lifetime of such an ultracold atom experiment.

Like figure 6.12 shows, the RF antenna consists of two loops of a special oxygen-free copper wire that has been mounted to one of the re-entrant viewports. The oxygen free copper wire<sup>19</sup> is

---

<sup>19</sup>Oxygen-free copper is used because much less oxygen is released into the vacuum chamber and thereby the vacuum is improved.



Figure 6.12: RF antenna for evaporation mounted on one re-entrant viewport.

insulated with a polyimide film<sup>20</sup> to insulate it electrically from the metallic mounting screws.

The copper wire is spot-welded on one end to the electrical feed-through, which allows the connection to an electronic RF source from the outside.

### 6.3.2 Evaporation of a two-component fermi gas

Evaporation of a two-component fermi gas in a magnetic trap presumes the preparation of magnetically trapped states in the magnetic trap with favorable collisional properties. For  ${}^{40}\text{K}$  a good configuration is the mixture of the  $|F = \frac{9}{2}, m_F = \frac{9}{2}\rangle$  and the  $|F = \frac{9}{2}, m_F = \frac{7}{2}\rangle$  state, which are magnetically trappable.

An arbitrary frequency generator<sup>21</sup> is used to drive the RF transition to the  $|F = \frac{7}{2}, m_F = \frac{7}{2}\rangle$  which is not trapped and causes the atoms to leave the trap (the transition frequency is on the

---

<sup>20</sup>This material is commonly known under the name Kapton®.

<sup>21</sup>DDS function generator PXI-5650 from National Instruments.

order of 1.2 GHz). To extend the range of operation the output frequency is doubled before it is amplified<sup>22</sup> and fed to the experiment, this allows creation of frequencies of up to 2.6 GHz.

Since a cold cloud is smaller than a hot cloud, the transition frequency and thus the Zeeman shift of the energy changes, the RF frequency needs to be adjusted continuously as evaporation proceeds. This can be programmed on a computer, which is connected via the National Instruments PXI bus to the function generator.

### 6.3.3 Sympathetic cooling

A major disadvantage of sympathetic cooling is the atom loss of the species that is evaporated. Instead, one can use two different atomic species with good collisional properties to ensure good thermalization and evaporate one of the species. The other species will be just cooled due to thermalization with the evaporated species which is known as **sympathetic coolant**.

Obviously this requires the handling of another species (the atomic source and the laser cooling setup has to be build for this species as well) but since one can evaporate the sympathetic coolant until no atoms are left one can reach very cold temperatures with this method. In this experiment <sup>23</sup>Na was added as a sympathetic coolant. From previous experiments it is known that the collisional properties with <sup>40</sup>K [81] and <sup>6</sup>Li [130] are good and sympathetic cooling is favorable.

However, it is not very favorable to evaporate two different species in a magnetic trap that is subject to gravity because of the different magnetic moments and the different masses (leading to a different gravitational sag, see section 6.1.6). Therefore both species will be loaded into an optical dipole trap, which provides a tighter confinement compared to the purely magnetic trap.

Besides evaporating in purely optical dipole trap (a crossed optical dipole trap is used very often since a single optical dipole trap provides a strong confinement only along two directions, but a crossed optical dipole trap along all three directions) the two species mixture can be evaporated in a hybrid trap as well. In this configuration a single-axis optical dipole trap and and magnetic trap (in this case the Ioffe-Pritchard trap in the cloverleaf configuration) are confining the atoms simultaneously.

Evaporation in a purely optical dipole trap can be done by ramping down the laser light power such that the hottest atoms automatically leave the trap because their energy is higher than the trap depth.

For optical dipole traps the depth of the potential depends on the detuning of the laser frequency with respect to the atomic transition and is in general different for different atomic species. For sympathetic cooling of <sup>40</sup>K with <sup>23</sup>Na the detuning is quite different ( $\lambda_{\text{laser}} = 1064 \text{ nm}$ ,  $\lambda_K^{D_2} = 766.7 \text{ nm}$ ,  $\lambda_{\text{Na}}^{D_2} = 589.2 \text{ nm}$ ) but luckily the gravitational sag is overcompensated by the effect of different optical dipole trap potentials for a given laser power due to the different detuning. As a result the <sup>23</sup>Na has a larger detuning and hence shallower optical dipole potential and will leave the trap first when the potential is slowly ramped down. This makes sympathetic cooling of <sup>40</sup>K with <sup>23</sup>Na very favorable and will be employed in this experiment as well.

---

<sup>22</sup>Conventional RF amplifier from Minicircuits.



---

## 7. An imaging system for fermions with single-atom and single site-resolution

---

A central part of a quantum gas microscope is the imaging system. Unlike conventional ultracold-atoms experiments, the imaging system needs to be capable of resolving single-atoms in the optical lattice with single lattice-site resolution. For this experiment, an optical lattice created with a laser wavelength of  $\lambda_{\text{lat}} = 1064 \text{ nm}$  is employed yielding a lattice spacing of  $a = 532 \text{ nm}$ .

The realization of such an imaging system is especially challenging since the atoms are trapped in an ultra-high vacuum (UHV) chamber with pressures on the order of  $p = 10^{-11} \text{ mbar}$  requiring thick steel and glass walls. For optical viewports a thickness of 5 mm is considered sufficient to avoid bending of the glass due to the pressure difference. As a consequence, the whole imaging system, which needs to be attached to the system outside of the vacuum chamber, needs to feature a long working distance.

As described in chapter 4, re-entrant viewports are used to accommodate the imaging system very close to the atoms. In the next sections the novel imaging system built for this experiment is explained in detail and some preliminary tests of the imaging systems are presented.

Another requirement of the imaging system besides a sufficient optical resolution is the detection efficiency. Although good CCD cameras can nowadays provide detection efficiencies of over 90% at the imaging wavelengths<sup>1</sup>, several tens of photons need to be collected to get a good signal-to-noise ratio. At the end of the chapter the general idea of the detection scheme based on the approach pursued in the bosonic quantum gas microscopes is presented.

### 7.1 A high numerical aperture imaging system

Since optical resolution is connected to the numerical aperture (NA) of the imaging system via the Rayleigh criterion for the minimum distance between resolvable points [131]

$$r = \frac{1.22\lambda}{2n \sin \theta} = \frac{0.61\lambda}{\text{NA}}, \quad (7.1)$$

a high-resolution imaging system requires a lens or an objective with a high numerical aperture.

Long-working distance microscopy objectives are commercially available and essentially satisfy the requirements, namely a long working distance **and** a high numerical aperture. Unlike for the bosonic quantum gas microscopes ([132] and [133]), a commercially available microscope objective instead of a custom-designed one is used. The commercial microscope objective **EO M Plan HR Infinity-Corrected Objective 20x** by Edmund Optics is much cheaper than any

---

<sup>1</sup>The imaging wavelengths in this experiment correspond to the  $D_2$ -transitions of the different species, which are given in figure 4.1.

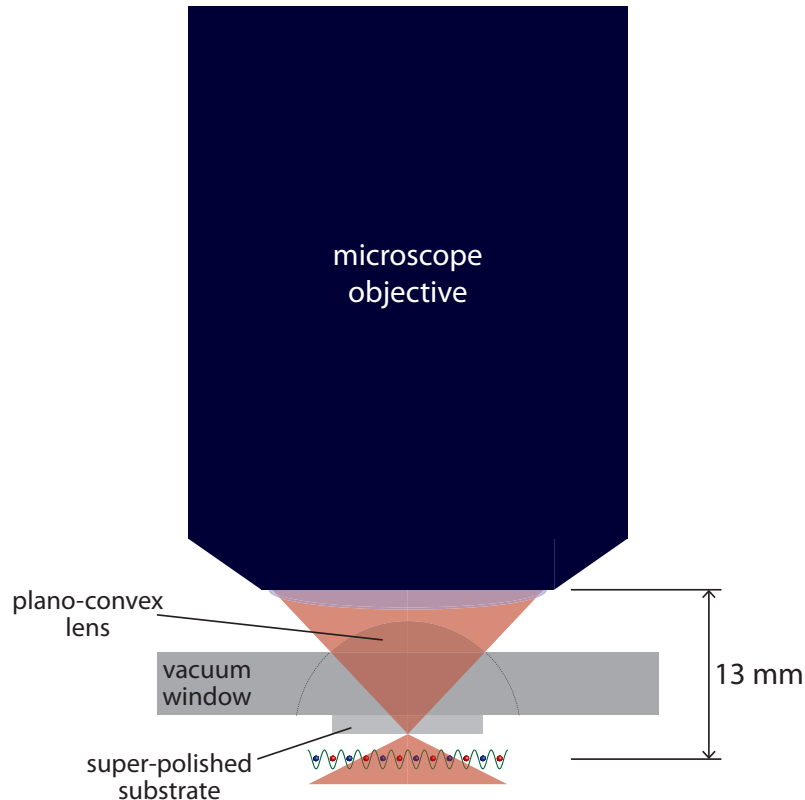


Figure 7.1: Enhancement of the numerical aperture with a hemispherical lens attached to the vacuum window. Below the vacuum window a super-polished substrate is optically contacted to reduce surface scattering.

custom-designed objective but also features a numerical aperture of  $NA = 0.6$  at a working distance of  $d_{\text{work}} = 13$  mm. Furthermore, there is no lead time on this objective.

However, the numerical aperture is still not sufficient to resolve single-lattice sites with a spacing on the order of  $r \approx 500 - 600$  nm. A smart combination of a custom-made plano-convex lens that is almost hemispheric and the vacuum window allows the enhancement of the numerical aperture which is shown in figure 7.1: The hemispheric lens (CAD drawing in section A.4) is optically contacted<sup>2</sup> to the vacuum window making up a complete half-sphere and allows imaging the atoms within the working distance of the microscope objective.

Below the vacuum window, a super-polished fused silica substrate of thickness  $d = 1.8$  mm is optically contacted to reduce the scattering from the surface. Since this surface is very close to the atoms located only a few micrometer away from the vacuum window, especially Rayleigh

---

<sup>2</sup>Optical contact bonding is a method to join two optical elements with conformal surfaces without any glue. The two pieces are just held together by the intermolecular forces like the van-der-Waals force.

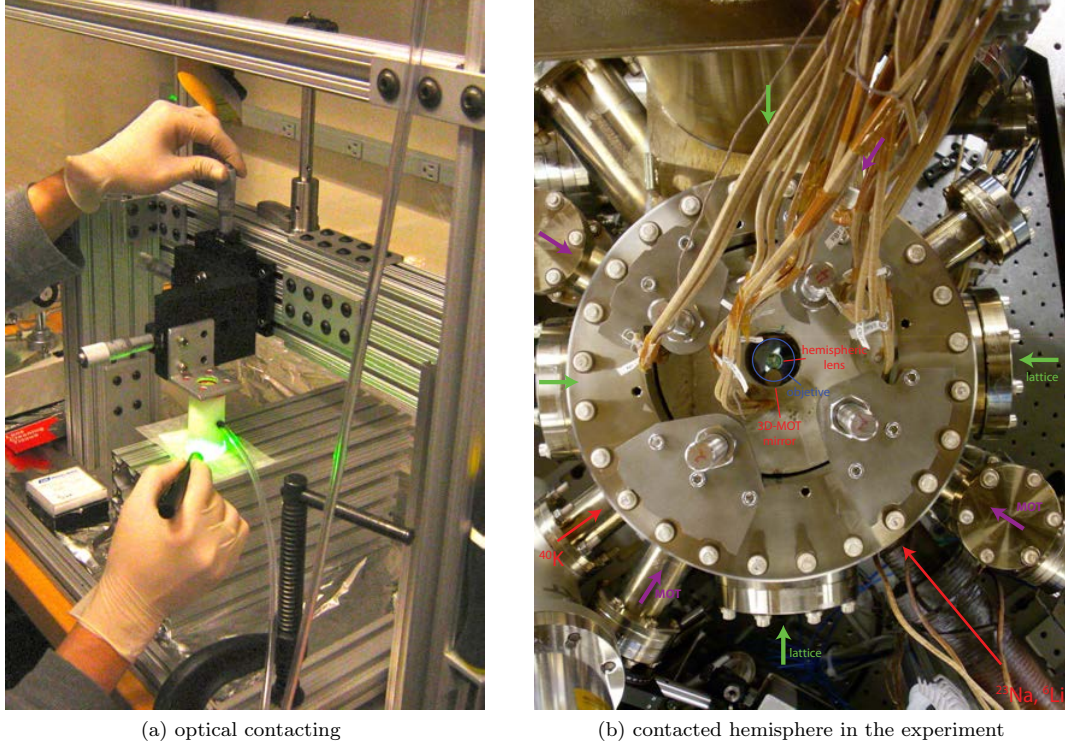


Figure 7.2: The hemisphere has been contacted to the viewport using a small vacuum pump mounted on three-dimensional translation stage as shown in (a). On the right the hemispheric lens and the little mirror for reflecting a 3D-MOT beam are visible in the readily assembled system (b).

scattering of a glass surface with standard optical quality would make any single-site resolved detection impossible. The super-polished substrate used here was manufactured by *ATFilms Inc.*, features a mean surface roughness of only  $\langle \Delta d \rangle_{\text{rms}} \approx 1 \cdot 10^{-10} \text{ m}$  and is coated with an anti-reflective-coating optimized for the imaging wavelengths  $\lambda = 589 \text{ nm}, 671 \text{ nm}, 767 \text{ nm}$  at normal incidence and with a high-reflectivity coating at the lattice laser wavelength  $\lambda_{\text{latt}} = 1064 \text{ nm}$  at normal and at  $10^\circ$  incidence (for creating a lattice with a larger lattice spacing, see section 7.3). A stress-compensation coating on the second side of the super-polished substrate compensates for thermal stress during the IBS coating process. A part of the spectrum of these two coatings has been characterized by the manufacturer, see figure A.2 in the appendix.

Since the imaging beam hits the hemispheric lens at normal incidence, no refraction occurs at the air-glass surface<sup>3</sup>. But at the lower glass-vacuum interface refraction occurs and the numerical aperture is enhanced by a factor given by the refractive index of the lens material fused silica,  $n_{\text{FS}} \approx 1.46$  (symbolized by the light-red-colored imaging beam in figure 7.1).

---

<sup>3</sup>The material of the hemispheric lens and the vacuum window is fused silica.

The optical contacting of the hemispheric lens, the vacuum window and the super-polished substrate requires all connecting surfaces to be very flat. For both the super-polished substrate and the hemispheric lens this is already the case since these elements are small and the fabrication process already features very good flatness (deviations less than  $\frac{\lambda}{50}$  and less than  $\frac{\lambda}{10}$  across the whole surface, respectively, for the imaging wavelength  $\lambda = 767$  nm). However, the vacuum windows needed to be processed further since they have been put into the re-entrant viewports by a diffusion-bonding process which is carried out at high temperatures and high pressures causing deformations of the vacuum window.

To improve the flatness of the window after the glass-metal bonding process of the re-entrant viewport, the window<sup>4</sup> has been polished with a special surface treatment technique, MRF polishing<sup>5</sup>, by fineoptix GmbH.

Interferometric measurements in figures A.3a and A.3b show that a good surface flatness of at least  $\frac{\lambda}{8}$  has been achieved in the center of the viewport (again in terms of the atomic imaging wavelength  $\lambda = 767$  nm and not the wavelength in the interferometric measurement).

A home-built clean room environment made with a hyper-filter system allowed to perform the optical contacting with low air pollution to avoid the deposit of dust in-between the two elements to be contacted. Figure 7.2a shows how the precise positioning was realized with a vacuum pump and a three-dimensional translations stage (picture was taken during optical contacting tests). Figure 7.2b shows the hemispheric lens at its final place in the experiment.

## 7.2 Testing the imaging system

Since the imaging system is a crucial part that needs to be built into the experiment from the beginning but can only be tested after all other components work and a cloud of ultracold atoms has been created, a prototype imaging system has been built and tested separately.

### 7.2.1 Microscope objective tests

As a first test, the wavefront distortion by the microscope objective was tested by interferometry. The measured wavefront distortion is shown in 7.3, which is comparable to what was expected for a standard microscopy objective.

The objective needs to be fixed tightly to the chamber and the other components of the imaging system. It is planned<sup>6</sup> to fix the objective with glue to the surrounding ceramics piece of the magnetic coils (visible in figure 7.2b).

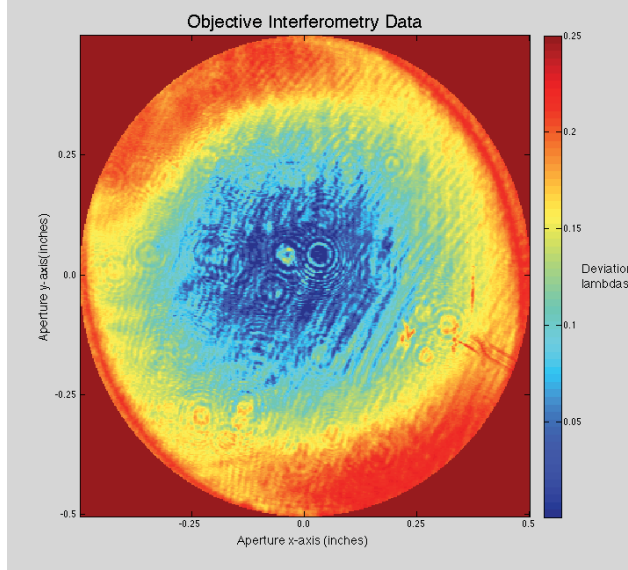


Figure 7.3: Testing the microscope objective with a interferometry setup: The image shows the relative wavefront distortion from the transmission of the objective relative to the imaging wavelength  $\lambda = 766.7017$  nm.

### 7.2.2 Interferometric test setup

In the prototype imaging system the optical contacting of the plano-convex lens and a 5 mm thick glass window (symbolizing the vacuum viewport window) has been tested successfully. To gain insight about the precision of the optical contacting process and the quality of the curved surface of the resulting hemisphere, two interferometric measurements on the both outer surfaces (one surface of the glass window and the curved surface of the hemisphere) have been carried out.

For these measurements a Fizeau interferometer [135] has been constructed<sup>7</sup>. In the first test, the reflection from the curved surface was imaged together with the reflection from the Fizeau plate by a CCD imaging system. When the Fizeau plate was tilted, interference fringes appeared and the relative flatness of the curved surface can be deduced from figure 7.4a.

In this test a movable lens allowed to focus at the desired surface such that the reflection from this surface is interfered with the reflection from the Fizeau plate. By blocking half of the beam

<sup>4</sup>Drawing C.1 in the appendix shows the windows with the surrounding metal wrap, which have the horizontal dimension 10.3 mm.

<sup>5</sup>MRF is short for Magneto-Rheological Finishing [134] and describes a computer-controlled polishing technique for optics where a magnetic fluid with controllable shape and stiffness is used to polish with a very high spatial precision.

<sup>6</sup>At the time of writing the main construction of the experiment has been finished and the hemispheric lens is in place as figure 7.2b shows.

<sup>7</sup>Essentially, in a Fizeau interferometer the reflection of the surface of interest and another reference surface, typically a piece of very flat glass called the Fizeau plate which is placed inside the beam, are overlapped on a beam splitter and the interference is being monitored with a CCD camera system.

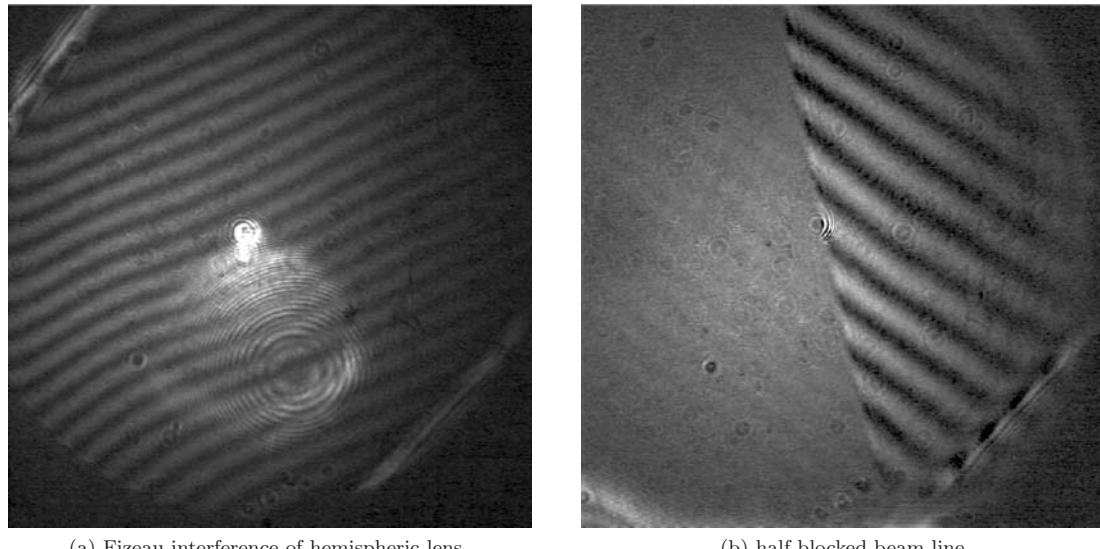


Figure 7.4: Fizeau interferometer images of the curved surface of the hemisphere. On the left side (a) the interference fringes with a reference Fizeau plate are visible, showing wavefront distortions. On the right side one half of the imaging has been blocked to prove that the interference fringes are coming from the curved surface (b).

line one can infer if the curved or the flat surface is viewed in the Fizeau interferometer: Since the light hits the curved surface of the hemisphere perpendicular, it is reflected back in the same direction. When the reflection occurs at the flat surface, blocking half of the beam line would result in a completely vanishing interference pattern since the light is not reflected back in the same direction but in the other blocked half of the beam line.

Hence blocking half of the beam line results in an image where one half of the interference pattern has vanished if the curved surface is imaged. As figure 7.4b shows this is the case and hence the interference fringes originate from the curved surface.

In another test the flat surface was imaged and the interference of this surface and the Fizeau plate observed as figure 7.5a. The interference pattern shows the relative wavefront distortion of the complete imaging system consisting of the objective, the hemispheric lens and the glass window<sup>8</sup>. By tilting the Fizeau plate in both dimensions, it could be aligned coplanar to the flat surface resulting in a vanished interference pattern which is shown in figure 7.5b.

### 7.2.3 Imaging nanospheres

In a third test, fluorescent nano-spheres with a diameter less than 100 nm provided a test object much smaller than the expected optical resolution of the imaging system. This test gives an indication of the diffraction-limit of the imaging system.

---

<sup>8</sup>For the sake of completeness another lens between the microscope objective and the CCD camera providing the optimal magnification on the CCD chip should be mentioned.

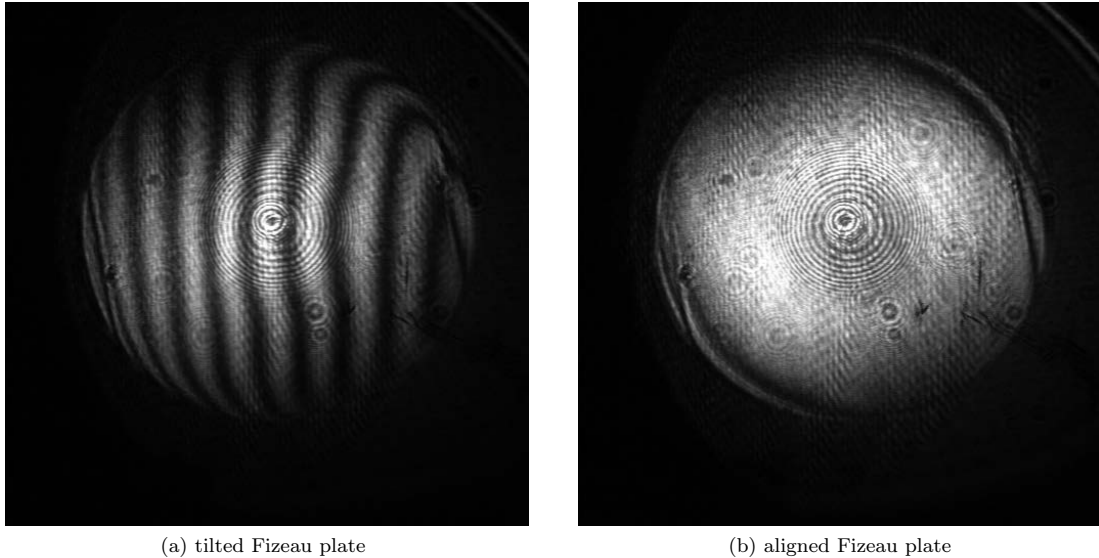


Figure 7.5: Fizeau interference images of the flat surface of the prototype imaging system consisting of a hemispheric lens contacted to a reference flat window with 5 mm thickness. In (a) the Fizeau plate is tilted with respect to the flat surface yielding Fizeau interference fringes, in (b) the Fizeau plate has been aligned coplanar with the reference flat and hence the interference fringes disappear.

The employed nano-spheres are commercially available and have been placed on the flat surface of the glass window. The special type of fluorescent nano-spheres used here can be excited at  $\lambda \approx 532$  nm using a green laser pointer and emit fluorescent light in the range 500 – 650 nm. By using an edge filter all fluorescent light with  $\lambda > 550$  nm was collected by the CCD camera through the imaging system.

Figure 7.6 shows the resulting picture, a numerical fit proved the diffraction-limitation of the objective given by the numerical aperture. Theoretically, the imaging system has a resolution of

$$r_K = \frac{1.22\lambda}{2n_{\text{refr.}} \sin \theta} = \frac{0.61 \cdot 767 \text{ nm}}{0.6 * 1.46} = 534 \text{ mm} \quad (7.2)$$

for the imaging wavelength of potassium and

$$r_K = \frac{1.22\lambda}{2n_{\text{refr.}} \sin \theta} = \frac{0.61 \cdot 671 \text{ nm}}{0.6 * 1.46} = 467 \text{ mm} \quad (7.3)$$

for lithium.

These tests with this prototype experiment show that the imaging system can theoretically image single atoms very close to the flat surface of the glass window (which corresponds to the super-polished substrate in the experiment).



Figure 7.6: Testing with imaging system with fluorescent nano-spheres: By imaging a single nano-sphere ( $\phi < 100$  nm) the diffraction-limited resolution of the microscope objective could be confirmed.

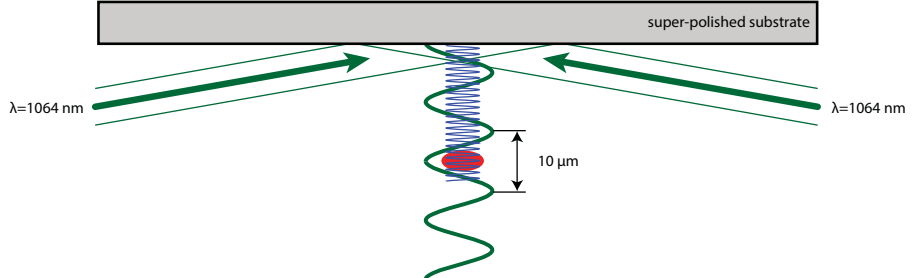


Figure 7.7: A lattice with a lattice constant of  $a \approx 10 \mu\text{m}$  is created by reflecting laser beams with wavelength  $\lambda = 1064 \text{ nm}$  of the surface of the superpolished substrate at a very small angle.

### 7.3 Loading the atoms in the optical lattice

A central idea of a quantum gas microscope is the imaging of exactly one 2D-layer of atoms in a three-dimensional optical lattice. Although the imaging systems can be focused at different working distances (for instance by moving the lens between the microscope objective and the CCD camera that will be added later, not shown in the figures in this chapter), other present layers in the three-dimensional lattice are likely to disturb the imaging with stray light.

To prevent this effect, a procedure to load only one layer of atoms into the optical lattice will

be used and was part of the design process of the vacuum chamber. An important part of this slicing process is to create a lattice with larger spacing of  $a = 10 \mu\text{m}$  by reflecting two lattice laser beams with a wavelength of  $\lambda = 1064 \text{ nm}$  at an angle of roughly  $10^\circ$  off the lower surface of the super-polished substrate as figure 7.7 shows.

The atomic cloud (red in the figure) can then be loaded into one of the wells of this large-spacing lattice. This could be done by loading from a tightly focused optical dipole trap.

Subsequently, the  $\lambda = 1064 \text{ nm}$ -lattice lattice with a lattice spacing of  $b = 532 \text{ nm}$  (blue in the figure), which is created by reflecting a laser beam normal to the surface of the super-polished substrate, is switched on and the atoms can be transferred into this lattice. A magnetic field gradient and selective RF transfer can then be employed to selectively depopulate all but one layer.

## 7.4 Parity imaging

As showed in the beginning of this chapter, a diffraction-limited imaging system has been developed that is improved compared to the imaging systems of the bosonic quantum gas microscopes: the quantum gas microscope at Harvard University [132] uses a hemispherical lens as well to enhance the numerical aperture, but another glass surface of a glass cell providing the vacuum makes it necessary to correct the microscope objective for that glass surface. The other bosonic quantum gas microscope in Munich [2] uses a microscope objective with a much higher numerical aperture resulting a very complicated custom-made design, that also needs to be corrected for the thick vacuum window.

Both approaches are far more expensive and time-consuming to implement than the approach reported in this work, but should yield the same results. So far the experiment described here has been build and the first atoms have been trapped (details on the recent progress will be given in the outlook in chapter 8). Yet, the high-resolution imaging system needs to be brought into operation.

Like for the bosonic quantum gas microscopes, several technical details are necessary to achieve the single-site resolved imaging of single atoms in the created 2D-layer. Light assisted collisions will lead to parity imaging, since every pair of atoms on one lattice site will escape in a light-assisted inelastic two-body collision [136].

Furthermore, for the imaging of the atoms inside the lattice, the lattice will need to be ramped up dramatically (up to  $3000 \cdot E_R$  in [133]) to inhibit any tunneling processes to other lattice sites during the imaging process and to prevent the atoms from escaping the lattice. Optical molasses will need to be used to ensure constant laser cooling while the atoms are imaged and typically up to 100 photons are acquired per lattice site.

The bosonic quantum gas microscopes have pioneered these techniques, which can be easily adapted in a fermionic quantum gas microscope.



---

## 8. Outlook

---

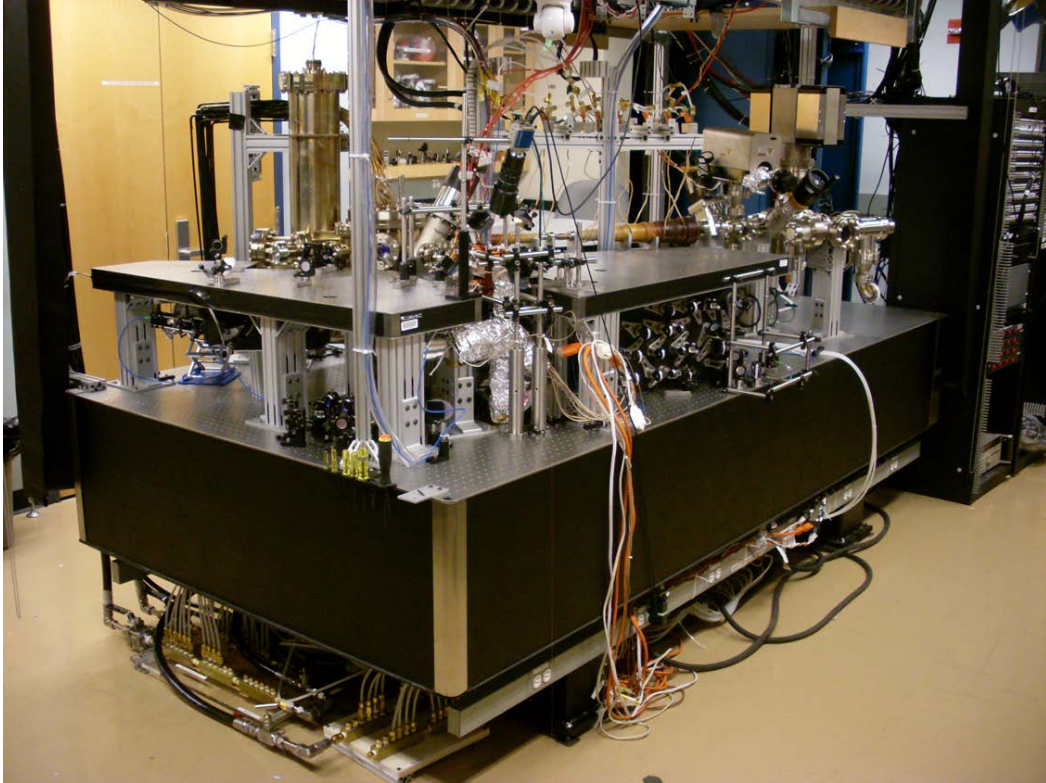


Figure 8.1: The assembled mechanical setup of the experiment. Another optical table accommodates most of the optical setup, which is not shown in this picture.

In this work the concept of a quantum gas microscope has been described. The technology of in-situ imaging of ultracold atoms in an optical lattice is at very early stage: On one hand he bosonic quantum gas microscopes have realized the first pieces of quantum many-body physics like a bosonic Mott insulator [2] and are on a good way of exploring more important phenomena like the recent observation of the 'Higgs' amplitude mode at the two-dimensional superfluid/Mott insulator transition [137] and quantum magnetism [138].

On the other hand, quantum gas microscopes for fermionic species are just now being set up like the experiment described in this work and other experiments around the world.

So far this experiment has been planned, designed and most of the experiment, especially the vacuum system, the magnetic trap, the laser cooling optics and much of the infrastructure needed

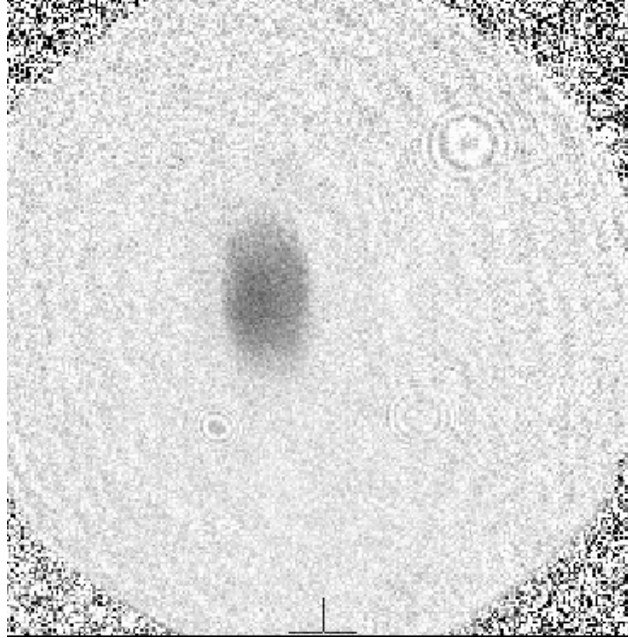


Figure 8.2: Absorption image of  $^{40}\text{K}$  atoms trapped by the magnetic quadrupole coils.

for such an experiment has been built.

Figure 8.1 show the experimental setup with the vacuum system and many peripheral hardware (electronic racks in the background, the water supply and current supply below the table). Not shown here is the optical setup for creating the needed laser frequencies, which is located on another optical table in the same laboratory. Appendix D provides more pictures of the construction process and the readily assembled machine.

Then, the parts of the system have been brought to operation consecutively. Namely, the vacuum systems has been baked and pumped down, the atomic source for  $^{40}\text{K}/^{39}\text{K}$  has been heated and a 2D-MOT of  $^{39}\text{K}$  has been created. Subsequently, the 2D-MOT for  $^{40}\text{K}$  was realized and a 3D-MOT for both potassium species has been observed as shown in figures 5.9a and 5.9b in chapter 5.

At the time of writing the most recent result is that  $^{40}\text{K}$  atoms have been loaded into the magnetic quadrupole coils, one part of the magnetic trap. Figure 8.2 shows an absorption image of the trapped atoms.

As a next step, the two other species  $^6\text{Li}$  and  $^{23}\text{Na}$  need to be added by bringing the double-species Zeeman slower to operation and join all species in the 3D-MOT. Afterwards, the atoms can be cooled down to quantum degeneracy as described in chapter 6. Finally, the optical lattice and the imaging system needs to be completed.

Once the imaging of single atoms in the optical lattice is achieved, one can proceed with the detection of the first fermionic phases in the optical lattice. A proof-of-principle experiment could be the in-situ imaging of a fermionic Mott insulator. Later, one can start studying interesting many-body phenomena that have not been observed so far like the antiferromagnetic phase.

This experiment is also designed to provide many future options. The implementation of two fermionic species and one bosonic species opens many possibilities in the future, like the study of various Bose-Fermi mixtures [43] and heteronuclear polar molecules [139] in optical lattices.

In summary one can say that the technological development of a fermionic quantum gas microscope is at a very early stage with a very good perspective. Quantum gas microscopes for bosonic and fermionic atoms are important milestones on the way to a better understanding of quantum many-body physics.



---

## A. Technical Data

---

### A.1 IBS coating of the main chamber viewports and hemisphere

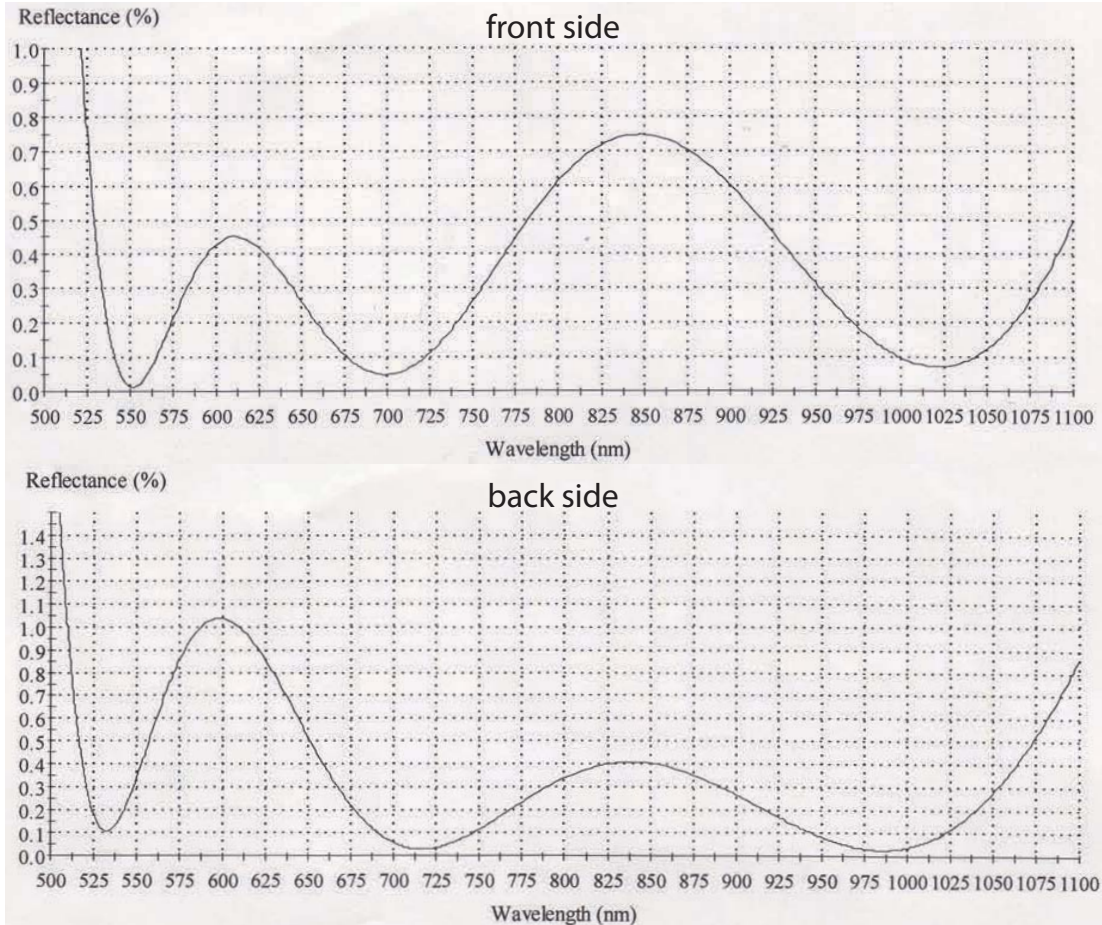


Figure A.1: Both the hemispherical lens of the imaging systems and all the main chamber viewports except the re-entrant viewports are coated with an IBS coating suitable for the  $D_2$  lines of  $^{23}\text{Na}$ ,  $^6\text{Li}$  and  $^{40}\text{K}$  as well as  $\lambda_{\text{lat}} = 1064 \text{ nm}$  for the optical lattice.

## A.2 IBS coating of the super-polished substrate

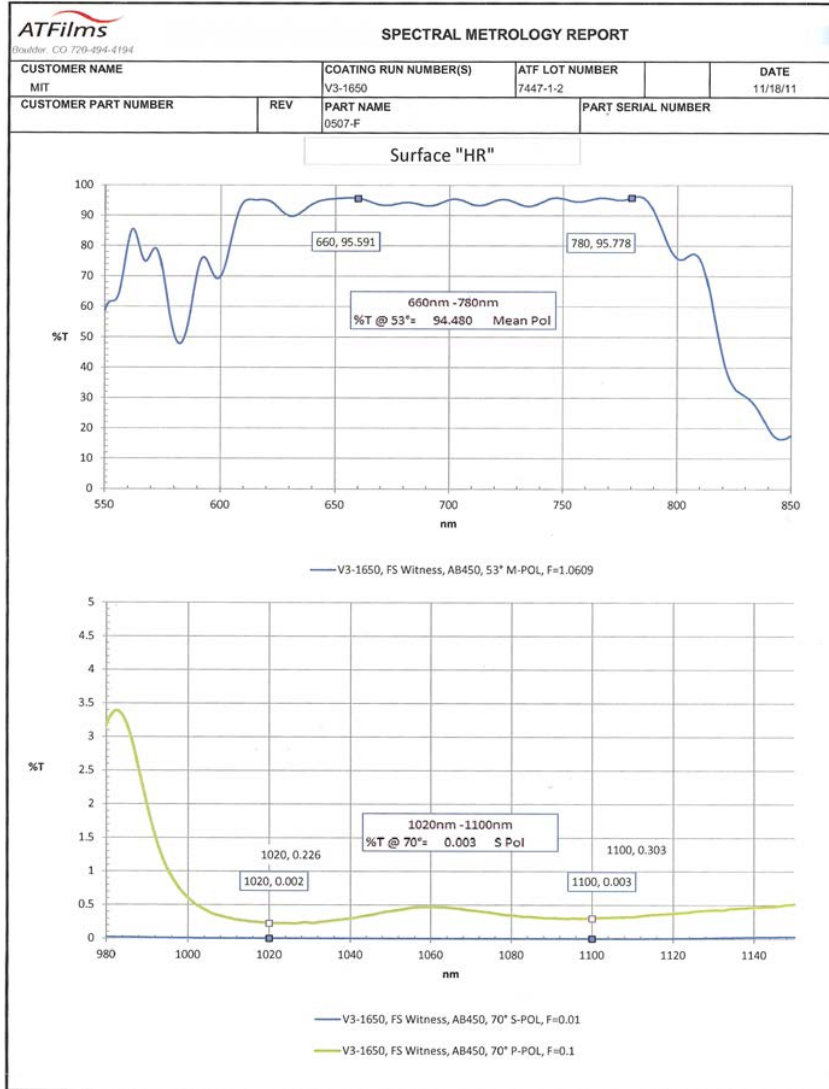
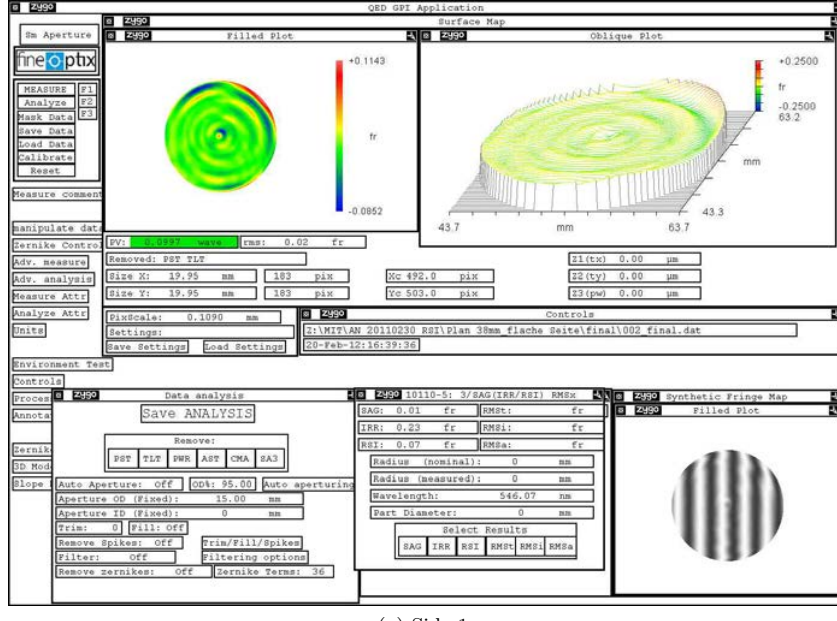
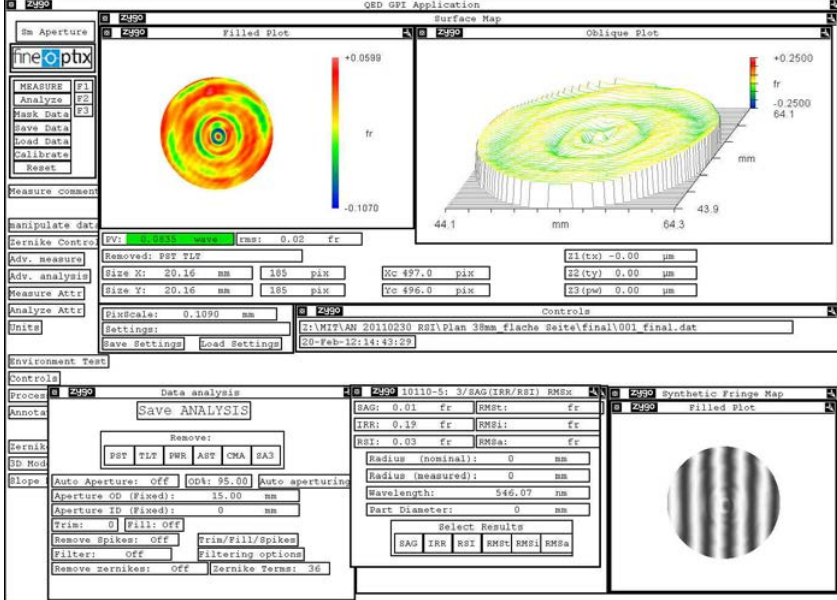


Figure A.2: Coating of the surfaces of the super-polished substrate. One surface is coated with highly reflective (labeled HR) coating, the other side with anti-reflection coating to compensate for stress during the coating process and avoid reflection at this surface.

**A.3 Interferometric measurement of DN200CF re-entrant viewport  
windows after the MRF-polishing process**



(a) Side 1



(b) Side 2

Figure A.3: Interferometric measurement of the wavefront distortion (reflection of the surface) of the two sides of the re-entrant viewport that is part of the imaging system (see chapter 7). Deviations are given in terms of the interferometer wavelength  $\lambda_{\text{inf}} = 546.07 \text{ nm}$ .

## A.4 Hemispheric lens for the imaging system

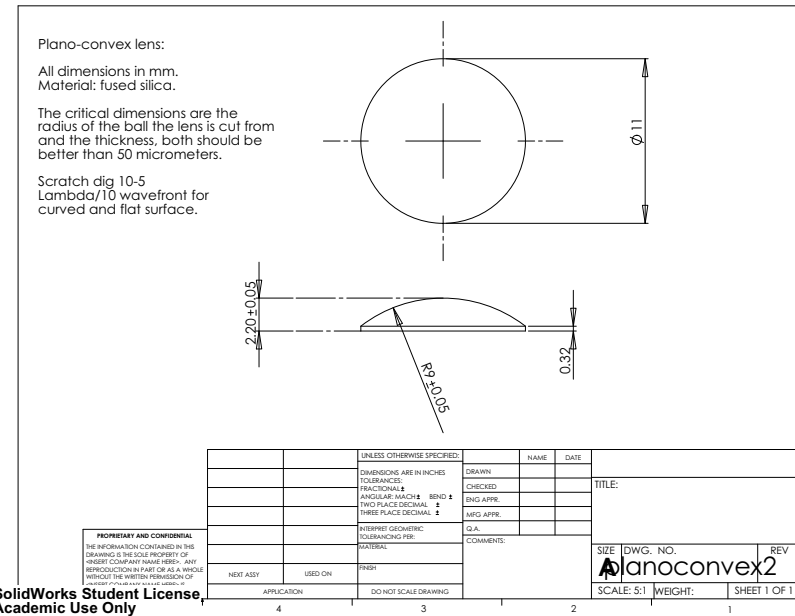


Figure A.4: Drawing of the planoconvex lens used as hemispheric lens in combination with the re-entrant viewport window as shown in figure 7.1.



---

## B. CAD drawings of the main chamber

---

On the following pages the CAD drawings for the main vacuum chamber are presented. Based on these drawings it was constructed by

Sharon Vacuum Inc.  
69 Falmouth Avenue  
Brockton, MA 02301  
<http://www.sharonvacuum.com> .

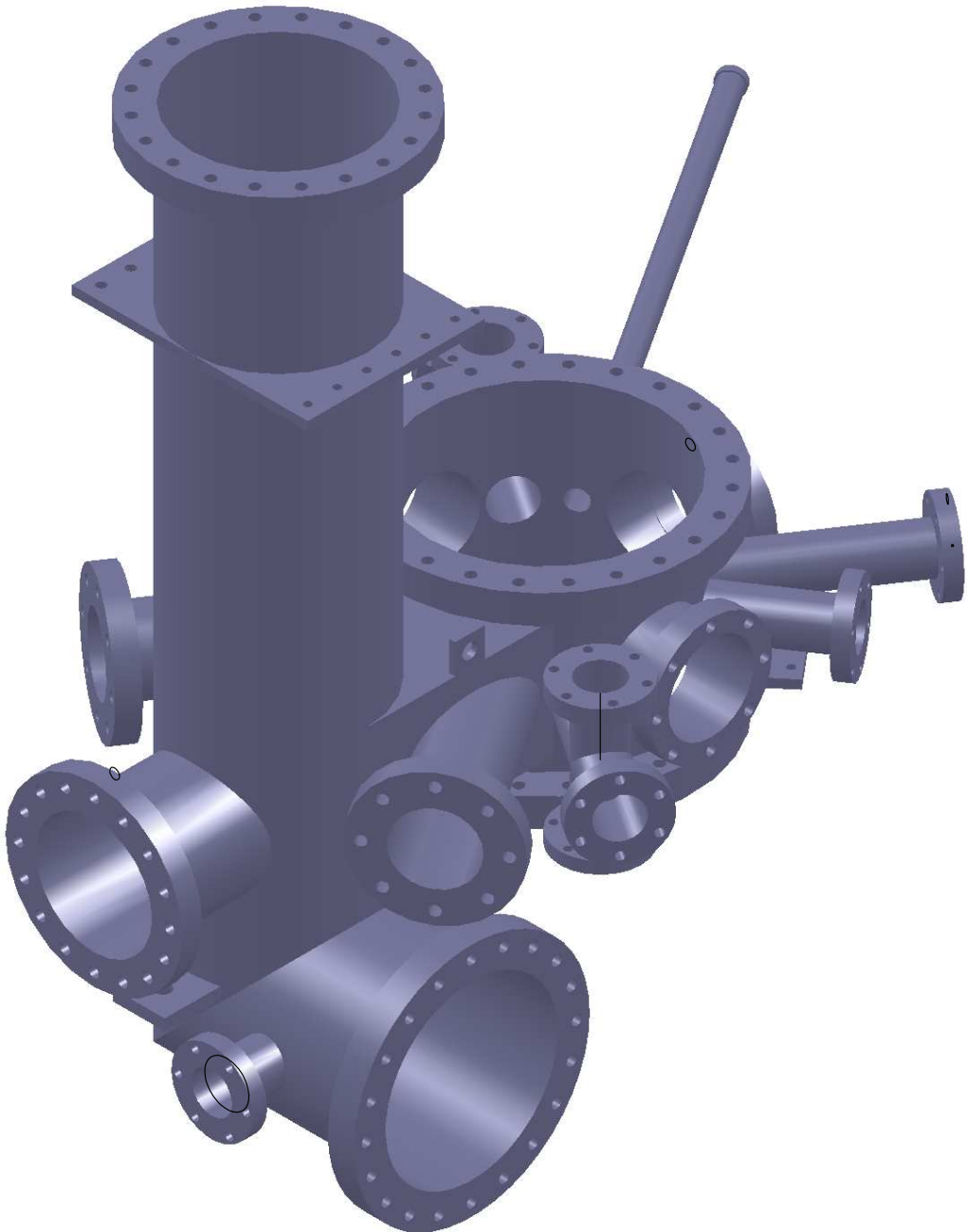
Vacuum chamber for Prof. Martin Zwierlein

Contact:

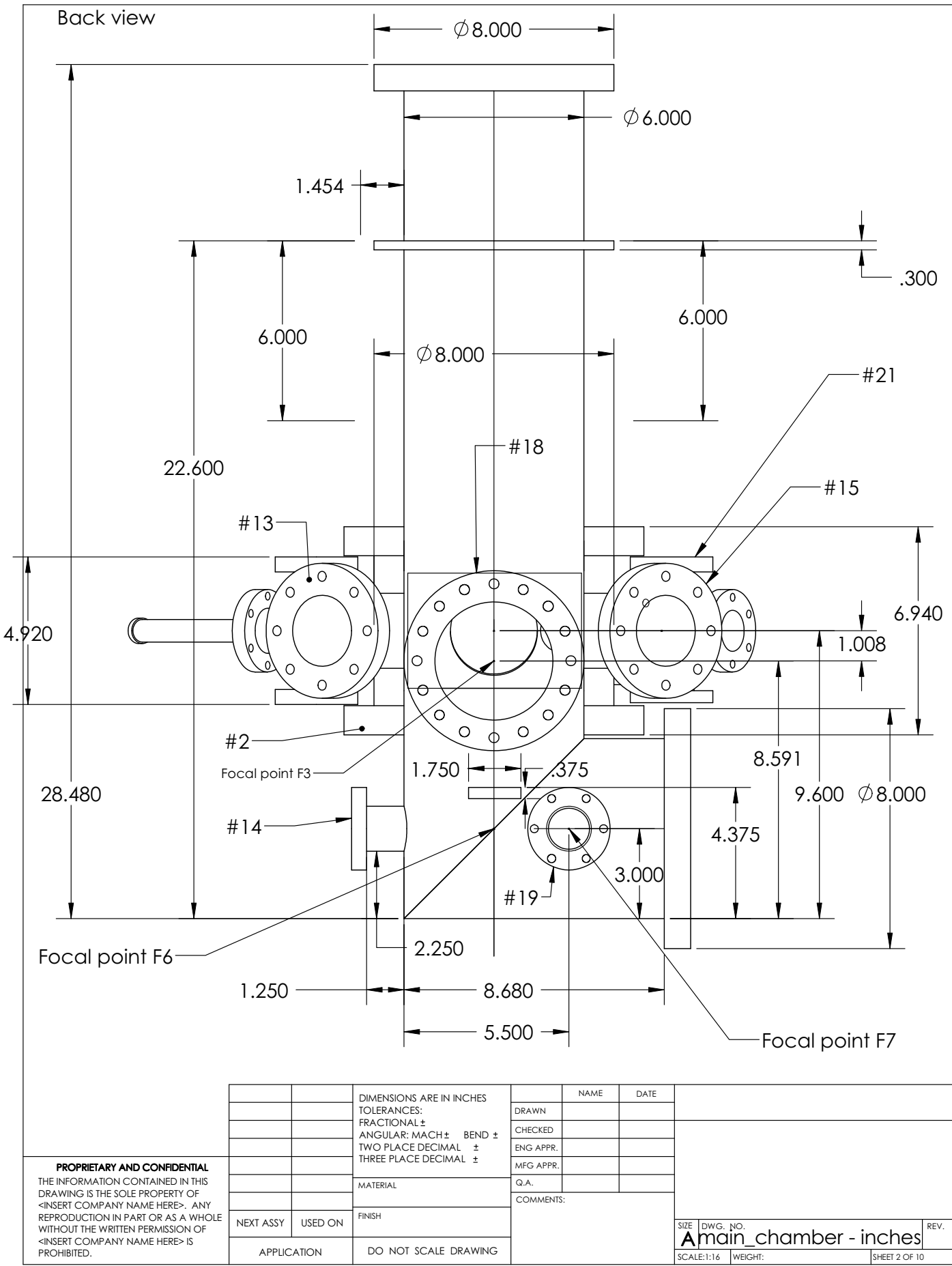
Thomas Gersdorf

gersdorf@mit.edu

617-324-0500



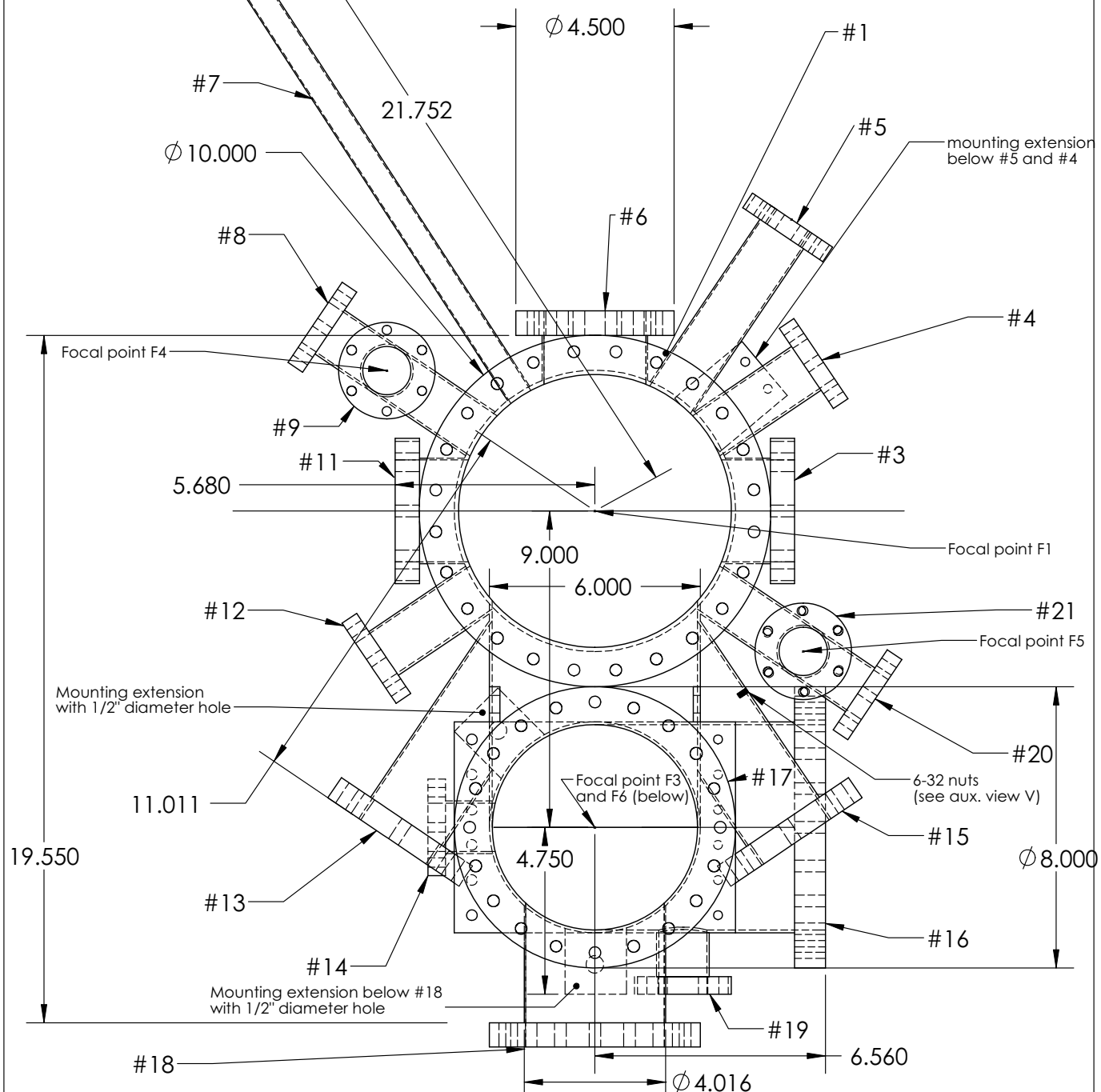
		DIMENSIONS ARE IN INCHES			NAME	DATE		
		TOLERANCES: FRACTIONAL $\pm$ ANGULAR: MACH $\pm$ BEND $\pm$ TWO PLACE DECIMAL $\pm$ THREE PLACE DECIMAL $\pm$		DRAWN				
				CHECKED				
				ENG APPR.				
				MFG APPR.				
				Q.A.				
				COMMENTS:				
<b>PROPRIETARY AND CONFIDENTIAL</b> THE INFORMATION CONTAINED IN THIS DRAWING IS THE SOLE PROPERTY OF <INSERT COMPANY NAME HERE>. ANY REPRODUCTION IN PART OR AS A WHOLE WITHOUT THE WRITTEN PERMISSION OF <INSERT COMPANY NAME HERE> IS PROHIBITED.		NEXT ASSY		USED ON		FINISH		SIZE DWG. NO. REV.
								<b>Amain_chamber - inches</b>
		APPLICATION		DO NOT SCALE DRAWING		SCALE:1:16 WEIGHT: SHEET 1 OF 10		



### Top view

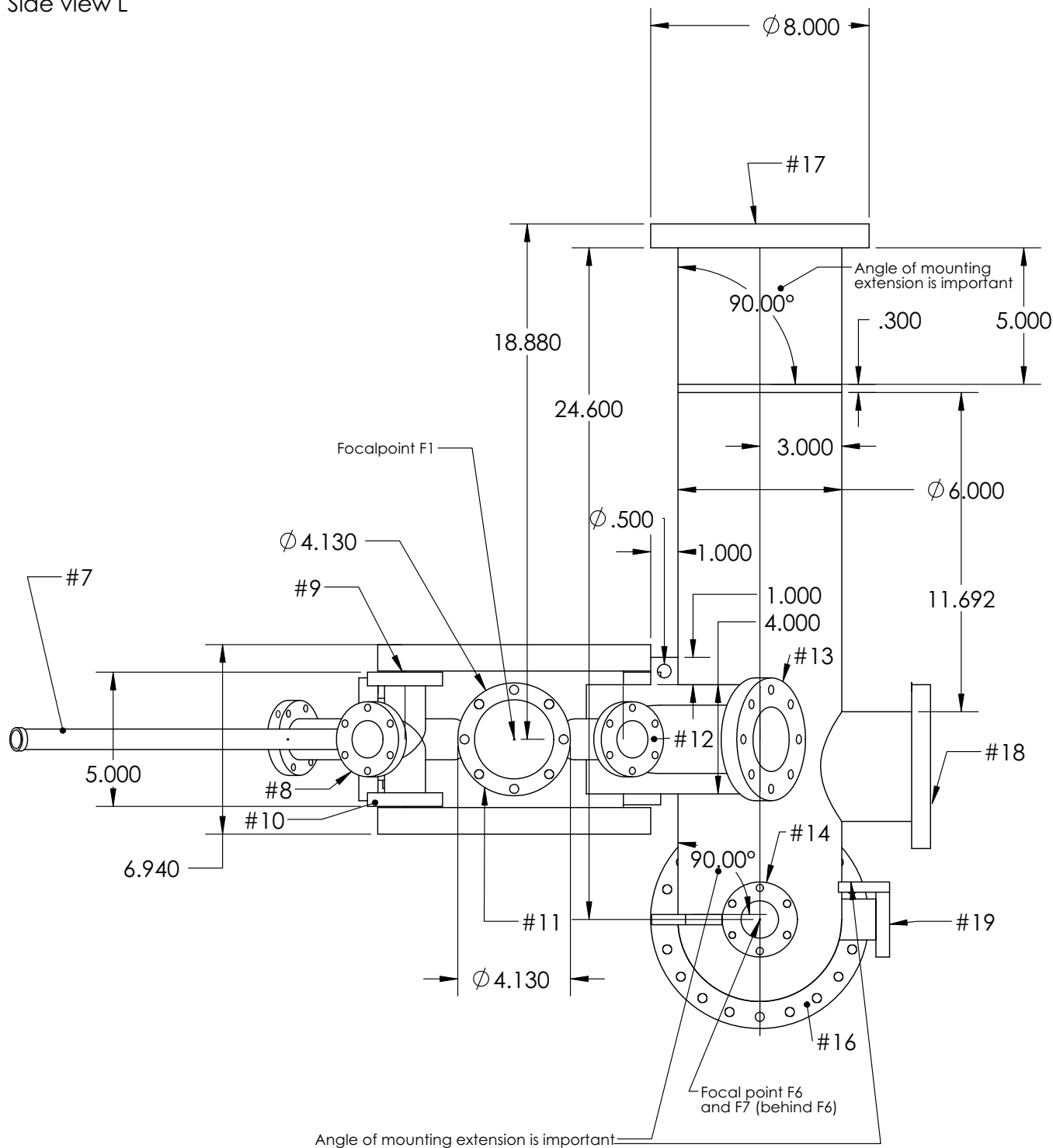
omit retaining  
ring (!!)

#4 and #7: azimuthal angle  
is very important!



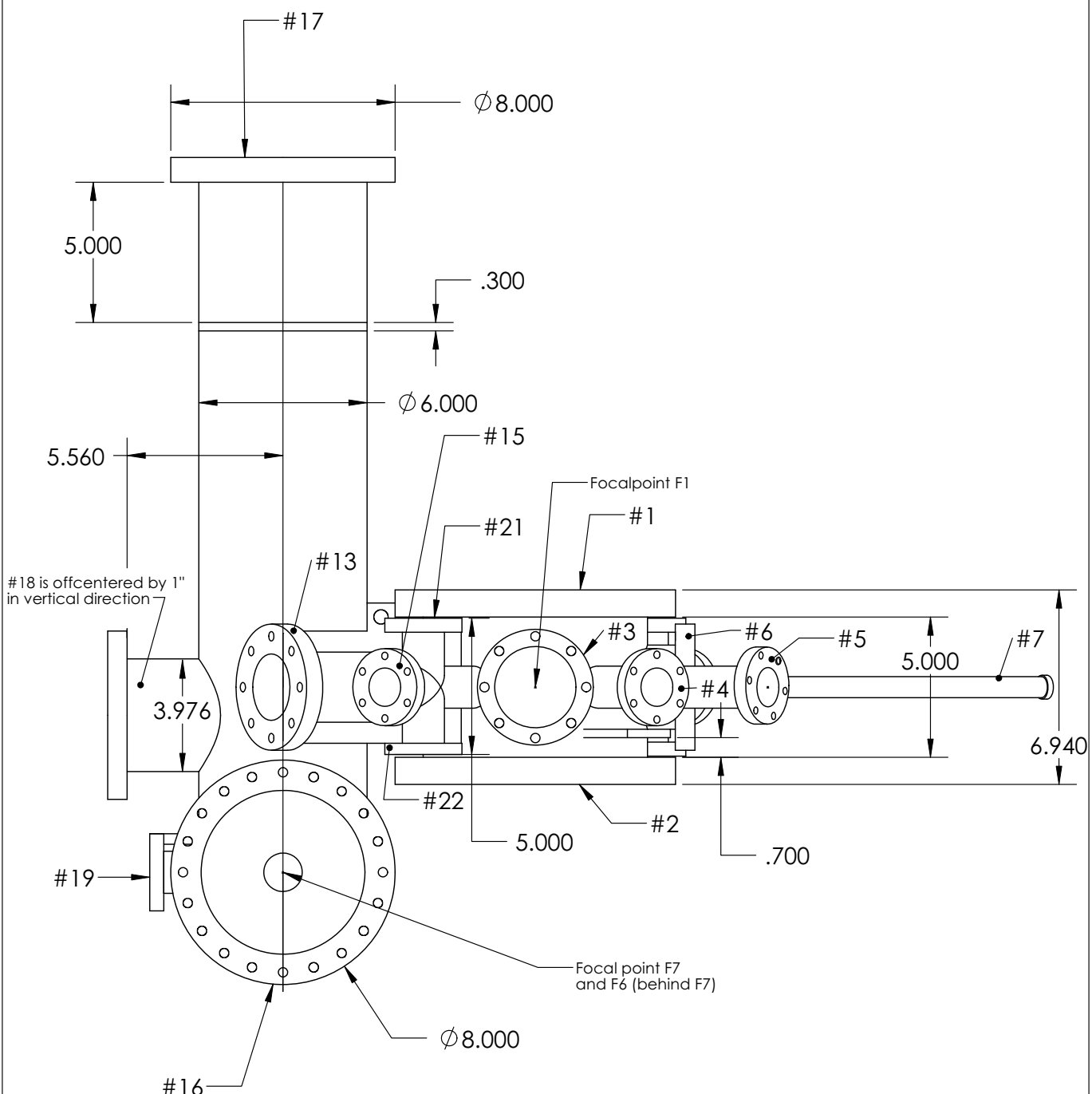
		DIMENSIONS ARE IN INCHES TOLERANCES: FRACTIONAL ± ANGULAR: MACH ± BEND ± TWO PLACE DECIMAL ± THREE PLACE DECIMAL ±		NAME	DATE			
			DRAWN					
			CHECKED					
			ENG APPR.					
			MFG APPR.					
			Q.A.					
			COMMENTS:					
NEXT ASSY	USED ON	FINISH			SIZE	DWG. NO. <b>Amain_chamber - inches</b>		REV.
APPLICATION		DO NOT SCALE DRAWING			SCALE:1:16	WEIGHT:	SHEET 3 OF 10	

Side view L



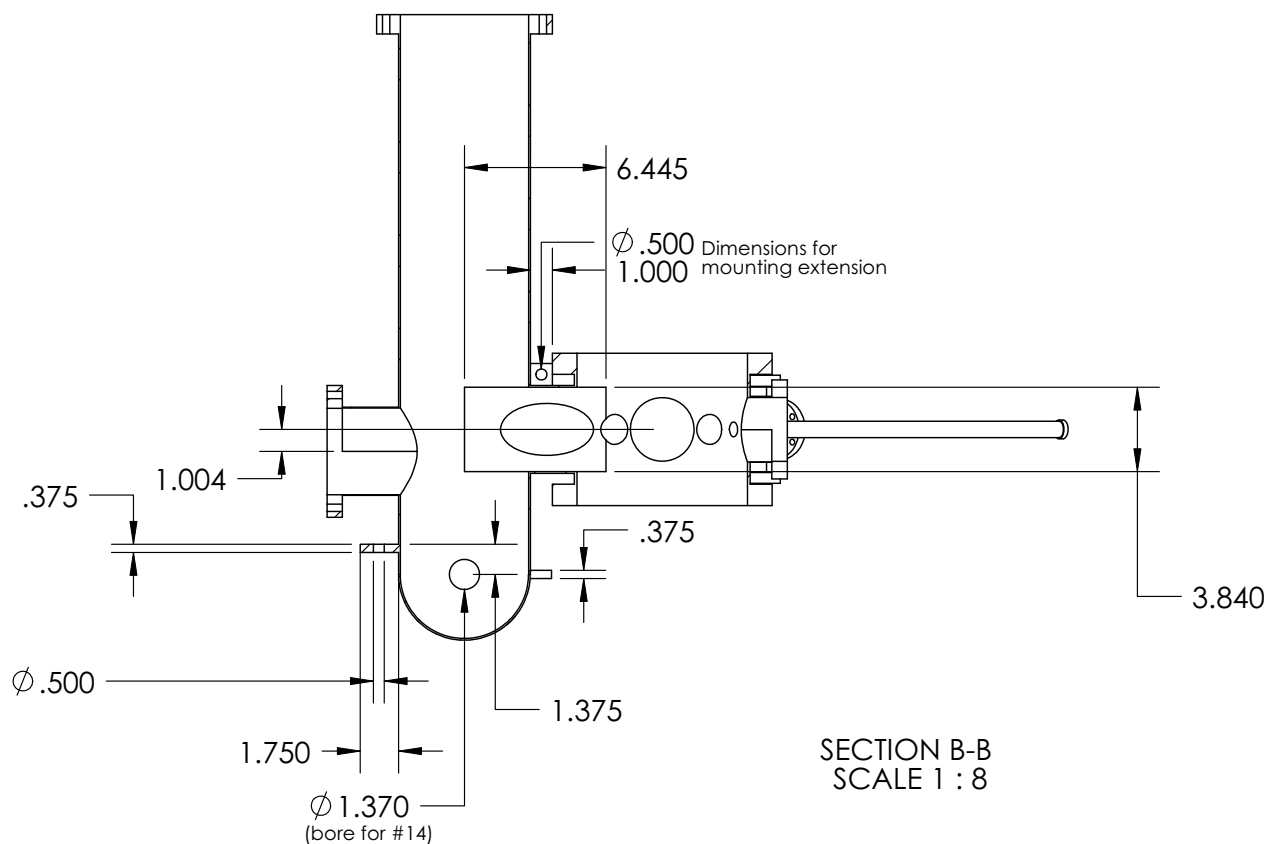
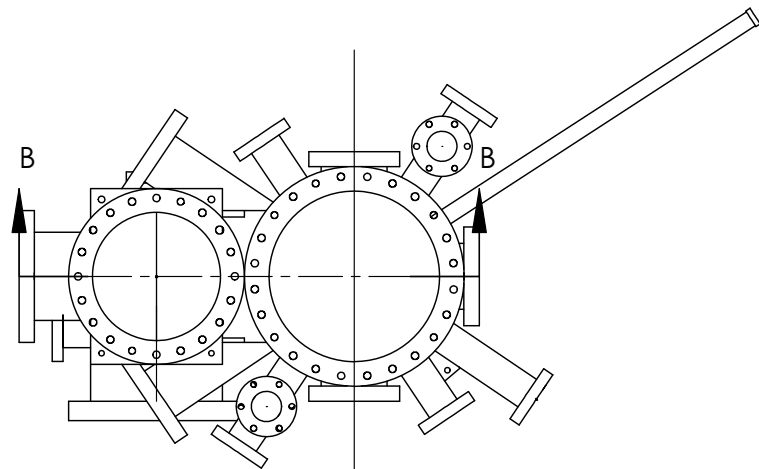
		DIMENSIONS ARE IN INCHES TOLERANCES: FRACTIONAL ± ANGULAR: MACH ± BEND ± TWO PLACE DECIMAL ± THREE PLACE DECIMAL ±			NAME	DATE	
				DRAWN			
				CHECKED			
				ENG APPR.			
				MFG APPR.			
				Q.A.			
				COMMENTS:			
PROPRIETARY AND CONFIDENTIAL  THE INFORMATION CONTAINED IN THIS DRAWING IS THE SOLE PROPERTY OF <INSERT COMPANY NAME HERE>. ANY REPRODUCTION IN PART OR AS A WHOLE WITHOUT THE WRITTEN PERMISSION OF <INSERT COMPANY NAME HERE> IS PROHIBITED.	NEXT ASSY	USED ON	MATERIAL				
			FINISH				
APPLICATION			DO NOT SCALE DRAWING				
SIZE DWG. NO. <b>Amain_chamber - inches</b> REV.:							
SCALE:1:16				WEIGHT:			SHEET 4 OF 10

Side view R



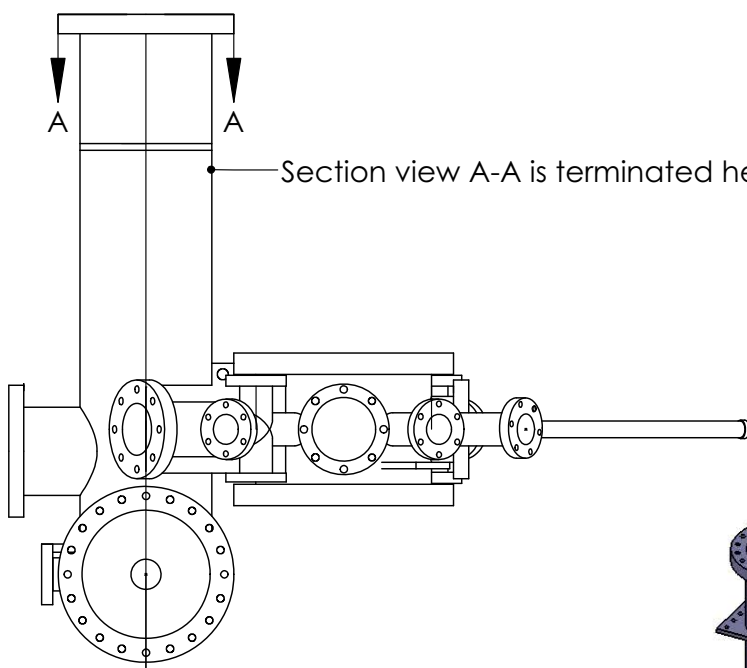
		DIMENSIONS ARE IN INCHES		COMMENTS:	DWG. NO. <b>Amain_chamber - inches</b> REV.		
		TOLERANCES: FRACTIONAL $\pm$ ANGULAR: MACH $\pm$ BEND $\pm$ TWO PLACE DECIMAL $\pm$ THREE PLACE DECIMAL $\pm$					
		MATERIAL					
NEXT ASSY	USED ON	FINISH					
APPLICATION		DO NOT SCALE DRAWING					
SCALE:1:16	WEIGHT:						
<b>PROPRIETARY AND CONFIDENTIAL</b> THE INFORMATION CONTAINED IN THIS DRAWING IS THE SOLE PROPERTY OF <INSERT COMPANY NAME HERE>. ANY REPRODUCTION IN PART OR AS A WHOLE WITHOUT THE WRITTEN PERMISSION OF <INSERT COMPANY NAME HERE> IS PROHIBITED.							

## Auxiliary view I

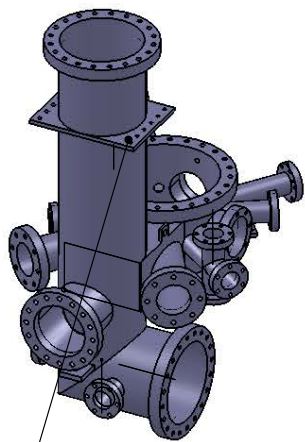
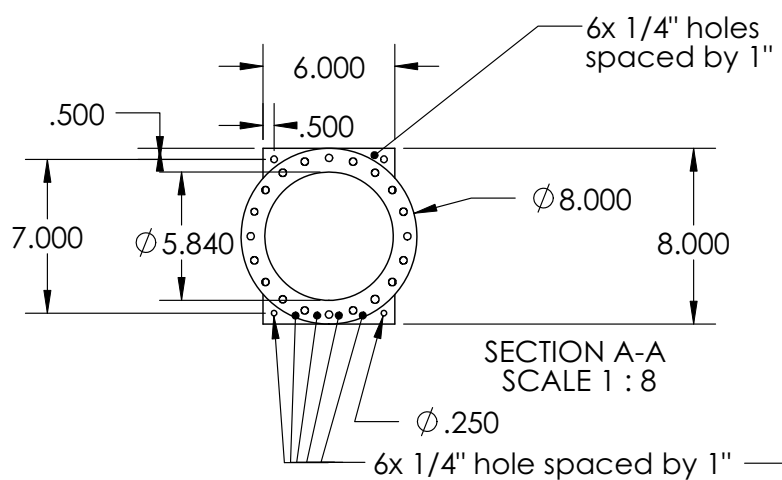


<b>PROPRIETARY AND CONFIDENTIAL</b> THE INFORMATION CONTAINED IN THIS DRAWING IS THE SOLE PROPERTY OF <INSERT COMPANY NAME HERE>. ANY REPRODUCTION IN PART OR AS A WHOLE WITHOUT THE WRITTEN PERMISSION OF <INSERT COMPANY NAME HERE> IS PROHIBITED.			DIMENSIONS ARE IN INCHES		DRAWN CHECKED ENG APPR. MFG APPR. Q.A. COMMENTS:	NAME      DATE <hr/> <hr/> <hr/> <hr/> <hr/> <hr/> <hr/> <hr/> <hr/> <hr/>	
			TOLERANCES:				
			FRACTIONAL $\pm$				
			ANGULAR: MACH $\pm$ BEND $\pm$				
			TWO PLACE DECIMAL $\pm$				
			THREE PLACE DECIMAL $\pm$				
			MATERIAL				
	NEXT ASSY	USED ON	FINISH				
	APPLICATION		DO NOT SCALE DRAWING				
				SIZE DWG. NO.		REV.	
				<b>Amain_chamber - inches</b>			
				SCALE:1:12 WEIGHT:		SCALE 6 OF 10	

## Auxiliary view II

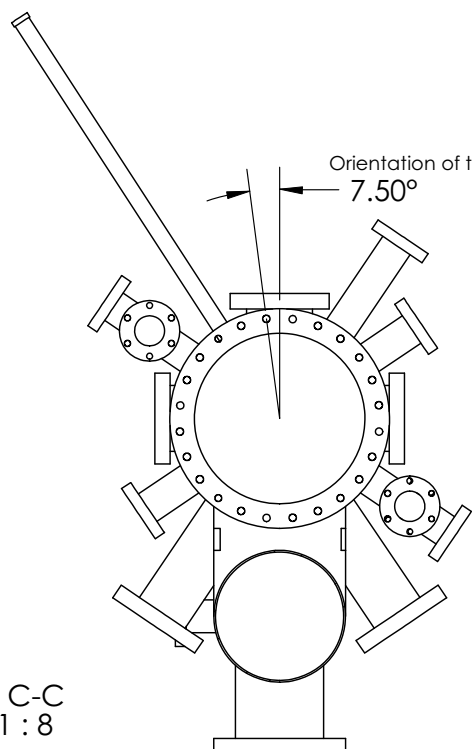
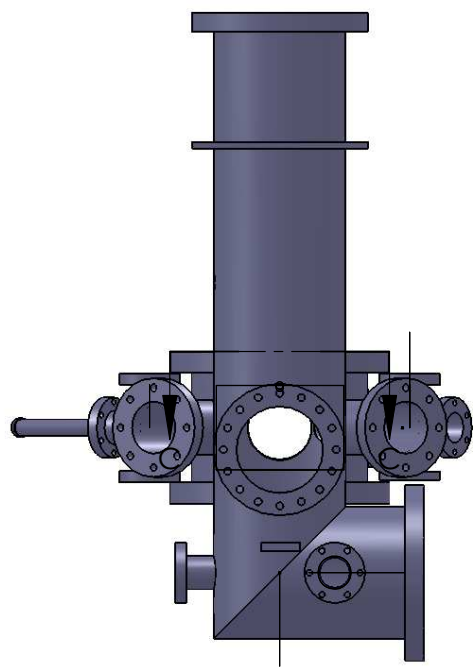


—Section view A-A is terminated here



		DIMENSIONS ARE IN INCHES TOLERANCES: FRACTIONAL ± ANGULAR: MACH ± BEND ± TWO PLACE DECIMAL ± THREE PLACE DECIMAL ±			NAME	DATE					
		MATERIAL		DRAWN							
				CHECKED							
		ENG APPR.		COMMENTS:							
		MFG APPR.									
		Q.A.									
NEXT ASSY		USED ON	FINISH							SIZE	DWG. NO.
APPLICATION				DO NOT SCALE DRAWING					Amain_chamber - inches		
									SCALE:1:12	WEIGHT:	SHEET 7 OF 10

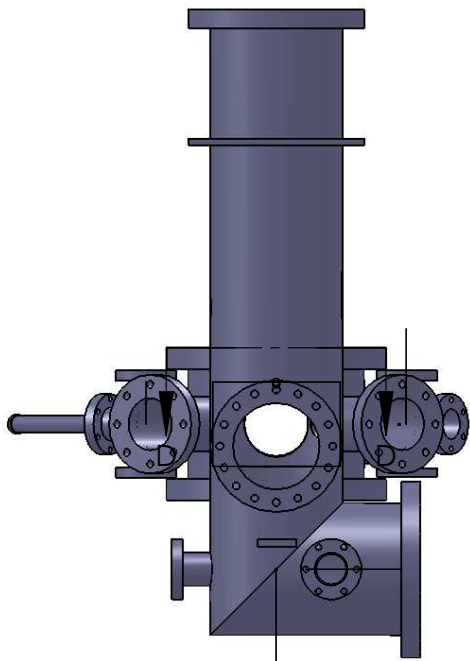
Auxiliary view III



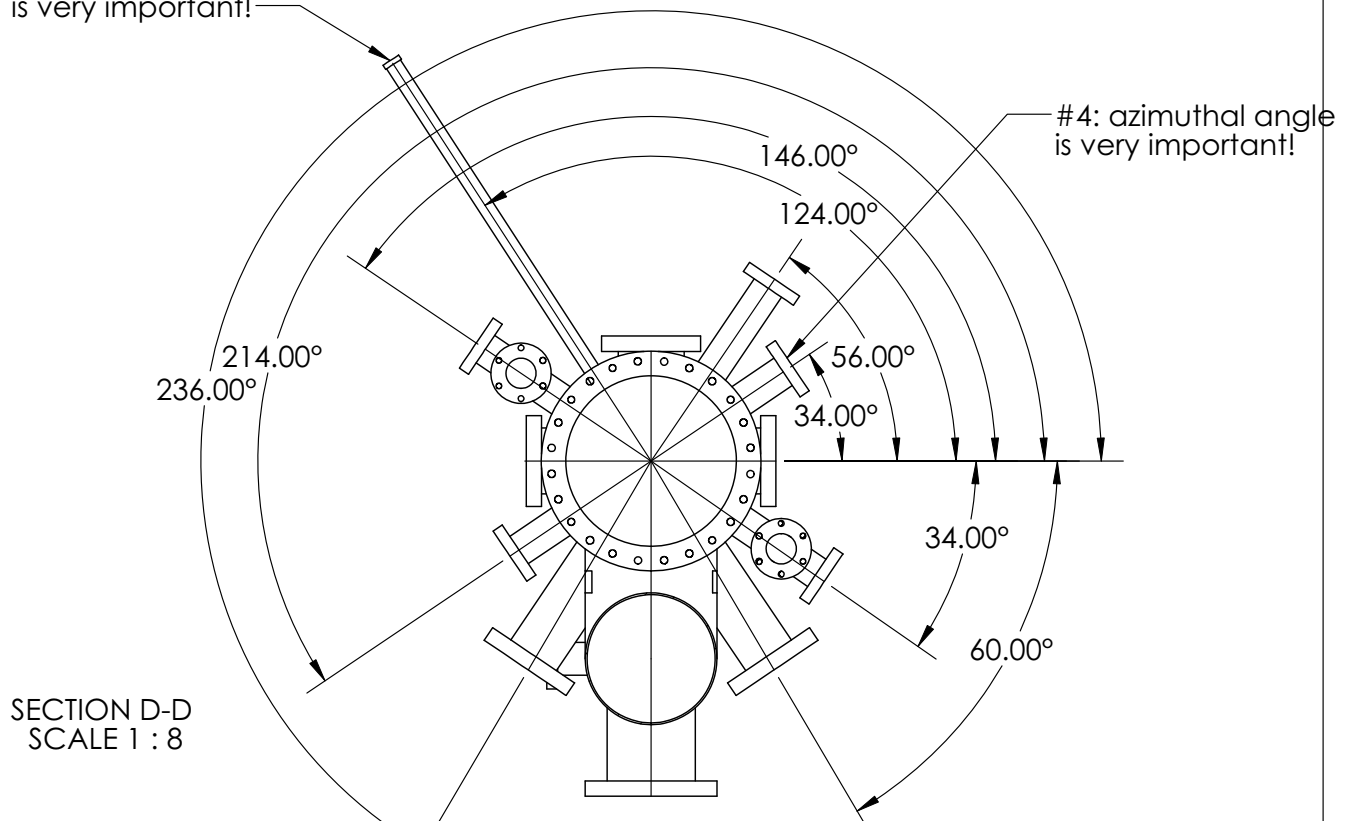
SECTION C-C  
SCALE 1 : 8

		DIMENSIONS ARE IN INCHES TOLERANCES: FRACTIONAL $\pm$ ANGULAR: MACH $\pm$ BEND $\pm$ TWO PLACE DECIMAL $\pm$ THREE PLACE DECIMAL $\pm$	DRAWN	NAME	DATE			
			CHECKED					
			ENG APPR.					
			MFG APPR.					
			Q.A.					
			COMMENTS:					
PROPRIETARY AND CONFIDENTIAL THE INFORMATION CONTAINED IN THIS DRAWING IS THE SOLE PROPERTY OF <INSERT COMPANY NAME HERE>. ANY REPRODUCTION IN PART OR AS A WHOLE WITHOUT THE WRITTEN PERMISSION OF <INSERT COMPANY NAME HERE> IS PROHIBITED.			SIZE DWG. NO. REV. <b>Amain_chamber - inches</b>					
NEXT ASSY	USED ON	FINISH			SCALE:1:12 WEIGHT: SHEET 8 OF 10			
APPLICATION		DO NOT SCALE DRAWING						

Auxiliary view IV

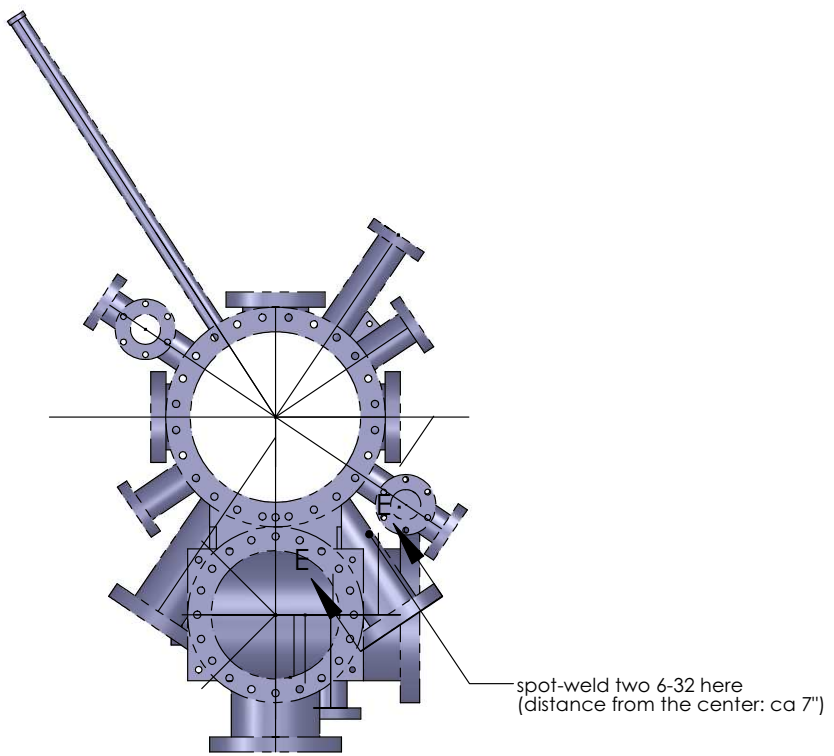


#7: azimuthal angle  
is very important!



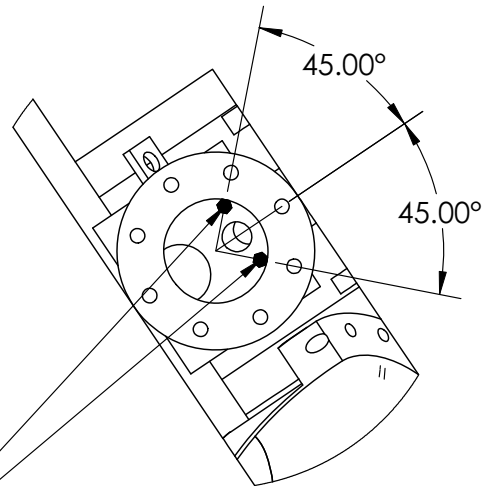
		DIMENSIONS ARE IN INCHES TOLERANCES: FRACTIONAL $\pm$ ANGULAR: MACH $\pm$ BEND $\pm$ TWO PLACE DECIMAL $\pm$ THREE PLACE DECIMAL $\pm$	DRAWN	NAME	DATE	
		MATERIAL	CHECKED			
			ENG APPR.			
			MFG APPR.			
			Q.A.			
			COMMENTS:			
PROPRIETARY AND CONFIDENTIAL						
THE INFORMATION CONTAINED IN THIS DRAWING IS THE SOLE PROPERTY OF <INSERT COMPANY NAME HERE>. ANY REPRODUCTION IN PART OR AS A WHOLE WITHOUT THE WRITTEN PERMISSION OF <INSERT COMPANY NAME HERE> IS PROHIBITED.						
NEXT ASSY	USED ON	FINISH				
APPLICATION		DO NOT SCALE DRAWING				
			SIZE	DWG. NO.		REV.
				Amain_chamber - inches		
			SCALE:1:12	WEIGHT:		SHEET 9 OF 10

Auxiliary view V



PARTIAL E-E  
SCALE 1 : 4

spot-weld 6-32 nuts here  
(nuts are not to size)



		DIMENSIONS ARE IN INCHES TOLERANCES: FRACTIONAL $\pm$ ANGULAR: MACH $\pm$ BEND $\pm$ TWO PLACE DECIMAL $\pm$ THREE PLACE DECIMAL $\pm$		DRAWN	NAME	DATE	
				CHECKED			
				ENG APPR.			
				MFG APPR.			
				Q.A.			
		COMMENTS:					
<b>PROPRIETARY AND CONFIDENTIAL</b> THE INFORMATION CONTAINED IN THIS DRAWING IS THE SOLE PROPERTY OF <INSERT COMPANY NAME HERE>. ANY REPRODUCTION IN PART OR AS A WHOLE WITHOUT THE WRITTEN PERMISSION OF <INSERT COMPANY NAME HERE> IS PROHIBITED.							
NEXT ASSY	USED ON	FINISH					
APPLICATION		DO NOT SCALE DRAWING					
		SIZE DWG. NO. <b>Amain_chamber - inches</b>					REV.
SCALE:1:12		WEIGHT:					SHEET 10 OF 10



---

## C. CAD drawings of other components

---

The special techniques group of the United Kingdom Atomic Energy Authority (UKAEA),

Special Techniques Group  
Culham Centre for Fusion Energy  
Culham Science Centre  
Abingdon  
Oxfordshire  
OX14 3DB  
United Kingdom  
[http://www.ccf.ac.uk/Special\\_Techniques.aspx](http://www.ccf.ac.uk/Special_Techniques.aspx) ,

provided the laser-diffusion bonded re-entrant viewports. In order to reach the required optical properties (high flatness and low surface roughness) for the microscope imaging setup, the window of one DN200CF re-entrant viewport was MRF-polished by

fineoptix GmbH  
Schmalheck 18  
35625 Huettenberg  
Germany  
<http://www.fineoptix.com/>

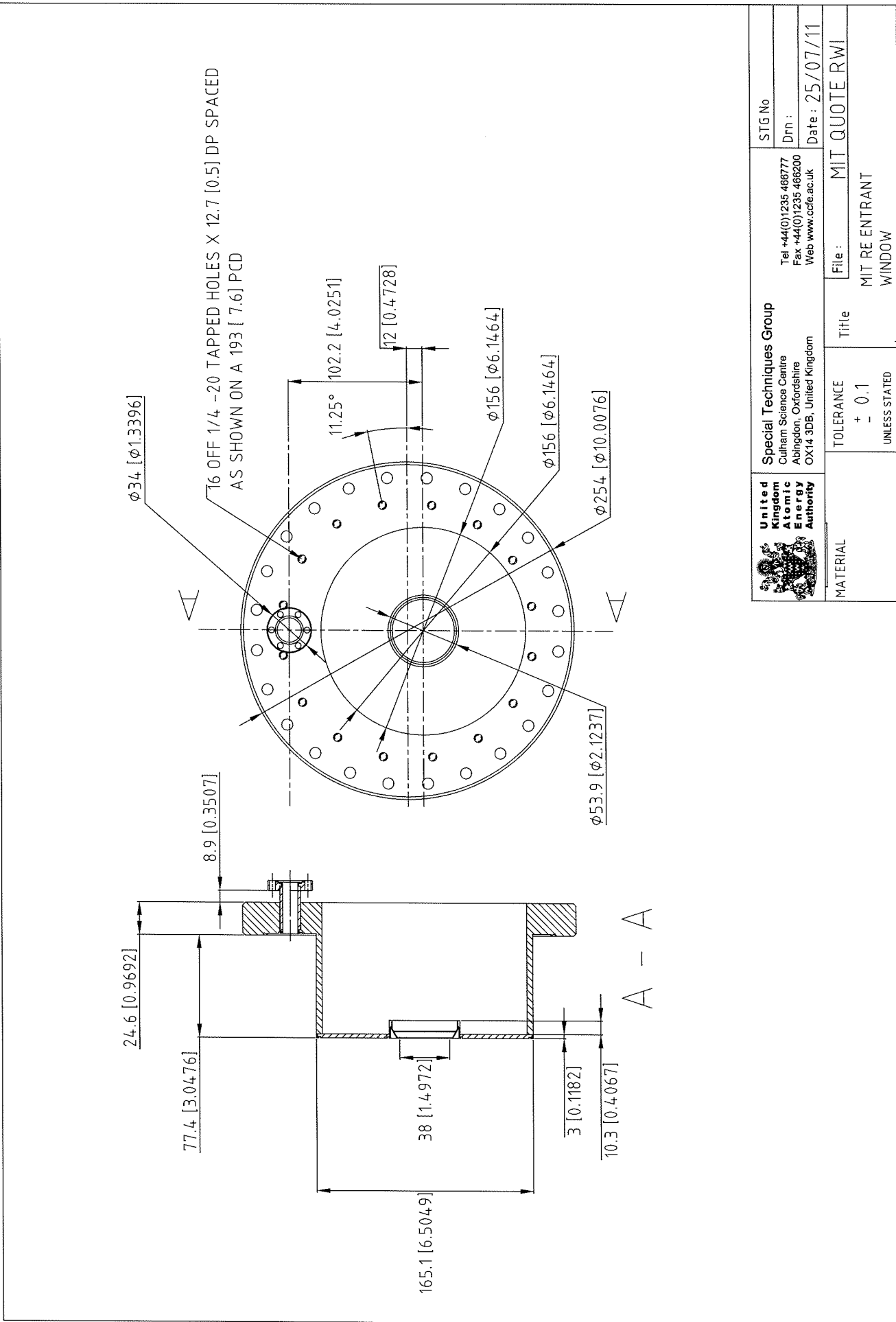
and the welded into the metal flange at UKAEA.

The other DN200CF re-entrant viewport and all DN63CF viewports were AR-coated by

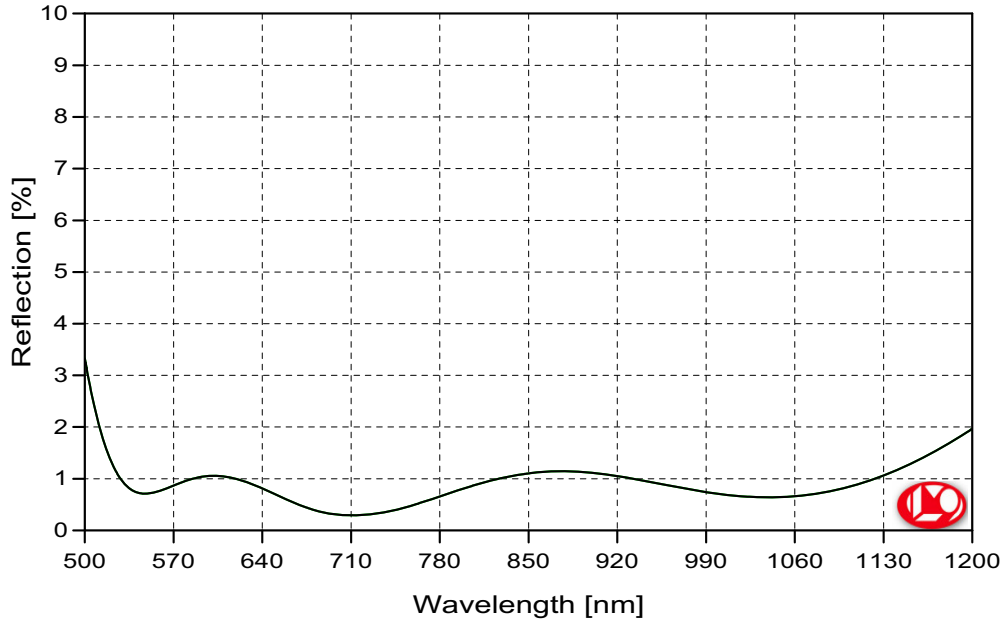
LASEROPTIK GmbH  
Gneisenaustr. 14  
30826 Garbsen  
Germany  
<http://www.laseroptik.de/>

which is shown in figure C.1.

### C.1 DN200CF re-entrant viewports



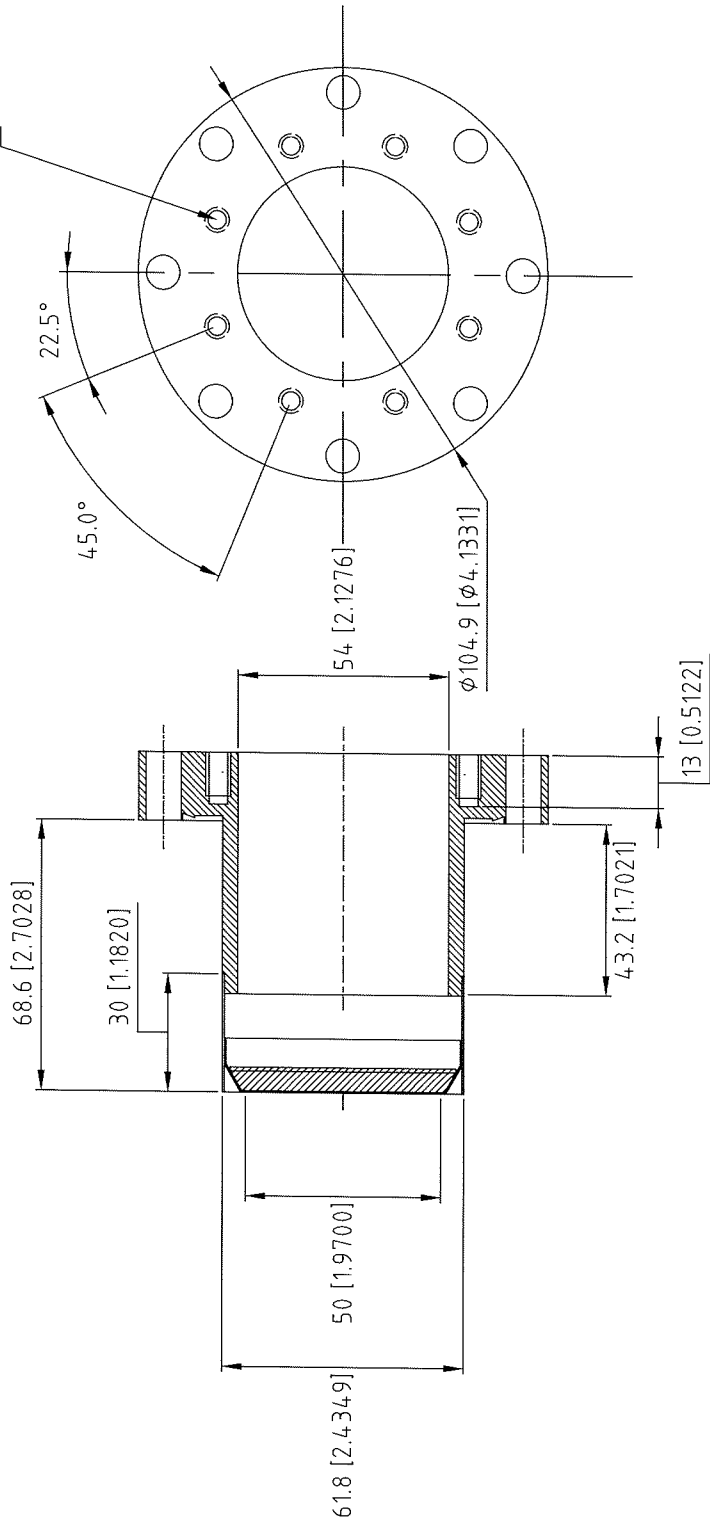
## C.2 DN63CF re-entrant viewports



B-09070: AR532+589+671+767+1064nm/0° on UHV

Figure C.1: Coating for DN63CF and one of the DN200CF viewports performed by Laseroptik GmbH.

8 OFF 1/4-20 TAPPED HOLES X 12.7[0.5] DP  
ON A 69.85[2.75] PCD AS SHOWN.

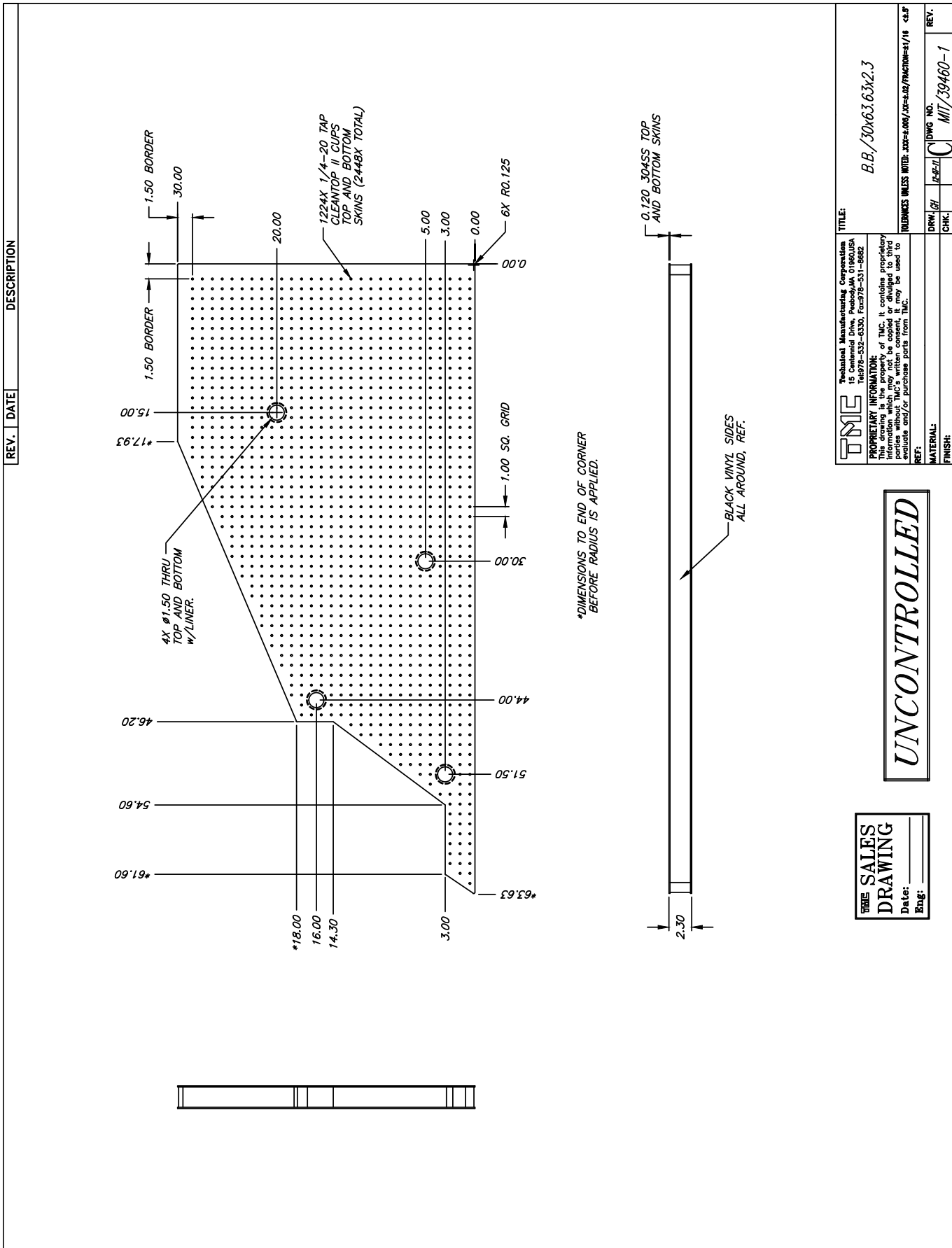


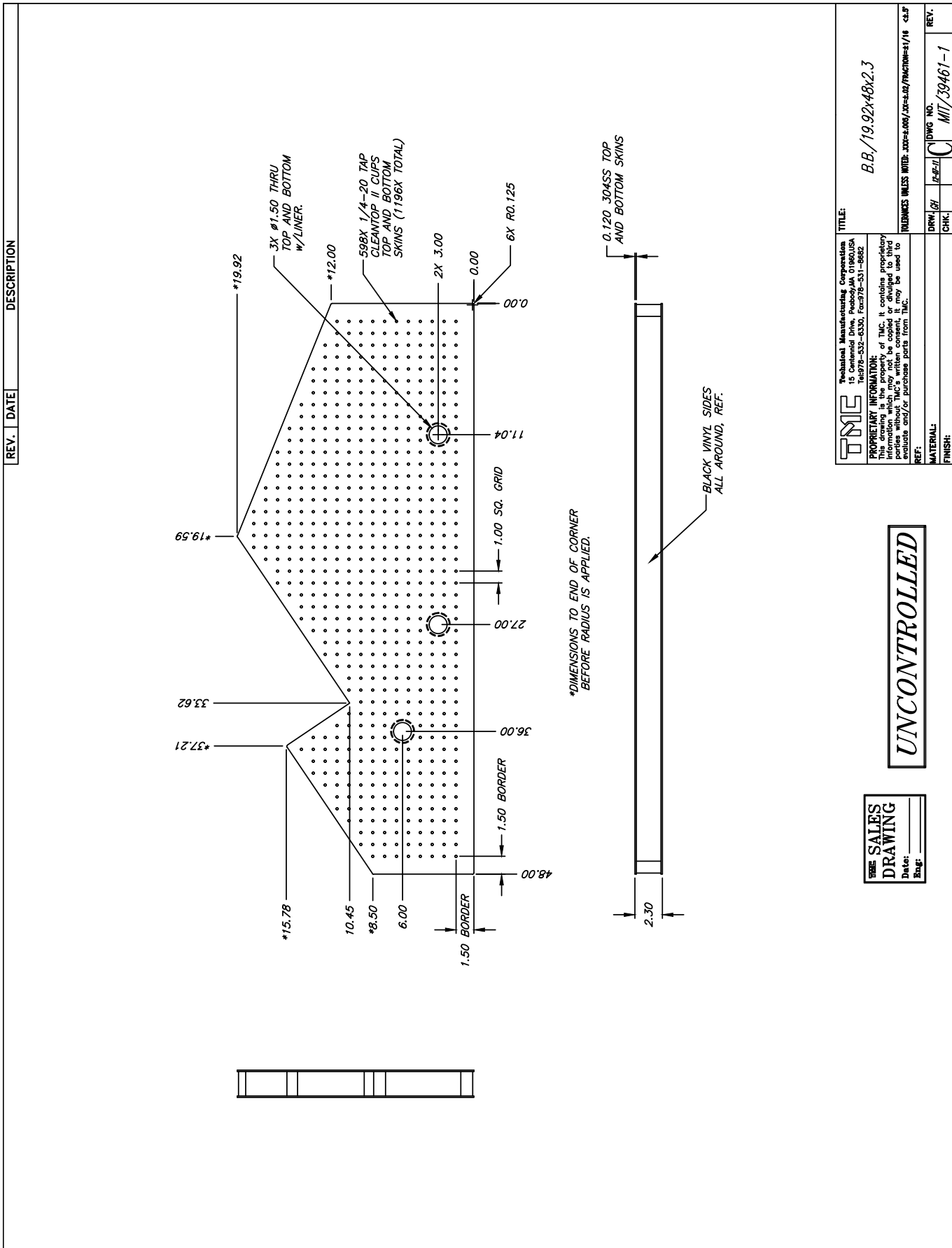
	Special Techniques Group Culham Science Centre Abingdon, Oxfordshire OX14 3DB, United Kingdom	Tel +44(0)1235 466777 Fax +44(0)1235 466200 Web www.cte.ac.uk	STG No Drn : Date : 25/07/11
MATERIAL	TOLERANCE $\pm 0.1$ UNLESS STATED	Title	File : MIT QUOTE2 RWI SMALL BUCKET

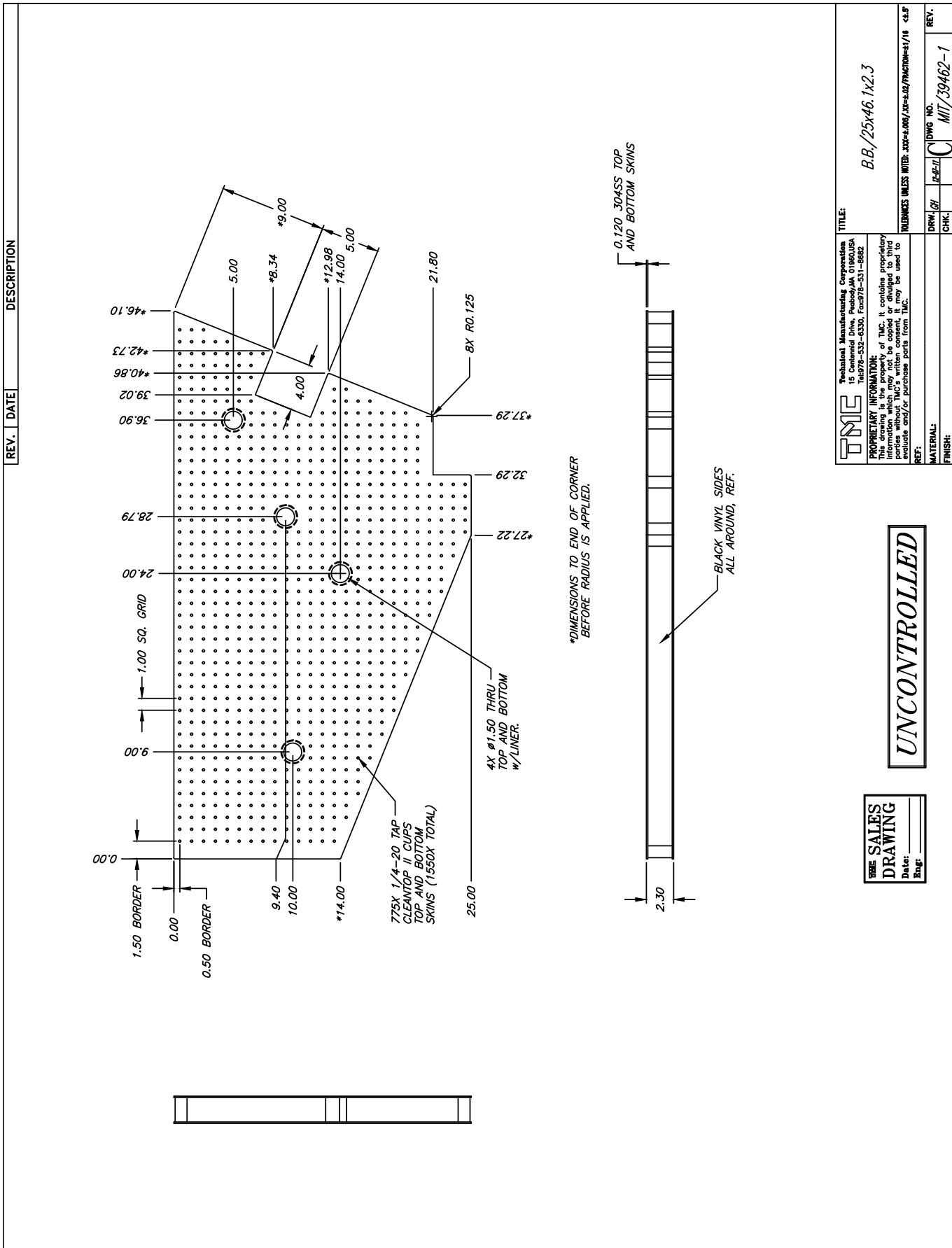
### C.3 Optical breadboards

Technical Manufacturing Corporation  
15 Centennial Drive  
Peabody, MA 01960 USA  
<http://www.techmfg.com/>

manufactured the optical breadboards that allow to mount optics on a second level above the optical table. In the following the design of these optical breadboards is presented.







---

## D. Pictures of the experiment construction

---

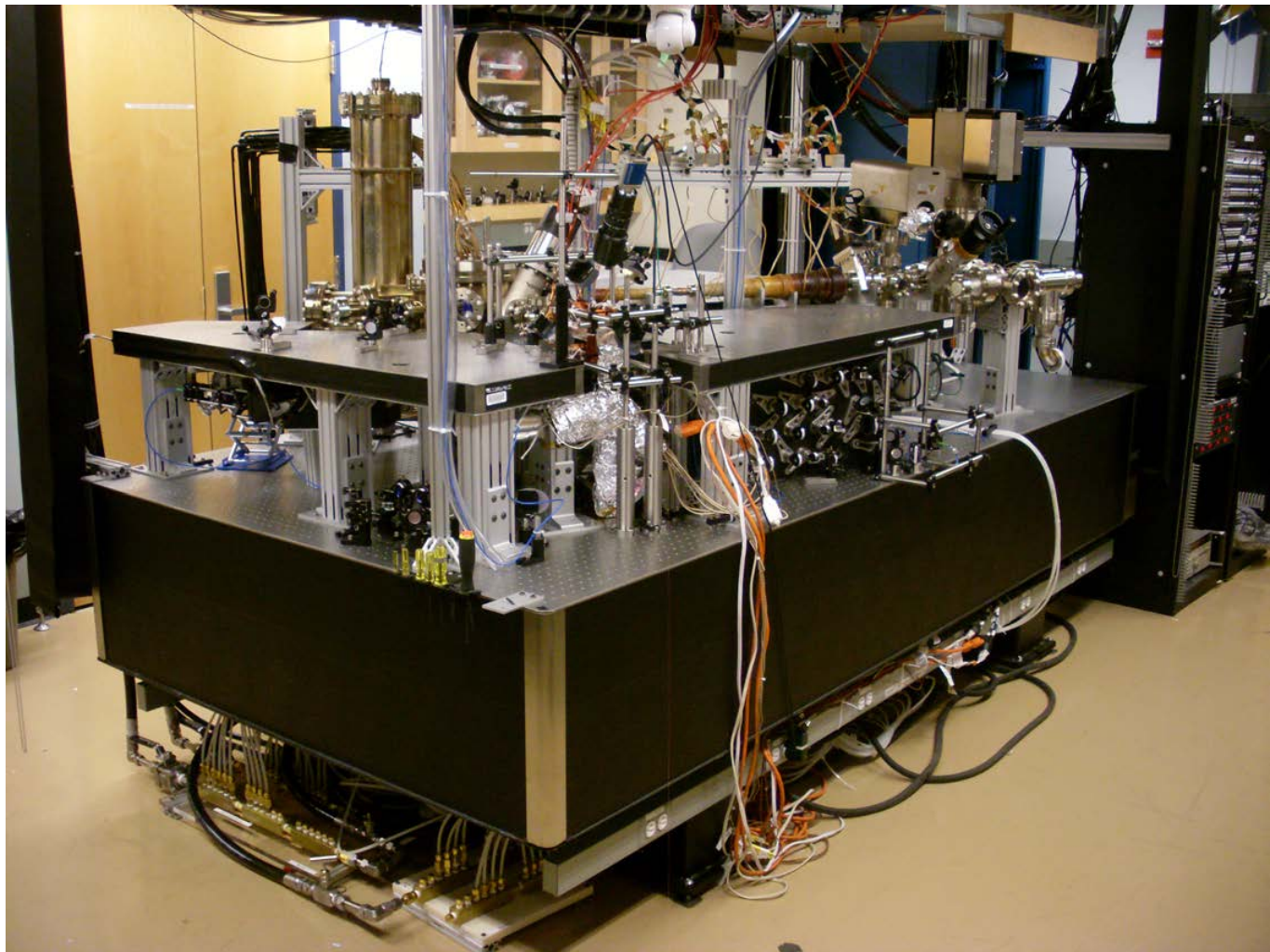


Figure D.1: Picture showing the optical table with the vacuum system and the first optical elements.

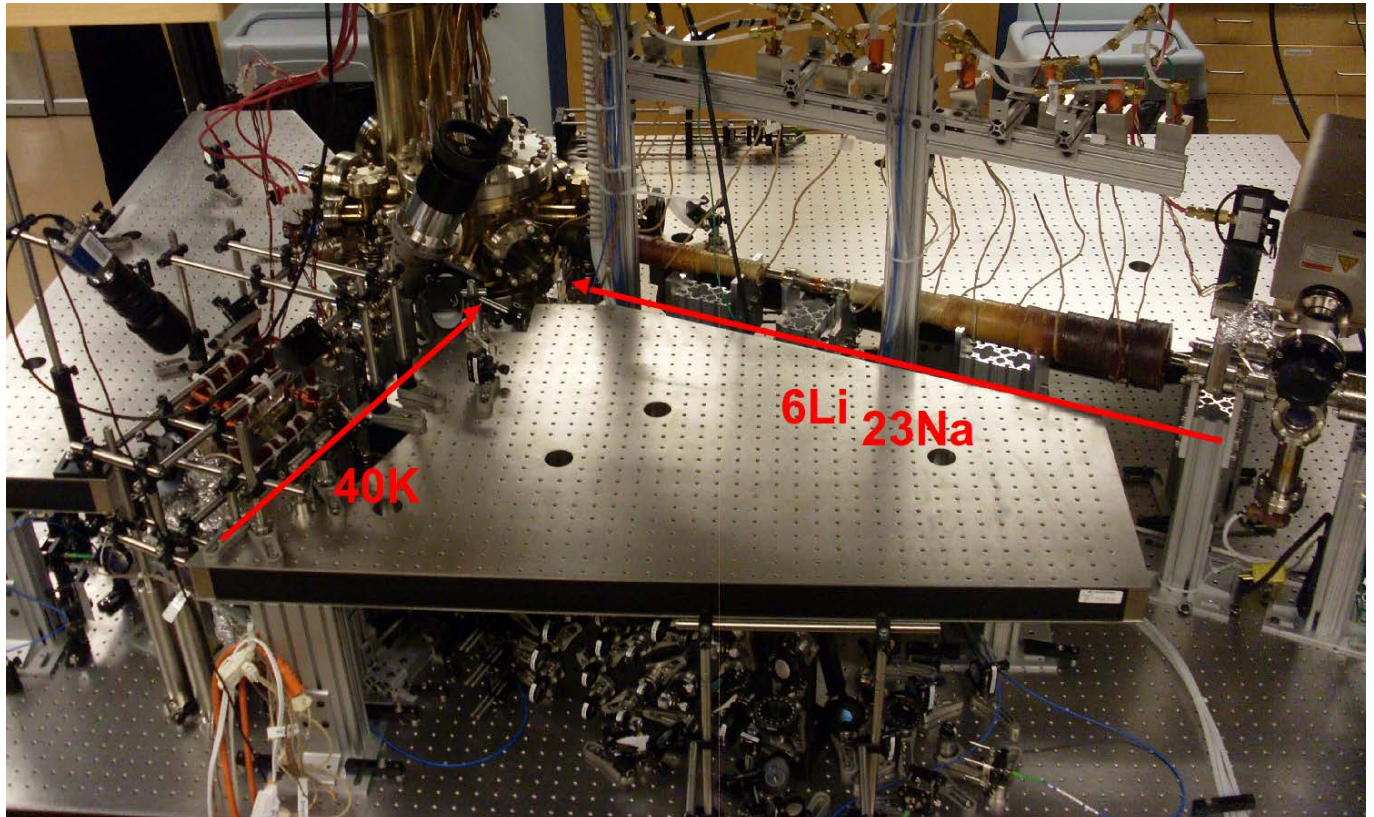


Figure D.2: View from the top: the 2D-MOT for  $^{40}\text{K}$  and the Zeeman slower for  $^{23}\text{Na}$  and  $^6\text{Li}$  are connected to main chamber on two different axes.

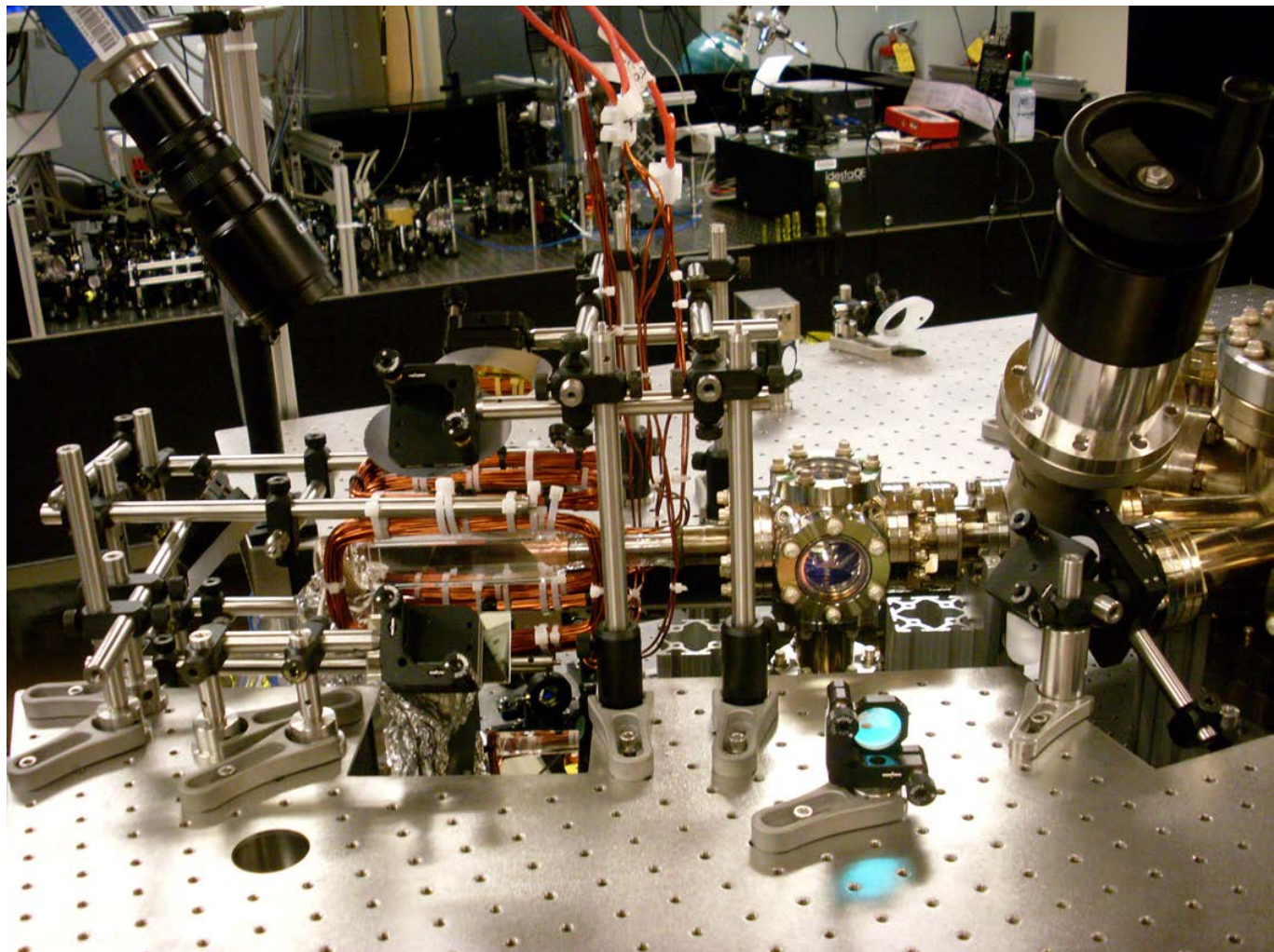


Figure D.3: Setup of the 2D-MOT connected to main chamber on the right.

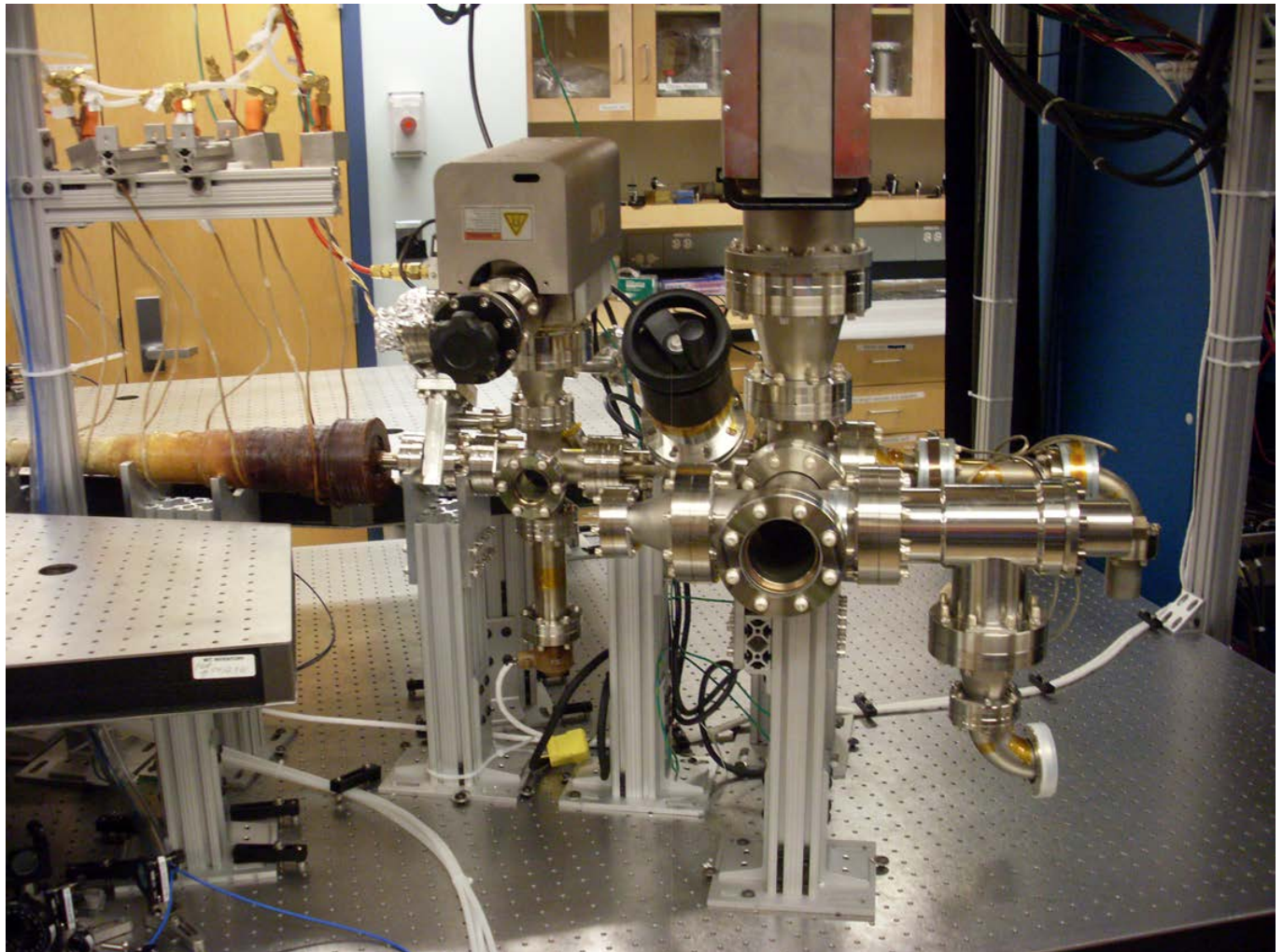


Figure D.4: Double species oven and Zeeman slower, connected to the main chamber on the left.

---

## E. Technical reference information

---

### E.1 IGBT box

To switch currents up to  $I = 600$  A industrial grade IGBTs (Mitsubishi CM1000HA-28H) are employed. Together with a diode (Powerex R7001205XXUA) and a varistor (Littelfuse V131DA40) for over-voltage protection they are built into a 19-inch rack-mount box.

As one can see in the picture in figure E.1, two IGBTs have been accommodated into one box together with water-cooling for the diode and the IGBT as well as the driving electronics (Powerex BG1A).

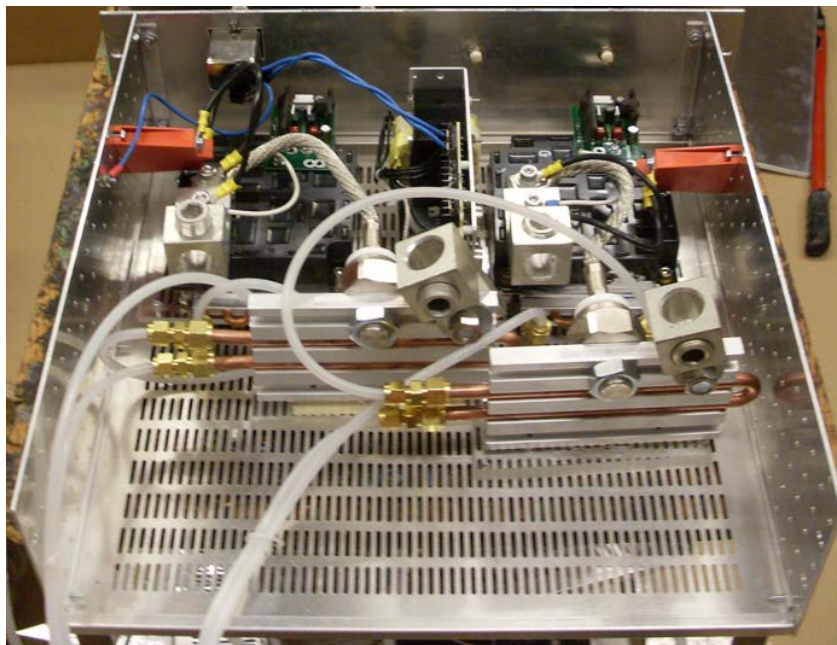
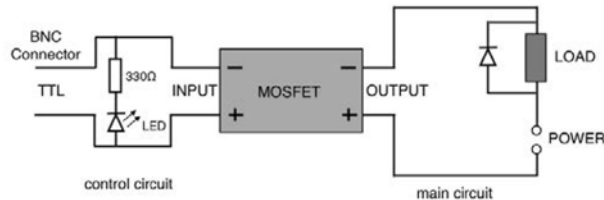


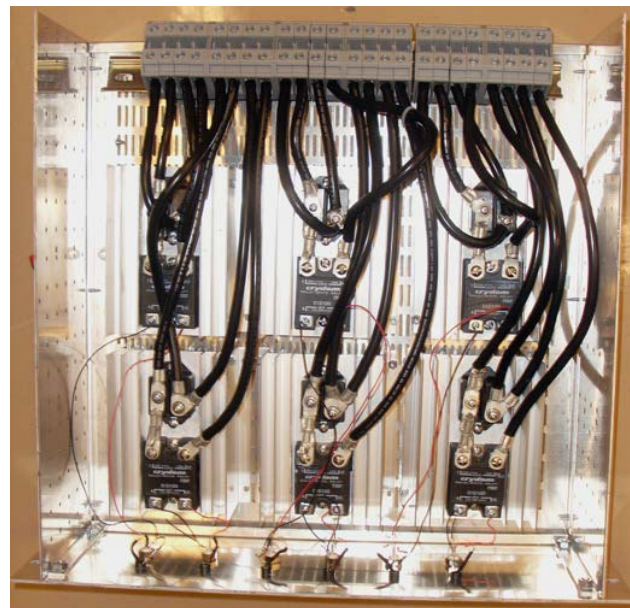
Figure E.1: Readily assembled rack-mount box housing two Mitsubishi CM1000HA-28H IGBTs together with the driving electronics. Water cooling is provided for the IGBT and the diode with the white tubing connected to the aluminum/copper cooling plates.

## E.2 MOSFET box

Two 19-inch rack-mount boxes with six MOSFETs per box have been constructed according to the schematic E.2a and depicted in E.2b. Each MOSFET can be chosen to switch up to  $I_1 = 40$  A (using Crydom D1D40 as MOSFET and Powerex CS240650 diode) or  $I_2 = 100$  A (using Crydom D1D100 and Powerex CS240610).



(a) Schematic



(b) readily assembled rack-mount box

Figure E.2: Schematic (a) and picture (b) of the readily assembled MOSFET rack-mount box with six MOSFETs.

---

## List of Figures

---

1.1	High-resolution fluorescence images and reconstructed single-site resolved occupation numbers of a superfluid BEC (left column) and Mott insulators with three different fillings (right three columns) in a two-dimensional optical lattice as observed with a bosonic quantum gas microscope. The experiment is described in [32], from which the figure was adapted.	3
1.2	Concept of quantum gas microscope: Atoms of different spin states are trapped in an optical lattice and placed in front of a high-resolution imaging system.	4
2.1	Illustration of the Pauli principle with bosonic/fermionic atoms in harmonic potential at $T \rightarrow 0$ : Whereas for bosons multiple occupation of one quantum state is possible, there is at most one fermionic atom in a single quantum state.	8
2.2	Fermi-Dirac distribution as a function of energy (vertical axis) for different temperatures expressed relative to the Fermi temperature $T_F$ . Below $T = T_F$ the Fermi-Dirac changes its shape and reaches a step function $\theta(E_F - E)$ at $E = E_F = \mu_0$ at zero temperature.	10
2.3	Interatomic potentials describing the collision of two fermionic $^6\text{Li}$ atoms in singlet (blue) or triplet (red) configuration. Due to the Pauli blocking of two electrons in the same spin configuration the triplet potential is much shallower as explained in the text. Adapted from [52].	13
2.4	Feshbach resonances: The scattering length is plotted as function of the magnetic field around the Feshbach resonance. At the Feshbach resonance (red dashed line) the scattering length diverges.	15
2.5	Creation of a 1D optical lattice: By reflecting and overlapping a laser beam a standing light wave can be created, which corresponds to a periodic optical potential. The two lenses create a Gaussian beam which enhances the depth of the potential due to the higher light intensity in the focus of the beam.	21
2.6	Bloch bands for a free particle (left graph) and for a one-dimensional lattice for three different lattice depths given in terms of the lattice recoil energy $E_R$ . A quadratic dispersion of a free particle is obtained for no lattice, whereas for increasing lattice depth gaps open up in the Bloch bands.	22
3.1	Schematic phase diagram for the Fermi-Hubbard model at half-filling for simple cubic lattice in three dimensions, adapted from [66]. AFM denotes the antiferromagnetically ordered phase. On the attractive side of the diagram $s$ -wave superfluidity with a BEC-BCS crossover is expected.	24
3.2	Double occupancy as function of atom number from [30] in (a) and compression of the trapping potential from [31] in (b). When repulsive interactions are present, the double occupancy is strongly suppressed.	25
3.3	In-situ images and reconstructed occupation numbers of <b>bosonic</b> Mott insulators with three different fillings (right three columns) in a two-dimensional optical lattice. Figure adapted from [32].	26

3.4	The metallic, Mott-insulating and band-insulating phase of a Fermi gas in an optical lattice: The left column illustrates the behavior with allowed tunneling, the center column the corresponding density distribution and the right column the 'freezing' of the different phases in the zero-tunneling limit (very deep lattice). Figure adapted from [31]. . . . .	27
3.5	Theoretically predicted phase diagram of fermions in an optical lattice showing the temperature/hole-doping concentration plane, from [38]. . . . .	28
3.6	Radial atom number occupation and fluctuations as function of local chemical potential observed by the bosonic quantum gas microscope. The lower inset shows the distribution the entropy density in the measured sample. Figure adapted from [31]. . .	29
3.7	Phase diagram of cuprate superconductors for electron- (left side) and hole-doping (right side), adapted from [70]. . . . .	29
3.8	Number filtering of Mott insulator shells as reported in [74]: With an occupation-number-selective method lattice sites with $n = 1, 2, 3, 4, \dots$ atoms are consecutively transferred into lattice sites with exactly one atom. . . . .	30
4.1	Energy level scheme showing the hyperfine structure of ${}^6\text{Li}$ , ${}^{23}\text{Na}$ and ${}^{40}\text{K}$ . The Fraunhofer $D_1$ and $D_2$ lines [86] as well as the transitions used for laser cooling are marked.	35
4.2	CAD illustration showing the setup of the imaging system inside of the re-entrant vacuum viewport (2) consisting of a microscope objective (1), the hemispherical lens below and the super-polished substrate (4) attached to the vacuum window inside the vacuum chamber. Around the objective the magnetic coils have been placed, symbolized by different colors (3). Lattice laser beams (5) can be reflected at the super-polished substrate, which is used for creating an optical lattice along the vertical direction. The recording camera is placed above the objective like shown in figure 4.3.	36
4.3	The fermi gas microscope from the bird's eye perspective: CAD illustration of the mechanical setup and some of the cooling (red: 3D-MOT) and trapping beams (green: 2D lattice). . . . .	38
4.4	CAD illustration of the custom-made main chamber mounted at its final position on top of the optical table. . . . .	39
4.5	View from the top onto the upper re-entrant viewport with the magnetic coils (colored) and the glass window with the hemisphere in it. The 3D-MOT laser beams (red) aim at the center of the main chamber, while the optical dipole trap/lattice beams (green) aim at a position which $d_{\text{offset}} = 12$ mm apart from the center. . . . .	41
4.6	CAD illustration showing a cut through the re-entrant viewports mounted to the main chamber. The offset of the centerline of the DN200CF re-entrant viewport with respect to the main chamber vacuum port is visible. . . . .	42
4.7	CAD illustration showing the 2D-MOT and the atomic source (vacuum nipple below the gate valve on the right side) for ${}^{40}\text{K}$ . . . . .	43
4.8	CAD illustration showing the double species oven for ${}^6\text{Li}$ and ${}^{23}\text{Na}$ : Two reservoirs allow separate temperature control of both atomic sources. An atomic beam (purple) is formed by different beam shaping elements, whereas a cold cup and two ion pumps capture atoms with a velocity vector not in the desired direction of the atomic beam. Two differential pumping tubes (labeled DPT) help maintaining the ultra-high vacuum in the main chamber (attached left of the Zeeman slower), while oven is at higher pressure due to the heating of the atomic sources. . . . .	46
4.9	Pictures of the lead-filled mounts for the main chamber (a), which have been made of t-slotted aluminum extrusion, and of the double-layer optical table during the construction of the experiment (b). . . . .	47

5.1 CAD illustration of the 2D-MOT part of the experiment, described in the text. . . . .	50
5.2 Fluorescence image of the 2D-MOT showing a large cloud of laser-cooled $^{39}\text{K}$ atoms. . . . .	51
5.3 Zeeman slower winding profile showing the number of turns in each layer. The increasing field section is attached right of the decreasing field section as the continuing position scale indicates. The different colors symbolize cooling circuits, all turns of a specific color have one common water cooling connection. . . . .	53
5.4 Simulated and measured longitudinal magnetic field of the Zeeman slower. . . . .	54
5.5 Schematic diagram of the laser setup used for the 2D and 3D-MOT for $^{40}\text{K}$ . AOM (DP) denotes an acousto-optic modulator in a double-pass configuration [107], the given laser frequency shift denotes the shift after the complete passage of the double-pass configuration. . . . .	55
5.6 Schematic diagram of the laser setup supplying light for the Zeeman slower and 3D-MOT for $^6\text{Li}$ . . . . .	55
5.7 Schematic diagram of the planned laser setup for $^{23}\text{Na}$ . . . . .	56
5.8 CAD illustration of one arrangement of the 3D-MOT beams: The beam tuned to the $^{23}\text{Na}$ frequency (yellow) is joined at a dichroic mirror with the beam carrying the frequencies for $^6\text{Li}$ and $^{40}\text{K}$ (red). The two frequencies for $^6\text{Li}$ and $^{40}\text{K}$ are created below the upper layer of the optical table (not shown in detail). . . . .	58
5.9 Fluorescence images showing the 3D-MOT as a bright spot in the center for $^{39}\text{K}$ (a) and $^{40}\text{K}$ (b). . . . .	59
6.1 Concept of a Cloverleaf magnetic trap and RF evaporation (figure adapted from [41]): a low-field seeking (magnetically trapped) state is flipped to a high-field seeking (magnetically antitrapped state) by a RF pulse and thereby leaves the magnetic trap. . . . .	62
6.2 Shift of the hyperfine energy levels due to the Zeeman effect for $^{40}\text{K}$ . . . . .	63
6.3 Magnetic transport of the atomic cloud at the initial 3D-MOT position (purple sphere) to the center of the chamber (big blue sphere, evaporation is performed here) and towards the objective (small blue sphere). . . . .	64
6.4 CAD rendered picture of one set of magnetic coils. The two different principal centerline axes for the MOT coil (green) and the other coils are visible. Two sets of these coils make up the magnetic trap as shown in figure 6.3. . . . .	66
6.5 Pictures of the fabrication of the coils on a lathe (a), a readily manufactured cloverleaf coil (b) and the alignment in a special structure to glue them together (c). . . . .	68
6.6 Pictures of the readily manufactured coil package (left) and the setup for the magnetic field test (right) with magnetic field probe (long black rod) on a three-axis translation stage, described in detail in the text. . . . .	69
6.7 Schematic diagram showing the water cooling setup of the experiment (symbols according to DIN/ISO 1219, [124]), explained in detail in the text. . . . .	70
6.8 Schematic of the electric setup of the power supplies powering the magnetic coils, explained in the text. . . . .	71
6.9 Magnetic field measurements of the magnetic trap. . . . .	73
6.10 Graph showing a possible example of current ramps to move the atoms from the magnetic quadrupole to the Ioffe-Pritchard trap as described in the text. . . . .	75
6.11 Magnitude of the magnetic field during ramping from the quadrupole trap to cloverleaf trap along the $x$ - $y$ -plane (a) and the $x$ - $z$ -plane (b). . . . .	76
6.12 RF antenna for evaporation mounted on one re-entrant viewport. . . . .	78

7.1	Enhancement of the numerical aperture with a hemispherical lens attached to the vacuum window. Below the vacuum window a super-polished substrate is optically contacted to reduce surface scattering. . . . .	82
7.2	The hemisphere has been contacted to the viewport using a small vacuum pump mounted on three-dimensional translation stage as shown in (a). On the right the hemispheric lens and the little mirror for reflecting a 3D-MOT beam are visible in the readily assembled system (b). . . . .	83
7.3	Testing the microscope objective with a interferometry setup: The image shows the relative wavefront distortion from the transmission of the objective relative to the imaging wavelength $\lambda = 766.7017$ nm. . . . .	85
7.4	Fizeau interferometer images of the curved surface of the hemisphere. On the left side (a) the interference fringes with a reference Fizeau plate are visible, showing wavefront distortions. On the right side one half of the imaging has been blocked to prove that the interference fringes are coming from the curved surface (b). . . . .	86
7.5	Fizeau interference images of the flat surface of the prototype imaging system consisting of a hemispheric lens contacted to a reference flat window with 5 mm thickness. In (a) the Fizeau plate is tilted with respect to the flat surface yielding Fizeau interference fringes, in (b) the Fizeau plate has been aligned coplanar with the reference flat and hence the interference fringes disappear. . . . .	87
7.6	Testing with imaging system with fluorescent nano-spheres: By imaging a single nanosphere ( $\phi < 100$ nm) the diffraction-limited resolution of the microscope objective could be confirmed. . . . .	88
7.7	A lattice with a lattice constant of $a \approx 10 \mu\text{m}$ is created by reflecting laser beams with wavelength $\lambda = 1064$ nm of the surface of the superpolished substrate at a very small angle. . . . .	88
8.1	The assembled mechanical setup of the experiment. Another optical table accommodates most of the optical setup, which is not shown in this picture. . . . .	91
8.2	Absorption image of $^{40}\text{K}$ atoms trapped by the magnetic quadrupole coils. . . . .	92
A.1	Both the hemispherical lens of the imaging systems and all the main chamber viewports except the re-entrant viewports are coated with an IBS coating suitable for the $D_2$ lines of $^{23}\text{Na}$ , $^6\text{Li}$ and $^{40}\text{K}$ as well as $\lambda_{\text{lat}} = 1064$ nm for the optical lattice. . . . .	95
A.2	Coating of the surfaces of the super-polished substrate. One surface is coated with highly reflective (labeled HR) coating, the other side with anti-reflection coating to compensate for stress during the coating process and avoid reflection at this surface. . . . .	96
A.3	Interferometric measurement of the wavefront distortion (reflection of the surface) of the two sides of the re-entrant viewport that is part of the imaging system (see chapter 7). Deviations are given in terms of the interferometer wavelength $\lambda_{\text{inf}} = 546.07$ nm. . . . .	98
A.4	Drawing of the planoconvex lens used as hemispheric lens in combination with the re-entrant viewport window as shown in figure 7.1. . . . .	99
C.1	Coating for DN63CF and one of the DN200CF viewports performed by Laseroptik GmbH. . . . .	115
D.1	Picture showing the optical table with the vacuum system and the first optical elements. . . . .	121
D.2	View from the top: the 2D-MOT for $^{40}\text{K}$ and the Zeeman slower for $^{23}\text{Na}$ and $^6\text{Li}$ are connected to main chamber on two different axes. . . . .	122
D.3	Setup of the 2D-MOT connected to main chamber on the right. . . . .	123
D.4	Double species oven and Zeeman slower, connected to the main chamber on the left. . . . .	124

E.1 Readily assembled rack-mount box housing two Mitsubishi CM1000HA-28H IGBTs together with the driving electronics. Water cooling is provided for the IGBT and the diode with the white tubing connected to the aluminum/copper cooling plates. . . . .	125
E.2 Schematic (a) and picture (b) of the readily assembled MOSFET rack-mount box with six MOSFETs. . . . .	126

---

## List of Tables

---

4.1	General physical properties of the atomic species used in this experiment. . . . .	34
6.1	Properties of the magnetic coils. The coil referred as 'MOT' is used for creating the 3D-MOT and subsequently used as magnetic quadrupole coil by running a higher current through the same coil. . . . .	67
6.2	Electrical specifications of the manufactured coils: The resistance is given for the whole circuit including the switching IGBT with a diode. The maximal current is given for the configuration where one power supply powers all coil layers of one coil type (compare figure 6.8). . . . .	72

---

## Bibliography

---

- [1] W. S. Bakr, A. Peng, M. E. Tai, R. Ma, J. Simon, J. I. Gillen, S. Folling, L. Pollet, M. Greiner. Probing the Superfluid-to-Mott insulator transition at the Single-Atom level. *Science*, **329**(5991) (2010) 547–550.
- [2] Jacob F. Sherson, Christof Weitenberg, Manuel Endres, Marc Cheneau, Immanuel Bloch, Stefan Kuhr. Single-atom-resolved fluorescence imaging of an atomic mott insulator. *Nature*, **467**(7311) (2010) 68–72.
- [3] J. G. Bednorz, K. A. Müller. Possible high T<sub>c</sub> superconductivity in the BaLaCuO system. *Zeitschrift für Physik B Condensed Matter*, **64**(2) (1986) 189–193.
- [4] A P Ramirez. Colossal magnetoresistance. *Journal of Physics: Condensed Matter*, **9**(39) (1997) 8171–8199.
- [5] Tsuneya Ando, Alan B. Fowler, Frank Stern. Electronic properties of two-dimensional systems. *Reviews of Modern Physics*, **54**(2) (1982) 437–672.
- [6] Horst L. Stormer. Nobel lecture: The fractional quantum hall effect. *Reviews of Modern Physics*, **71**(4) (1999) 875–889.
- [7] Markus König, Steffen Wiedmann, Christoph Brüne, Andreas Roth, Hartmut Buhmann, Laurens W. Molenkamp, Xiao-Liang Qi, Shou-Cheng Zhang. Quantum spin hall insulator state in HgTe quantum wells. *Science*, **318**(5851) (2007) 766 –770.
- [8] Richard P. Feynman. Simulating physics with computers. *International Journal of Theoretical Physics*, **21**(6-7) (1982) 467–488.
- [9] K. B. Davis, M. -O. Mewes, M. R. Andrews, N. J. van Druten, D. S. Durfee, D. M. Kurn, W. Ketterle. Bose-Einstein condensation in a gas of sodium atoms. *Physical Review Letters*, **75**(22) (1995) 3969–3973.
- [10] M. H. Anderson, J. R. Ensher, M. R. Matthews, C. E. Wieman, E. A. Cornell. Observation of Bose-Einstein condensation in a dilute atomic vapor. *Science*, **269**(5221) (1995) 198 – 201.
- [11] M. Greiner, C. A Regal, D. S Jin. Emergence of a molecular Bose-Einstein condensate from a fermi gas. *Nature*, **426**(6966) (2003) 537–540.
- [12] S. Jochim. Bose-Einstein condensation of molecules. *Science*, **302**(5653) (2003) 2101–2103.
- [13] M. W. Zwierlein, C. A. Stan, C. H. Schunck, S. M. F. Raupach, A. J. Kerman, W. Ketterle. Condensation of pairs of fermionic atoms near a feshbach resonance. *Physical Review Letters*, **92**(12) (2004) 120403.
- [14] Markus Greiner, Olaf Mandel, Tilman Esslinger, Theodor W. Hansch, Immanuel Bloch. Quantum phase transition from a superfluid to a mott insulator in a gas of ultracold atoms. *Nature*, **415**(6867) (2002) 39–44.

- [15] A. Cavalleri, Cs. Tóth, C. W. Siders, J. A. Squier, F. Ráksi, P. Forget, J. C. Kieffer. Femtosecond structural dynamics in VO<sub>2</sub> during an ultrafast Solid-Solid phase transition. *Physical Review Letters*, **87**(23) (2001) 237401.
- [16] A. L. Cavalieri, N. Müller, Th. Uphues, V. S. Yakovlev, A. Baltuska, B. Horvath, B. Schmidt, L. Blümel, R. Holzwarth, S. Hendel, M. Drescher, U. Kleineberg, P. M. Echenique, R. Kienberger, F. Krausz, U. Heinzmann. Attosecond spectroscopy in condensed matter. *Nature*, **449**(7165) (2007) 1029–1032.
- [17] M. R Andrews, C. G Townsend, H. -J Miesner, D. S Durfee, D. M Kurn, W. Ketterle. Observation of interference between two bose condensates. *Science*, **275**(5300) (1997) 637–641.
- [18] M. R. Andrews, D. M. Kurn, H.-J. Miesner, D. S. Durfee, C. G. Townsend, S. Inouye, W. Ketterle. Propagation of sound in a Bose-Einstein condensate. *Physical Review Letters*, **79**(4) (1997) 553–556.
- [19] D. M. Stamper-Kurn, A. P. Chikkatur, A. Görlitz, S. Inouye, S. Gupta, D. E. Pritchard, W. Ketterle. Excitation of phonons in a Bose-Einstein condensate by light scattering. *Physical Review Letters*, **83**(15) (1999) 2876–2879.
- [20] M. R. Matthews, B. P. Anderson, P. C. Haljan, D. S. Hall, C. E. Wieman, E. A. Cornell. Vortices in a Bose-Einstein condensate. *Physical Review Letters*, **83**(13) (1999) 2498–2501.
- [21] K. W. Madison, F. Chevy, W. Wohlleben, J. Dalibard. Vortex formation in a stirred Bose-Einstein condensate. *Physical Review Letters*, **84**(5) (2000) 806–809.
- [22] J. R Abo-Shaeer, C. Raman, J. M Vogels, W. Ketterle. Observation of vortex lattices in Bose-Einstein condensates. *Science*, **292**(5516) (2001) 476–479.
- [23] B. DeMarco, D. S. Jin. Onset of fermi degeneracy in a trapped atomic gas. *Science*, **285**(5434) (1999) 1703 –1706.
- [24] S. Inouye, M. R. Andrews, J. Stenger, H. J Miesner, D. M. Stamper-Kurn, W. Ketterle. Observation of feshbach resonances in a Bose-Einstein condensate. *Nature*, **392**(6672) (1998) 151–154.
- [25] D. Jaksch, C. Bruder, J. I. Cirac, C. W. Gardiner, P. Zoller. Cold bosonic atoms in optical lattices. *Physical Review Letters*, **81**(15) (1998) 3108–3111.
- [26] Matthew P. A. Fisher, Peter B. Weichman, G. Grinstein, Daniel S. Fisher. Boson localization and the superfluid-insulator transition. *Physical Review B*, **40**(1) (1989) 546–570.
- [27] Michael Köhl, Henning Moritz, Thilo Stöferle, Kenneth Günter, Tilman Esslinger. Fermionic atoms in a three dimensional optical lattice: Observing fermi surfaces, dynamics, and interactions. *Physical Review Letters*, **94**(8) (2005) 080403.
- [28] Kenneth Günter, Thilo Stöferle, Henning Moritz, Michael Köhl, Tilman Esslinger. Bose-Fermi mixtures in a Three-Dimensional optical lattice. *Physical Review Letters*, **96**(18) (2006) 180402.
- [29] S. Ospelkaus, C. Ospelkaus, O. Wille, M. Succo, P. Ernst, K. Sengstock, K. Bongs. Localization of bosonic atoms by fermionic impurities in a Three-Dimensional optical lattice. *Physical Review Letters*, **96**(18) (2006) 180403.

- [30] Robert Jördens, Niels Strohmaier, Kenneth Gunter, Henning Moritz, Tilman Esslinger. A mott insulator of fermionic atoms in an optical lattice. *Nature*, **455**(7210) (2008) 204–207.
- [31] U. Schneider, L. Hackermüller, S. Will, Th. Best, I. Bloch, T. A. Costi, R. W. Helmes, D. Rasch, A. Rosch. Metallic and insulating phases of repulsively interacting fermions in a 3D optical lattice. *Science*, **322**(5907) (2008) 1520 –1525.
- [32] Christof Weitenberg, Manuel Endres, Jacob F. Sherson, Marc Cheneau, Peter Schauß, Takeshi Fukuhara, Immanuel Bloch, Stefan Kuhr. Single-spin addressing in an atomic mott insulator. *Nature*, **471**(7338) (2011) 319–324.
- [33] G. Binnig, H. Rohrer, Ch. Gerber, E. Weibel. Surface studies by scanning tunneling microscopy. *Physical Review Letters*, **49**(1) (1982) 57–61.
- [34] Rolf Erni, Marta Rossell, Christian Kisielowski, Ulrich Dahmen. Atomic-Resolution imaging with a sub-50-pm electron probe. *Physical Review Letters*, **102**(9) (2009).
- [35] Karl D. Nelson, Xiao Li, David S. Weiss. Imaging single atoms in a three-dimensional array. *Nature Physics*, **3**(8) (2007) 556–560.
- [36] Waseem S. Bakr, Jonathon I. Gillen, Amy Peng, Simon Fölling, Markus Greiner. A quantum gas microscope for detecting single atoms in a hubbard-regime optical lattice. *Nature*, **462**(7269) (2009) 74–77.
- [37] F. Serwane, G. Zürn, T. Lompe, T. B Ottenstein, A. N Wenz, S. Jochim. Deterministic preparation of a tunable Few-Fermion system. *Science*, **332**(6027) (2011) 336–338.
- [38] W. Hofstetter, J. I. Cirac, P. Zoller, E. Demler, M. D. Lukin. High-Temperature superfluidity of fermionic atoms in optical lattices. *Physical Review Letters*, **89**(22) (2002) 220407.
- [39] Simon Trebst, Ulrich Schollwöck, Matthias Troyer, Peter Zoller. d-Wave resonating valence bond states of fermionic atoms in optical lattices. *Physical Review Letters*, **96**(25) (2006) 250402.
- [40] Vinay V. Ramasesh. Towards a quantum gas microscope for fermionic atoms, 2012. Thesis (S.B.)—Massachusetts Institute of Technology, Dept. of Physics, 2012.
- [41] Wolfgang Ketterle, Martin W. Zwierlein. Making, probing and understanding ultracold fermi gases. *0801.2500*, Januar 2008.
- [42] Stefano Giorgini, Lev P. Pitaevskii, Sandro Stringari. Theory of ultracold atomic fermi gases. *Reviews of Modern Physics*, **80**(4) (2008) 1215–1274.
- [43] Sebastian Will. *Interacting bosons and fermions in three-dimensional optical lattice potentials: from atom optics to quantum simulation / Sebastian Will*. Universitätsbibliothek Mainz, Mainz, 2011.
- [44] W. Ketterle, D. S Durfee, D. M Stamper-Kurn. Making, probing and understanding Bose-Einstein condensates. *cond-mat/9904034*, April 1999.
- [45] Immanuel Bloch, Wilhelm Zwerger. Many-body physics with ultracold gases. *Reviews of Modern Physics*, **80**(3) (2008) 885–964.
- [46] Kerson Huang. *Statistical Mechanics 2E*. John Wiley & Sons, 2. ed., April 1987.

- [47] W. Pauli. The connection between spin and statistics. *Physical Review*, **58**(8) (1940) 716–722.
- [48] Michael E. Peskin, Daniel V. Schroeder. *An Introduction To Quantum Field Theory*. Westview Press, Oktober 1995.
- [49] D.J. Griffiths. *Introduction to quantum mechanics*. Pearson Prentice Hall, 2005.
- [50] D.A. McQuarrie. *Statistical Mechanics*. University Science Books, 2000.
- [51] Claude Cohen-Tannoudji, David Guery-Odelin. *Advances In Atomic Physics: An Overview*. World Scientific Publishing Company, November 2011.
- [52] Cheng Chin, Paul Julienne, Eite Tiesinga. Feshbach resonances in ultracold gases. *Reviews of Modern Physics*, **82**(2) (2010) 1225–1286.
- [53] J. J. Sakurai, Jim J. Napolitano. *Modern Quantum Mechanics*. Addison Wesley, 2 ed., Juli 2010.
- [54] T.W. Hänsch, A.L. Schawlow. Cooling of gases by laser radiation. *Optics Communications*, **13**(1) (1975) 68 – 69.
- [55] E. L. Raab, M. Prentiss, Alex Cable, Steven Chu, D. E. Pritchard. Trapping of neutral sodium atoms with radiation pressure. *Phys. Rev. Lett.*, **59**(23) (1987) 2631–2634.
- [56] J. E. Bjorkholm, R. R. Freeman, A. Ashkin, D. B. Pearson. Observation of focusing of neutral atoms by the dipole forces of Resonance-Radiation pressure. *Physical Review Letters*, **41**(20) (1978) 1361–1364.
- [57] Steven Chu, J. E. Bjorkholm, A. Ashkin, A. Cable. Experimental observation of optically trapped atoms. *Physical Review Letters*, **57**(3) (1986) 314–317.
- [58] Rudolf Grimm, Matthias Weidmüller, Yurii B Ovchinnikov. Optical dipole traps for neutral atoms. *arXiv:physics/9902072*, Februar 1999. Advances in Atomic, Molecular and Optical Physics Vol. 42, 95-170 (2000).
- [59] Marlan O Scully, Muhammad Suhail Zubairy. *Quantum optics*. Cambridge University Press, Cambridge; New York, 1997.
- [60] Claude Cohen-Tannoudji. Manipulating atoms with photons. *Physica Scripta*, **T76**(1) (1998) 33.
- [61] Markus Greiner. Ultracold quantum gases in three-dimensional optical lattice potentials. <http://edoc.ub.uni-muenchen.de/968/>, April 2003.
- [62] S. Autler, C. Townes. Stark effect in rapidly varying fields. *Physical Review*, **100**(2) (1955) 703–722.
- [63] Harald Ibach, Hans Lüth. *Solid-State Physics: An Introduction to Principles of Materials Science*. Springer, November 2009.
- [64] J. Hubbard. Electron correlations in narrow energy bands. *Proceedings of the Royal Society of London. Series A. Mathematical and Physical Sciences*, **276**(1365) (1963) 238–257.
- [65] Antoine Georges. Condensed matter physics with light and atoms: Strongly correlated cold fermions in optical lattices. *arXiv:cond-mat/0702122*, Februar 2007.

- [66] Tilman Esslinger. Fermi-Hubbard physics with atoms in an optical lattice. *Annual Review of Condensed Matter Physics*, **1**(1) (2010) 129–152.
- [67] Arnaud Koetsier, R. A. Duine, Immanuel Bloch, H. T. C. Stoof. Achieving the neel state in an optical lattice. *arXiv:0711.3425*, November 2007. Phys. Rev. A **77**, 023623 (2008).
- [68] F. Werner, O. Parcollet, A. Georges, S. R. Hassan. Interaction-induced adiabatic cooling and antiferromagnetism of cold fermions in optical lattices. *Physical Review Letters*, **95**(5) (2005) 056401.
- [69] T. A. Corcovilos, S. K. Baur, J. M. Hitchcock, E. J. Mueller, R. G. Hulet. Detecting antiferromagnetism of atoms in an optical lattice via optical bragg scattering. *Physical Review A*, **81**(1) (2010) 013415.
- [70] Andrea Damascelli, Zahid Hussain, Zhi-Xun Shen. Angle-resolved photoemission studies of the cuprate superconductors. *Reviews of Modern Physics*, **75**(2) (2003) 473–541.
- [71] P. W. Anderson. The resonating valence bond state in La<sub>2</sub>CuO<sub>4</sub> and superconductivity. *Science*, **235**(4793) (1987) 1196–1198.
- [72] Patrick A. Lee, Naoto Nagaosa, Xiao-Gang Wen. Doping a mott insulator: Physics of high-temperature superconductivity. *Reviews of Modern Physics*, **78**(1) (2006) 17–85.
- [73] T. Scheike, W. Böhlmann, P. Esquinazi, J. Barzola-Quiquia, A. Ballestar, A. Setzer. Can doping graphite trigger room temperature superconductivity? evidence for granular high-temperature superconductivity in water-treated graphite powder. *Advanced Materials*, 2012.
- [74] Waseem S. Bakr, Philipp M. Preiss, M. Eric Tai, Ruichao Ma, Jonathan Simon, Markus Greiner. Orbital excitation blockade and algorithmic cooling in quantum gases. *Nature*, **480**(7378) (2011) 500–503.
- [75] Y.-J. Lin, R. L. Compton, K. Jiménez-García, J. V. Porto, I. B. Spielman. Synthetic magnetic fields for ultracold neutral atoms. *Nature*, **462**(7273) (2009) 628–632.
- [76] Pengjun Wang, Zeng-Qiang Yu, Zhengkun Fu, Jiao Miao, Lianghui Huang, Shijie Chai, Hui Zhai, Jing Zhang. Spin-orbit coupled degenerate fermi gases. *arXiv:1204.1887*, April 2012.
- [77] Lawrence W. Cheuk, Ariel T. Sommer, Zoran Hadzibabic, Tarik Yefsah, Waseem S. Bakr, Martin W. Zwierlein. Spin-injection spectroscopy of a spin-orbit coupled fermi gas. *arXiv:1205.3483*, Mai 2012.
- [78] Chuanwei Zhang, Sumanta Tewari, Roman M. Lutchyn, S. Das Sarma. p\_x+ip\_y superfluid from s-wave interactions of fermionic cold atoms. *Physical Review Letters*, **101**(16) (2008) 160401.
- [79] Masatoshi Sato, Yoshiro Takahashi, Satoshi Fujimoto. Non-abelian topological order in s-wave superfluids of ultracold fermionic atoms. *Physical Review Letters*, **103**(2) (2009) 020401.
- [80] Vladan Vuletić, Andrew J Kerman, Cheng Chin, Steven Chu. Laser cooling: Beyond optical molasses and beyond closed transitions. *AIP Conference Proceedings*, **551**(1) (2001) 356–366.

- [81] Jee Woo Park, Cheng-Hsun Wu, Ibon Santiago, Tobias G. Tiecke, Peyman Ahmadi, Martin W. Zwierlein. Quantum degenerate Bose-Fermi mixture of chemically different atomic species with widely tunable interactions. *arXiv:1110.4552*, Oktober 2011.
- [82] NIST: atomic weights and isotopic compositions of the elements. <http://www.nist.gov/pml/data/comp.cfm>.
- [83] Brookhaven National Laboratory National Nuclear Data Center. Chart of nuclides. <http://www.nndc.bnl.gov/chart>.
- [84] Canadian Metallurgical Quarterly. Vapor pressure of the metallic elements. *Elements*, **4** (2000) 5–7.
- [85] William M Haynes. *CRC Handbook of Chemistry and Physics 2011*. Taylor & Francis, August 2010.
- [86] G. Kirchhoff. Ueber die fraunhofer'schen linien. *Annalen der Physik*, **185**(1) (1860) 148–150.
- [87] C. H. Schunck, M. W. Zwierlein, C. A. Stan, S. M. F. Raupach, W. Ketterle, A. Simoni, E. Tiesinga, C. J. Williams, P. S. Julienne. Feshbach resonances in fermionic  ${}^6\text{Li}$ . *Physical Review A*, **71**(4) (2005) 045601.
- [88] United states patent: 3298719, Januar 1967.
- [89] British Stainless Steel Association. Magnetic properties of stainless steel, Mai 2000.
- [90] Ananth P. Chikkatur. Colliding and moving Bose-Einstein condensates: studies of superfluidity and optical tweezers for condensate transport. <http://dspace.mit.edu/handle/1721.1/16907>, 2003. Thesis (Ph. D.)–Massachusetts Institute of Technology, Dept. of Physics, February 2003.
- [91] Dan M. Stamper-Kurn. Peeking and poking at a new quantum fluid: Studies of gaseous bose-einstein condensates in magnetic and optical traps. [http://cua.mit.edu/ketterle\\_group/Theeses/DSDThesis.pdf](http://cua.mit.edu/ketterle_group/Theeses/DSDThesis.pdf), 2000. Thesis (Ph. D.)–Massachusetts Institute of Technology, Dept. of Physics, February 2000.
- [92] UKAEA Special Techniques Group, Culham Centre for Fusion Energy. [http://www.ccfef.ac.uk/Diffusion\\_bonding.aspx](http://www.ccfef.ac.uk/Diffusion_bonding.aspx).
- [93] C. A Stan, W. Ketterle. Multiple species atom source for laser-cooling experiments. *Review of Scientific Instruments*, **76**(6) (2005) 063113–063113–5.
- [94] Claudiu Andrei Stan. Experiments with interacting bose and fermi gases. <http://dspace.mit.edu/handle/1721.1/34384>, 2005. Thesis (Ph. D.)–Massachusetts Institute of Technology, Dept. of Physics, 2005.
- [95] Karl Jousten. *Handbook of vacuum technology*. Wiley-VCH, November 2008.
- [96] K.M. Birnbaum. Ultra-High vacuum chambers, September 2005.
- [97] Marc-Oliver Mewes, Wolfgang Ketterle. The Main-Chamber bakeout, Januar 1996.
- [98] Aviv Keshet. Cicero word generator git repository. <https://github.com/akeshet/Cicero-Word-Generator>.

- [99] Harold J. Metcalf, Peter Van der Straten. *Laser cooling and trapping*. Springer, 1999.
- [100] Vladilen Letokhov. *Laser Control of Atoms and Molecules*. Oxford University Press, USA, April 2007.
- [101] K. Dieckmann, R. J. C. Spreeuw, M. Weidemüller, J. T. M. Walraven. Two-dimensional magneto-optical trap as a source of slow atoms. *Physical Review A*, **58**(5) (1998) 3891–3895.
- [102] Thomas Gersdorf. Magneto-optical traps for a second generation optical lattice experiment, 2010. Bachelor Thesis.
- [103] Stephan Falke, Horst Knöckel, Jan Fribe, Matthias Riedmann, Eberhard Tiemann, Christian Lisdat. Potassium ground-state scattering parameters and Born-Oppenheimer potentials from molecular spectroscopy. *Physical Review A*, **78**(1) (2008) 012503.
- [104] Cheng-Hsun Wu, Ibon Santiago, Jee Woo Park, Peyman Ahmadi, Martin W. Zwierlein. Strongly interacting isotopic Bose-Fermi mixture immersed in a fermi sea. *Physical Review A*, **84**(1) (2011) 011601.
- [105] Dorothy Hoffman, Bawa Singh, John H. Thomas III. *Handbook of Vacuum Science and Technology*. Surendra Kumar, Oktober 1997.
- [106] John Prodan, William Phillips, Harold Metcalf. Laser production of a very slow monoenergetic atomic beam. *Physical Review Letters*, **49**(16) (1982) 1149–1153.
- [107] *Electromagnetic Radiation: Atomic, Molecular, and Optical Physics: Atomic, Molecular, And Optical Physics: Electromagnetic Radiation*. Academic Press, Juni 1997.
- [108] L. Ricci, M. Weidemüller, T. Esslinger, A. Hemmerich, C. Zimmermann, V. Vuletic, W. König, T. W Hänsch. A compact grating-stabilized diode laser system for atomic physics. *Optics Communications*, **117**(5-6) (1995) 541–549.
- [109] Sara Campbell. Building an apparatus for ultracold Lithium-Potassium Fermi-Fermi mixtures, 2010. Bachelor Thesis.
- [110] Wolfgang Ketterle, Kendall B. Davis, Michael A. Joffe, Alex Martin, David E. Pritchard. High densities of cold atoms in a dark spontaneous-force optical trap. *Physical Review Letters*, **70**(15) (1993) 2253–2256.
- [111] M. Prentiss, A. Cable, J. E. Bjorkholm, Steven Chu, E. L. Raab, D. E. Pritchard. Atomic-density-dependent losses in an optical trap. *Optics Letters*, **13**(6) (1988) 452–454.
- [112] Thad Walker, David Sesko, Carl Wieman. Collective behavior of optically trapped neutral atoms. *Physical Review Letters*, **64**(4) (1990) 408–411.
- [113] G. Modugno, C. Benkő, P. Hannaford, G. Roati, M. Inguscio. Sub-Doppler laser cooling of fermionic  ${}^40\text{K}$  atoms. *Physical Review A*, **60**(5) (1999) R3373–R3376.
- [114] Vladan Vuletić, Cheng Chin, Andrew J. Kerman, Steven Chu. Degenerate raman sideband cooling of trapped cesium atoms at very high atomic densities. *Physical Review Letters*, **81**(26) (1998) 5768–5771.
- [115] Kendall B. Davis, Marc-Oliver Mewes, Michael A. Joffe, Michael R. Andrews, Wolfgang Ketterle. Evaporative cooling of sodium atoms. *Physical Review Letters*, **74**(26) (1995) 5202–5205.

- [116] J.C. Maxwell. Ii. illustrations of the dynamical theory of gases. *Philosophical Magazine Series 4*, **20**(130) (1860) 21–37.
- [117] Wing William H. On neutral particle trapping in quasistatic electromagnetic fields. *Progress in Quantum Electronics*, **8**(3–4) (1984) 181–199.
- [118] Ettore Majorana. Atomi orientati in campo magnetico variabile. *Il Nuovo Cimento (1924-1942)*, **9** (1932) 43–50. 10.1007/BF02960953.
- [119] T. Bergeman, Gidon Erez, Harold Metcalf. Magnetostatic trapping fields for neutral atoms. *Physical Review A*, **35**(4) (1987) 1535–1546.
- [120] M.-O. Mewes, M. Andrews, N. van Druten, D. Kurn, D. Durfee, W. Ketterle. Bose-Einstein condensation in a tightly confining dc magnetic trap. *Physical Review Letters*, **77**(3) (1996) 416–419.
- [121] David Pritchard. Cooling neutral atoms in a magnetic trap for precision spectroscopy. *Physical Review Letters*, **51**(15) (1983) 1336–1339.
- [122] European Synchrotron Radiation Facility. Radia package. National Nuclear Data Center, Brookhaven National Laboratory.
- [123] P. Elleaume, O. Chubar, J. Chavanne. Computing 3d magnetic fields from insertion devices. In *Particle Accelerator Conference, 1997. Proceedings of the 1997*, Volume 3, p. 3509 –3511 vol.3, may 1997.
- [124] International Organization for Standardization. Fluid power systems and components – graphic symbols and circuit diagrams (din/iso 1219). <http://www.iso.org/>.
- [125] T. Van Zoest, N. Gaaloul, Y. Singh, H. Ahlers, W. Herr, S. T Seidel, W. Ertmer, E. Rasel, M. Eckart, E. Kajari, S. Arnold, G. Nandi, W. P Schleich, R. Walser, A. Vogel, K. Sengstock, K. Bongs, W. Lewoczko-Adamczyk, M. Schiemangk, T. Schuldt, A. Peters, T. Könenmann, H. Müntinga, C. Lämmerzahl, H. Dittus, T. Steinmetz, T. W Hänsch, J. Reichel. Bose-Einstein condensation in microgravity. *Science*, **328**(5985) (2010) 1540–1543.
- [126] Robert L. D. Campbell, Robert P. Smith, Naaman Tammuz, Scott Beattie, Stuart Moulder, Zoran Hadzibabic. Efficient production of large  $^{39}\text{K}$  bose-einstein condensates. *Phys. Rev. A*, **82** (2010) 063611.
- [127] Markus Greiner, Immanuel Bloch, Theodor W. Hänsch, Tilman Esslinger. Magnetic transport of trapped cold atoms over a large distance. *Physical Review A*, **63**(3) (2001) 031401.
- [128] M. J. Holland, B. DeMarco, D. S. Jin. Evaporative cooling of a two-component degenerate fermi gas. *Physical Review A*, **61**(5) (2000) 053610.
- [129] W. Geist, L. You, T. A. B. Kennedy. Sympathetic cooling of an atomic Bose-Fermi gas mixture. *Physical Review A*, **59**(2) (1999) 1500–1508.
- [130] Z. Hadzibabic, S. Gupta, C. A. Stan, C. H. Schunck, M. W. Zwierlein, K. Dieckmann, W. Ketterle. Fiftyfold improvement in the number of quantum degenerate fermionic atoms. *Physical Review Letters*, **91**(16) (2003) 160401.
- [131] Ariel Lipson, Stephen G. Lipson, Henry Lipson. *Optical Physics*. Cambridge University Press, Oktober 2010.

- [132] Waseem Bakr. *Microscopic Studies of Quantum Phase Transitions in Optical Lattices*. PhD thesis, 2011.
- [133] Christof Weitenberg. *Single-Atom Resolved Imaging and Manipulation in an Atomic Mott Insulator*. Universitätsbibliothek der Ludwig-Maximilians-Universität, München, 2011.
- [134] William I. Kordonsky, Igor V. Prokhorov, Sergei R. Gorodkin, Gennadii R. Gorodkin, Leonid K. Gleb, Bronislav E. Kashevsky. Magnetorheological polishing devices and methods, September 1995. U.S. Classification: 451/35 International Classification: B24B 31112.
- [135] P. Hariharan. *Basics of Interferometry*. Academic Press, 2007.
- [136] M. Karski, L. Förster, J. M. Choi, W. Alt, A. Widera, D. Meschede. Nearest-neighbor detection of atoms in a 1D optical lattice by fluorescence imaging. *Physical Review Letters*, **102**(5) (2009) 053001.
- [137] Manuel Endres, Takeshi Fukuhara, David Pekker, Marc Cheneau, Peter Schauß, Christian Gross, Eugene Demler, Stefan Kuhr, Immanuel Bloch. The Higgs amplitude mode at the two-dimensional superfluid/Mott insulator transition. *Nature*, **487**(7408) (2012) 454–458.
- [138] Jonathan Simon, Waseem S. Bakr, Ruichao Ma, M. Eric Tai, Philipp M. Preiss, Markus Greiner. Quantum simulation of antiferromagnetic spin chains in an optical lattice. *Nature*, **472**(7343) (2011) 307–312.
- [139] Amodsen Chotia, Brian Neyenhuis, Steven A. Moses, Bo Yan, Jacob P. Covey, Michael Foss-Feig, Ana Maria Rey, Deborah S. Jin, Jun Ye. Long-lived dipolar molecules and feshbach molecules in a 3D optical lattice. *Physical Review Letters*, **108**(8) (2012) 080405.



---

## Acknowledgements

---

At this point I want to look back and thank everyone who supported me and this project at MIT and all the great people that I met during the wonderful time there.

First, I want to thank Martin Zwierlein. His enthusiasm and spirit are unbelievable and absolutely unique (insiders call it the 'Chyeaaah' spirit, often misspelled as 'Tschyeaaah'). The unlimited trust and confidence in his students, his openness to new ideas and different approaches from everyone and his never-ending support enables his group to tackle projects that nobody believed to be possible. He allowed me to take over a lot of responsibility and I had his absolute confidence in what I did. This freedom together with the motivation of a visionary project coined myself more than any other part of my education. His support is inimitable and I felt really lucky to be part of his group. Martin also has an unmatched understanding of physics and we had great discussions not only on physics. At the end, we finally managed to organize a 'The Big Lebowski' night.

While working on the quantum gas microscope in the new lab, many people joined the Fermi2 team and made it an awesome place to work. I will never forget Vinay Ramasesh soldering all kinds of electronics while watching The Big Bang Theory and snacking Thorlabs snack boxes. Vinay shared our vision of a quantum gas microscope and spent all his spare time besides classes (and often much more than that) working for the lab. Together with Waseem Bakr, we built most of the experiment with amazing speed. Without Vinay and Waseem, it would not have been possible to engineer and build such a project.

Waseem joined our experiment shortly after the start and it was just awesome to work with him. He was really up to everything, whether if I asked him to explain a paper to us or to give me a hand while assembling something on the experiment (most notably winding a Zeeman slower). I could always count on him, no matter when. Even though he had another obligation with the BEC1 experiment, he really believed in our goal and pushed the experiment forward with full effort. His impressive expertise and his ability to ask the right questions made us do the right things and take the right decisions at the right time.

Furthermore, I want to mention the students who helped us building the experiment, namely Sara Campbell, Jordan Goldstein, David Reens, Takuma Inoue and Melih Okan. Their help and support was very helpful and especially David deserves a big thanks for his 'Yeah, let's do it' mentality.

The Fermi1 team, consisting of Peyman Ahmadi, Jee Woo Park, Ibon Santiago, Cheng-Hsun Wu and later with Sebastian Will made me always feel welcome, no matter if we had a tea together, if we let alkali elements react with water, if we were stealing optics from each other or if I wanted to know anything. Ibon and Peyman taught me a lot about ultracold atom experiments, helped me to start in the new lab and contributed significantly to the quantum gas microscope. Ibon's

helpfulness and Peyman's optimism and their positive attitude are unforgettable. Peyman's fearless approach to every problem and especially his ability to help people to achieve their goals is awesome.

The BEC1 team with Lawrence Cheuk, Mark Ku and Ariel Sommer and later Tarik Yefsah shared their office with me for a long time and especially allowed me to have our whole lab infrastructure and the complete experiment delivered to their office in thousands of small packages. I remember a lot of enjoyable moments, lunches, dinners and always a nice atmosphere.

The BEC5 lab with Ivana Dimitrova, Jesse Amato-Grill, Niklas Jepsen and Michael Messer together with almost-BEC5 resident Timur Rvachov made the CUA at MIT an awesome place to live. We did so many interesting and funny things together such that it really felt like a big family. Every single moment with them, from the unbelievable beach party in March shortly after the blizzard to the very precisely worked aluminum front-panel with laser-engraved signatures was great, I cannot express how much fun we had together. Another thing that I will always remember is Niki's happiness, which is for sure unbeatable. It is a great attitude and I think the whole group profited from it.

The people in the other labs in the CUA were always helpful and it was very nice to work in such an environment where everything (stuff, ideas) is just next door. Aviv Keshet and Christian Sanner shared a lot of engineering with us and provided a lot of inspiration for elegant and technically professional solutions. All labs in the CUA live the spirit of Wolfgang Ketterle and Dave Pritchard, who coined the CUA with their visionary leadership.

Everyone working to support the MIT community deserves to be mentioned. While setting up a new lab, it was great to have people like Al McGurl of the RLE, Andrew Gallant and his team of the central machine shop and Mark Belanger of Edgerton shop who helped me with many aspects of engineering. A big thanks goes to Joana Keseberg and the RLE headquarters staff, who were always very helpful.

On the other side of the Atlantic Ocean, I would like to thank Tilman Esslinger for his continuous support. He backed me with my ambitious plans for my Master's thesis and made everything possible at ETH that was needed to perform this project at MIT.

All the interesting people that I met during my studies at MIT and at ETH Zurich, especially my teachers, coworkers and fellow students, are wonderful and it was a great pleasure to study physics with them.

Most importantly I want to thank my parents, Irene and Joachim, and my sister Elisabeth for their continuous support in every respect during my whole life. With their continuous motivation and their never-ending interest in my plans they brought me to where I am now.

*I would like to dedicate this thesis to my family.*



Eidgenössische Technische Hochschule Zürich  
Swiss Federal Institute of Technology Zurich

## Declaration of Originality

**This sheet must be signed and enclosed with every piece of written work submitted at ETH.**

I hereby declare that the written work I have submitted entitled

---

is original work which I alone have authored and which is written in my own words.\*

### Author(s)

Last name

First name

---

### Supervising lecturer

Last name

First name

---

With the signature I declare that I have been informed regarding normal academic citation rules and that I have read and understood the information on 'Citation etiquette' ([http://www.ethz.ch/students/exams/plagiarism\\_s\\_en.pdf](http://www.ethz.ch/students/exams/plagiarism_s_en.pdf)). The citation conventions usual to the discipline in question here have been respected.

The above written work may be tested electronically for plagiarism.

---

Place and date

---

Signature

\*Co-authored work: The signatures of all authors are required. Each signature attests to the originality of the entire piece of written work in its final form.